



저작자표시-비영리-변경금지 2.0 대한민국

이용자는 아래의 조건을 따르는 경우에 한하여 자유롭게

- 이 저작물을 복제, 배포, 전송, 전시, 공연 및 방송할 수 있습니다.

다음과 같은 조건을 따라야 합니다:



저작자표시. 귀하는 원저작자를 표시하여야 합니다.



비영리. 귀하는 이 저작물을 영리 목적으로 이용할 수 없습니다.



변경금지. 귀하는 이 저작물을 개작, 변형 또는 가공할 수 없습니다.

- 귀하는, 이 저작물의 재이용이나 배포의 경우, 이 저작물에 적용된 이용허락조건을 명확하게 나타내어야 합니다.
- 저작권자로부터 별도의 허가를 받으면 이러한 조건들은 적용되지 않습니다.

저작권법에 따른 이용자의 권리는 위의 내용에 의하여 영향을 받지 않습니다.

이것은 [이용허락규약\(Legal Code\)](#)을 이해하기 쉽게 요약한 것입니다.

[Disclaimer](#)

공학박사 학위논문

**Relation Between Fabrication
Method and Photovoltaic
Performance of Planar
Heterojunction Perovskite Solar
Cells**

평면 이중접합 페로브스카이트 태양전지의 제작
방법과 광전 효율의 상관관계

2016년 2월

서울대학교 대학원

재료공학부

배 승 환

Abstract

**Relation Between Fabrication
Method and Photovoltaic
Performance of Planar
Heterojunction Perovskite Solar
Cells**

Seunghwan Bae

Department of Materials Science and Engineering

The Graduate School

Seoul National University

Although one-step deposition method has intensively been studied because of simple and easy fabrication of perovskite films, uncontrolled crystallization of perovskite during one-step deposition often results in films with small crystallites and low surface coverage, leading to low photovoltaic performance. In this study, we have proposed the optimum processing condition to afford favorable film morphology and crystal orientation for achieving high power conversion efficiency of perovskite solar cells. First, two different morphologies, tree-like and flower-like morphologies, are developed depending upon the spin-coating time and post-heat treatment temperature. When the perovskite is crystallized from the liquid film after short spin-coating time, the flower-like morphology is developed, whereas the tree-like morphology is developed when the perovskite is crystallized for long spin-coating time. When the morphology evolution is monitored using in-situ

optical microscopy and X-ray diffraction to investigate the origin of the difference between tree-like and flower-like morphologies, it reveals that $\text{CH}_3\text{NH}_3\text{I}-\text{PbI}_2$ -solvent complex is formed to develop the tree-like morphology before $\text{CH}_3\text{NH}_3\text{PbI}_3$ crystals are formed whereas the flower-like morphology is developed when the $\text{CH}_3\text{NH}_3\text{PbI}_3$ crystals are formed directly from the liquid film without formation of $\text{CH}_3\text{NH}_3\text{I}-\text{PbI}_2$ -solvent complex. The film with flower-like morphology, as prepared from DMSO solution, has large-sized crystallites, and the crystallites are highly orientated along (112) and (200) directions, resulting in a high PCE of 13.85%, whereas the film with tree-like morphology has small-sized crystallites with random crystal orientation, exhibiting very low PCEs. Second, we successfully fabricated $\text{CH}_3\text{NH}_3\text{PbI}_3$ crystals with two different orientations to the substrate using two different organic precursors ($\text{CH}_3\text{NH}_3\text{I}$ and $\text{CH}_3\text{NH}_3\text{Cl}$), and then investigated the effect of crystal orientation on the photovoltaic performance of $\text{CH}_3\text{NH}_3\text{PbI}_3$ solar cells with planar heterojunction structure. The power conversion efficiency (PCE) of inverted cell (13.60%) prepared with I_3 film (made from precursor $\text{CH}_3\text{NH}_3\text{I}$) is higher than that of the inverted cell (11.26%) prepared with I_2Cl film (made from precursor $\text{CH}_3\text{NH}_3\text{Cl}$) mainly due to higher short circuit current (J_{SC}) and higher fill factor (FF) of I_3 -based cell, whereas the PCE of normal cell (12.88%) prepared with I_2Cl film is higher than that of the inverted cell (3.97%) made of I_3 film. Considering that I_3 and I_2Cl films exhibit different crystal orientations, we realize that the crystal orientation of perovskite is directly related to PCE. The PCE difference due to different crystal orientation is interpreted by the charge carrier lifetime extracted from transient photoluminescence spectrum: Shorter lifetime affords faster charge transfer from perovskite layer to charge transport layer, thus the device with shorter lifetime exhibits higher J_{SC} and PCE. Strong hysteresis of $J-V$ curves of normal cells is also interpreted by slow and imbalanced charge transfer from perovskite to CTL.

Keywords: perovskite solar cells, methylammonium lead iodide, film morphology, planar heterojunction, processing method, crystal orientation

Student Number: 2009-23044

Contents

Chapter 1 Introduction	1
1.1 Organic-inorganic hybrid perovskite solar cells	1
1.1.1 Organic-inorganic hybrid perovskites.....	1
1.1.2 Physical properties of organic-inorganic hybrid perovskites	5
1.1.2.1 Optical properties.....	5
1.1.2.2 Bandgap and energy level	7
1.1.2.3 Exciton binding energy	9
1.1.2.4 Dielectric constant.....	10
1.1.2.5 Charge carrier diffusion lengths	11
1.1.2.6 Charge carrier mobilities.....	14
1.1.3 Device structures.....	16
1.2 Planar heterojunction perovskite solar cells.....	19
1.2.1 Operating principles.....	19
1.2.2 Fabrication methods for organic-inorganic hybrid perovskite	
film.....	22
1.3 Objectives of this study.....	29
Chapter 2 Experimental Section	33
2.1 Synthesis	33
2.1.1 Materials	33
2.1.2 Synthesis	33
2.1.2.1 Synthesis of organic precursors	33
2.1.2.2 Synthesis of titanium dioxide nanoparticles	34
2.2 Film fabrication and characterization	35
2.2.1 Materials	35
2.2.2 Fabrication method	35
2.2.3 Characterization method	36
2.3 Device fabrication and measurement.....	37
2.3.1 Materials	37
2.3.2 Solar cell device fabrication.....	38

2.3.2.1	Fabrication of devices with normal structure	38
2.3.2.2	Fabrication of devices with inverted structure	39
2.3.3	Solar cell performance measurement and device characterization	40

Chapter 3 Results and Discussion.....42

3.1	Two different mechanisms of $\text{CH}_3\text{NH}_3\text{PbI}_3$ film formation and its effect on photovoltaic properties	42
3.1.1	Synthesis and characterization	42
3.1.2	Photovoltaic properties	42
3.1.3	Mechanisms of $\text{CH}_3\text{NH}_3\text{PbI}_3$ film formation	47
3.1.4	$\text{CH}_3\text{NH}_3\text{PbI}_3$ crystal orientation	67
3.1.5	Summary	73
3.2	$\text{CH}_3\text{NH}_3\text{PbI}_3$ crystal orientation and photovoltaic performance of planar heterojunction perovskite solar cells	75
3.2.1	Synthesis and characterization	75
3.2.2	$\text{CH}_3\text{NH}_3\text{PbI}_3$ crystal orientation	75
3.2.3	Film morphology	81
3.2.4	Photovoltaic properties	83
3.2.5	Charge transfer characteristics	83
3.2.6	Photocurrent density–voltage hysteresis	90
3.2.7	Summary	93

Chapter 4 Conclusions95

Bibliography98

Korean Abstract 112

List of Tables

Table 3.1	Photovoltaic properties of $\text{CH}_3\text{NH}_3\text{PbI}_3$ perovskite solar cells depending on solvent and spin-coating time.....	45
Table 3.2	Photovoltaic properties of $\text{CH}_3\text{NH}_3\text{PbI}_3$ solar cells made of different organic precursor and different device structure....	85
Table 3.3	Fitting parameters of PL decays of $\text{CH}_3\text{NH}_3\text{PbI}_3$ and $\text{CH}_3\text{NH}_3\text{PbI}_3/\text{CTL}$	89
Table 3.4	Photovoltaic properties of $\text{CH}_3\text{NH}_3\text{PbI}_3$ solar cells depending on device structure, organic precursor and scan direction....	92

List of Figures

- Figure 1.1 (a) Ball and stick representation of the basic perovskite structure and (b) their extended network structure connected by the corner-shared octahedra. 2
- Figure 1.2 Schematic representation of two dimensional organic-inorganic hybrid perovskites (a) with bilayer and (b) single layer intercalated organic molecules. (ref. 16)..... 4
- Figure 1.3 (a) UV-Vis spectrum of $\text{CH}_3\text{NH}_3\text{PbI}_3$ film. (ref. 34) (b) Refractive index and extinction coefficient of $\text{CH}_3\text{NH}_3\text{PbI}_3$ film. (ref. 28)..... 6
- Figure 1.4 Energy levels vs. vacuum and NHE for various perovskite absorbers, TiO_2 and a conventional hole transporting material, 2,2',7,7'-tetrakis-(*N,N*-dimethoxyphenyl-amine)-9,9'-spirobifluorene (spiro-MeOTAD). For the MAPbCl_3 , there is no reference regarding the band structures. MA = CH_3NH_3^+ , EA = $\text{CH}_3\text{CH}_2\text{NH}_3^+$, FA = $\text{NH}_2\text{-CH=NH}_2^+$. (ref. 48) 8
- Figure 1.5 Top view (a) and cross-section view (b) of the scan electron microscope images of the $\text{CH}_3\text{NH}_3\text{PbI}_3$ film. (c) Frequency-dependent relative dielectric constant of the $\text{CH}_3\text{NH}_3\text{PbI}_3$ film. The $\text{CH}_3\text{NH}_3\text{PbI}_3$ film based device structure for dielectric constant measurement is shown in the inset. (ref. 43) 12
- Figure 1.6 Real permittivity (ϵ') as a function of frequency for different incident light intensity from dark to 1 sun. Inset, linear fitting of dielectric constant to illumination intensity at $f = 50$ mHz. (ref. 3) 12
- Figure 1.7 Carrier mobility characterization of $\text{CH}_3\text{NH}_3\text{PbI}_3$ single crystal. Current-voltage curve (A) for a hole-only $\text{CH}_3\text{NH}_3\text{PbI}_3$ single crystal device and (B) an electron-only $\text{CH}_3\text{NH}_3\text{PbI}_3$ single crystal device. The insets show the device structure of hole-only and electron-only $\text{CH}_3\text{NH}_3\text{PbI}_3$ single crystal devices, respectively. (C) Schematic illustration of the device for the time-of-flight measurement. (D) The transient current curves of the $\text{CH}_3\text{NH}_3\text{PbI}_3$ single crystal

	device show the normalized transient photocurrent under various reverse biases. (ref. 37)	15
Figure 1.8	Device structures of perovskite solar cells. (a) mesoscopic heterojunction, (b) planar heterojunction with normal structure and (c) planar heterojunction with inverted structure.....	17
Figure 1.9	Schematic representation of the charge transfer and charge transport in a perovskite-sensitized TiO ₂ solar cell and a noninjecting Al ₂ O ₃ - based solar cell. (ref. 68)	18
Figure 1.10	current density–voltage curve of solar cells and photovoltaic parameters represented in current density–voltage curve.....	20
Figure 1.11	Schematic representation of one-step deposition method.	22
Figure 1.12	SEM images of (a, c, e) vapor-deposited perovskite film and (b, d, f) solution-processed perovskite film. (ref. 71)	23
Figure 1.13	Schematic representation of solvent engineering procedure and SEM image of perovskite film fabricated by solvent engineering process. (ref. 98)	24
Figure 1.14	Schematic illustration of fast deposition-crystallization (FDC) process and conventional spin-coating process, and SEM images of perovskite films fabricated by FDC process and conventional spin-coating process. (ref. 99)	26
Figure 1.15	SEM images of the thermally annealed perovskite films with thicknesses of (a) 250 nm, (d) 430 nm and (g) 1015 nm, and solvent-annealed perovskite films with thickness of (b) 250 nm, (e) 430 nm and (h) 1015 nm; the scale bars in the SEM micrographs are 2 μm. (ref. 100)	28
Figure 3.1	¹ H NMR spectrum of methylammonium iodide.....	43
Figure 3.2	<i>J</i> – <i>V</i> curves of CH ₃ NH ₃ PbI ₃ perovskite solar cells. The CH ₃ NH ₃ PbI ₃ films in the devices are prepared by spin-coating the DMF and DMSO solutions with different spin-coating times, then are thermally treated at 110 °C for 30 s.	44
Figure 3.3	External quantum efficiency spectra of the best cells fabricated from DMF and DMSO solution. The CH ₃ NH ₃ PbI ₃ films are prepared by spin-coating at 3000 rpm for 3 s (DMF)	

	and 15 s (DMSO), respectively and are thermally treated at 110 °C for 30 s.....	46
Figure 3.4	Statistical analysis of the power conversion efficiencies of the CH ₃ NH ₃ PbI ₃ perovskite solar cells depending on solvent and spin-coating time.	47
Figure 3.5	<i>J–V</i> hysteresis of perovskite solar cells fabricated from DMF and DMSO solution. The CH ₃ NH ₃ PbI ₃ films are prepared by spin-coating at 3000 rpm for 3 s (DMF) and 15 s (DMSO), respectively and are thermally treated at 110 °C for 30 s.	48
Figure 3.6	The change of film state with different spin-coating time using DMF and DMSO solutions before heat treatment. Dashed lines denote the point at which the liquid film starts to solidify.	49
Figure 3.7	OM images of CH ₃ NH ₃ PbI ₃ films formed from DMF solution with various spin-coating time. All films are spin-coated at 3000 rpm and are thermally treated at 110 °C for 30 s immediately after spin-coating.	51
Figure 3.8	OM images of CH ₃ NH ₃ PbI ₃ films formed from DMSO solution with various spin-coating time. All films are spin-coated at 3000 rpm and are thermally treated at 110 °C for 30 s immediately after spin-coating.....	52
Figure 3.9	SEM images of CH ₃ NH ₃ PbI ₃ films with (a, b) flower-like and (c, d) tree-like morphology fabricated from (a, c) DMF and (b, d) DMSO solution. All films are thermally treated at 110 °C for 30 s immediately after spin-coating.	53
Figure 3.10	HRTEM images of CH ₃ NH ₃ PbI ₃ films with flower-like morphology. The films are spin-coated at 3000 rpm and are thermally treated at 110 °C for 30 s immediately after spin-coating.....	54
Figure 3.11	Nyquist plots of CH ₃ NH ₃ PbI ₃ solar cells with (a–d) different morphology and processing solvent under different applied voltage. (e) Bulk recombination times are calculated by fitting the Nyquist plot using (f) the equivalent circuit.....	57
Figure 3.12	In-situ OM images of crystal growth in liquid films under	

	room temperature. The liquid films prepared from DMF and DMSO solutions are spin-coated for 3 s and 30 s, respectively.	58
Figure 3.13	In-situ OM images of crystal growth in liquid films at 110 °C. The liquid films prepared from DMF and DMSO solutions are spin-coated for 3 s and 30 s, respectively.....	59
Figure 3.14	XRD patterns of films fabricated from DMF and DMSO solution. Liquid films are solidified by standing the films at room temperature for >20 s (DMF) or >60 s (DMSO). The solidified films are thermally treated at 110 °C until the peaks of CH ₃ NH ₃ I–PbI ₂ –solvent complex disappear.....	61
Figure 3.15	FT-IR spectra of (a) DMF (solution), PbI ₂ –DMF (powder), CH ₃ NH ₃ I–PbI ₂ –DMF (powder) and (b) DMSO (solution), PbI ₂ –DMSO (powder), CH ₃ NH ₃ I–PbI ₂ –DMSO (powder). ..	62
Figure 3.16	XRD patterns of films fabricated from DMF and DMSO solution. The solidified films are prepared by spin-coating at 3000 rpm for 30 s (DMF) or 90 s (DMSO). When the solid films after spin-coating are thermally treated at 110 °C for 30 s, all peaks corresponding to CH ₃ NH ₃ I–PbI ₂ –solvent complex crystal completely disappear.....	64
Figure 3.17	OM images of solidified film during the spin-coating and the film after heat treatment. The solidified films are fabricated from DMF solution and prepared by spin-coating at 3000 rpm for 30 s. The solidified film after spin-coating are thermally treated at 110 °C for 30 s.	65
Figure 3.18	OM images of CH ₃ NH ₃ PbI ₃ films prepared from DMF and DMSO solution. The films are prepared by heating the liquid films, which are prepared by spin-coating at 3000 rpm for 3 s (DMF) or for 30 s (DMSO), at 60, 80 and 100 °C.....	66
Figure 3.19	Powder XRD patterns of CH ₃ NH ₃ PbI ₃ films with flower-like and tree-like morphology fabricated from DMF and DMSO solution. All films are thermally treated at 110 °C for 30 s after spin-coating. Films with flower-like and tree-like morphologies are ground for powder samples.....	67

Figure 3.20	XRD patterns of $\text{CH}_3\text{NH}_3\text{PbI}_3$ films with flower-like and tree-like morphology as prepared from DMF and DMSO solution. All films are thermally treated at 110 °C for 30 s immediately after spin-coating. 68
Figure 3.21	2D GIXD patterns of $\text{CH}_3\text{NH}_3\text{PbI}_3$ films with (a, b) tree-like and (c, d) flower-like morphologies fabricated from (a, c) DMF and (b, d) DMSO solution. All films are thermally treated at 110 °C for 30 s after spin-coating. 70
Figure 3.22	Assignment of peaks showing preferred orientation of $\text{CH}_3\text{NH}_3\text{PbI}_3$ crystallites in films. The films with flower-like morphology are prepared from DMSO solution. 71
Figure 3.23	Unit cell of tetragonal $\text{CH}_3\text{NH}_3\text{PbI}_3$ crystal. The C, N, I and Pb atoms are represented as brown, light blue, purple and black spheres, respectively, and black octahedra represent PbI_6 units. Solid lines indicate (a) (002), (b) (110), (c) (112) and (d) (200) planes. 72
Figure 3.24	^1H NMR spectrum of methylammonium chloride. 76
Figure 3.25	XRD patterns of films fabricated from (a) two different organic precursors ($\text{CH}_3\text{NH}_3\text{I}$ and $\text{CH}_3\text{NH}_3\text{Cl}$) and (b) the change of XRD patterns of I_2Cl films according to $\text{CH}_3\text{NH}_3\text{I}$ treatment. $\text{CH}_3\text{NH}_3\text{I}$ is treated on I_2Cl film several times to minimize the residual amount of $\text{CH}_3\text{NH}_3\text{PbCl}_3$ in $\text{CH}_3\text{NH}_3\text{PbI}_3$ crystal. 78
Figure 3.26	GIXD patterns of (a) I_3 and (b) I_2Cl film and (c, d) azimuthal angle (χ) scans. 79
Figure 3.27	Assignment of diffraction peaks. 2D diffraction pattern of I_3 film is assigned by calculated pattern of $\text{CH}_3\text{NH}_3\text{PbI}_3$ crystals oriented such (a) (112) and (b) (200) planes that are parallel to the substrate. 2D diffraction pattern of I_2Cl film is assigned by calculated pattern of $\text{CH}_3\text{NH}_3\text{PbI}_3$ crystals oriented such (a) (002) and (b) (112) planes that are parallel to the substrate. 80
Figure 3.28	Ball-and-stick representation of $\text{CH}_3\text{NH}_3\text{PbI}_3$ crystal in which (002), (110), (112) and (200) planes are parallel to the

	substrate. The C, N, I and Pb atoms are represented by brown, blue, purple and black spheres, respectively, and dark grey octahedron represent PbI_6 unit..	81
Figure 3.29	SEM images of films fabricated from different organic precursors: (a) I_3 film, (b) I_2Cl , and I_2Cl films after $\text{CH}_3\text{NH}_3\text{I}$ is treated (c) one and (d) two times.....	82
Figure 3.30	J - V curves of (a) inverted cells and (b) normal cells.....	84
Figure 3.31	EQE spectra of (a) inverted cells and (b) normal cells.	86
Figure 3.32	(a) energy levels of materials used for solar cells; transient photoluminescence spectra: (b) pristine $\text{CH}_3\text{NH}_3\text{PbI}_3$ film, (c) $\text{CH}_3\text{NH}_3\text{PbI}_3/\text{PEDOT:PSS}$, (d) $\text{CH}_3\text{NH}_3\text{PbI}_3/\text{PCBM}$, (e) $\text{CH}_3\text{NH}_3\text{PbI}_3/\text{spiro-OMeTAD}$ and (f) $\text{CH}_3\text{NH}_3\text{PbI}_3/\text{TiO}_2$. All samples for PL are prepared on quartz glass.....	88
Figure 3.33	J - V hysteresis of (a, b) inverted and (c, d) normal cells. The devices are fabricated from (a, c) I_3 and (b, d) I_2Cl films.	91

Chapter 1. Introduction

1.1 Organic-inorganic hybrid perovskite solar cells

1.1.1 Organic-inorganic hybrid perovskites

Perovskite is the name of crystal structure that is found in inorganic mineral CaTiO_3 at first. CaTiO_3 is discovered by German mineralogist, Gustav Rose, in 1839 and is named after a Russian mineralogist, Lew A. Perovski. A Unit cell of CaTiO_3 has cubic ABX_3 structure (Figure 1.1). A cations (Ca^{2+} for CaTiO_3) are located at corners, B cations (Ti^{4+} for CaTiO_3) are located at body center of cubic and X anions (O^{2-} for CaTiO_3) are placed at face centers of cubic.

Materials that have ABX_3 structure are also known as the perovskite. Each of A, B and X generally represents large rare earth metal cation, small metal cation and anion. A cation is surrounded by twelve X anions due to large size, however, the B cation is positioned in the octahedron that is formed by six X anions due to small size. There are many different perovskites such as CaTiO_3 , PbTiO_3 , BaTiO_3 , MgSiO_3 , SrFeO_3 , LiNbO_3 , SrZrO_3 , BaZrS_3 , KMgF_3 . After the first report of Weber that A cation can be replaced by small organic cation, methylammonium (CH_3NH_3^+) to generate the three-dimensional organic-inorganic hybrid perovskites,^{1,2} it is discovered that ethylammonium ($\text{CH}_3\text{CH}_2\text{NH}_3^+$), formamidinium ($\text{HC}(\text{NH}_2)_2^+$) can also form the organic-inorganic hybrid perovskite.

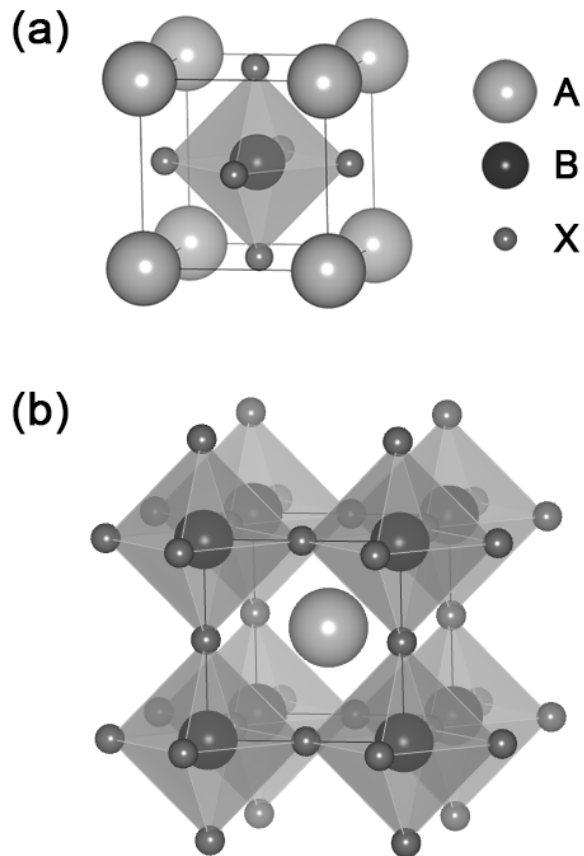


Figure 1.1. (a) Ball and stick representation of the basic perovskite structure and (b) their extended network structure connected by the corner-shared octahedra.

Perovskites generally have various phases with many different physical properties such as dielectric,^{3,4} ferroelectric,⁵⁻⁸ magnetoresistive,⁶ thermoelectric,⁹ electro-optic,¹⁰ semiconducting,¹¹ conducting^{6,12} and superconducting.^{7,13} These physical properties can be affected by distortion of cubic unit cell of the perovskite that is pseudo-cubic or distorted cubic in nature.¹⁴ Therefore, the size of organic cation and metal ions can be one of the important parameters to modulate the physical properties of perovskites. When too bulky organic cations are applied for perovskite, it cannot be embedded into the three dimensional perovskite, however, some of the bulky organic cations results two-dimensional layered organic-inorganic hybrid perovskite instead of three dimensional perovskite.

The concept of two-dimensional layered organic–inorganic perovskite was originated from the three-dimensional perovskite structure by cutting three-dimensional perovskite into one layer thick slice along (100) direction. Using relatively bulky organic cation, three dimensional metal halide octahedral frameworks are divided into a sheet (called perovskite sheet) which is sandwiched by organic cations (Figure 1.2). When, in ABX_3 structure, alkyl or aromatic ammonium ($R-NH_3^+$) or diammonium ($NH_3^+-R-NH_3^+$) are used as A cations and divalent metal cations such as Pb^{2+} , Cu^{2+} , Ni^{2+} , Co^{2+} , Fe^{2+} , Mn^{2+} , Pd^{2+} , Cd^{2+} , Sn^{2+} are used as B cations where halides are used as X anions, ammonium ions of organic cations interact with inorganic layer and R groups of organic cations are positioned between inorganic sheets. The physical interaction between ammonium ions and inorganic sheets is very important in the two dimensional layered perovskite.^{15,16}

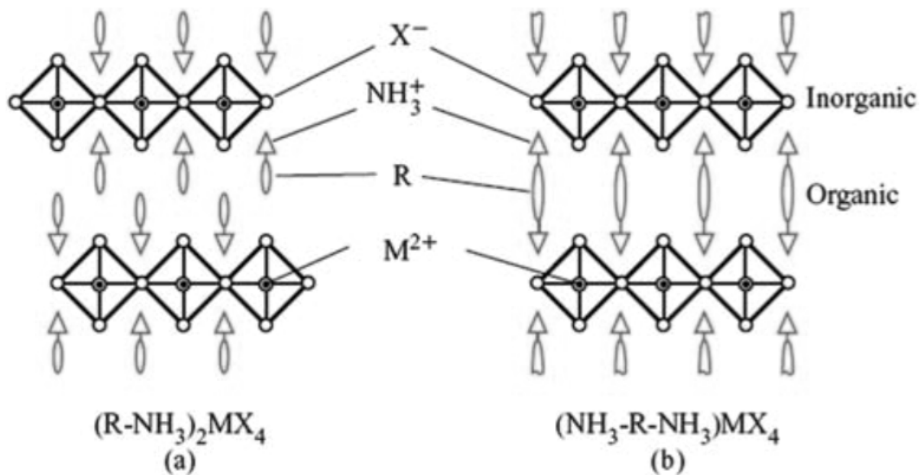


Figure 1.2. Schematic representation of two dimensional organic-inorganic hybrid perovskites (a) with bilayer and (b) single layer intercalated organic molecules. (ref. 16)

In organic-inorganic hybrid perovskites, ABX_3 where $\text{A} = \text{CH}_3\text{NH}_3^+$, $\text{B} = \text{Sn}^{2+}$, Pb^{2+} and $\text{X} = \text{Cl}^-$, Br^- , I^- have been reported.^{2,17-21} Mitzi *et. al.*^{12,22,23} applied them into field effect transistors²⁴ and electroluminescent devices^{25,26} due to high charge carrier mobilities. Recently, organic-inorganic hybrid perovskites have intensively been studied as a promising light absorber of solar cells because those have superior properties such as high absorption coefficient,^{27,28} low exciton binding energy,²⁹⁻³³ long charge carrier diffusion length³⁴⁻³⁷ and high charge carrier mobility.^{11,38-40} Furthermore, organic-inorganic hybrid perovskites are suitable for solution and low temperature

processing because the precursor materials have enough solubility in several organic solvents (dimethyl formamide, dimethyl sulfoxide, N-methylpyrrolidone, γ -butyrolactone).¹⁶⁻¹⁹ Particularly, the power conversion efficiency (PCE) of perovskite solar cells has increased dramatically from the first report of 3.8%²³ in 2009 to recent 20%.²⁴

1.1.2 Physical properties of organic-inorganic hybrid perovskites

Organic-inorganic hybrid perovskites have been introduced for light absorber for solar cells and received great interest due to capability for fabricating low cost and high efficiency solar cells. Organic-inorganic hybrid perovskites have superior properties such as high absorption coefficient,^{27,28} low exciton binding energy,²⁹⁻³³ large dielectric constant,⁴¹⁻⁴³ long charge carrier diffusion length³⁴⁻³⁷ and high charge carrier mobilities.^{11,38-40}

1.1.2.1 Optical properties

Park reported that the absorption coefficient of $\text{CH}_3\text{NH}_3\text{PbI}_3$ was estimated to be $1.5 \times 10^4 \text{ cm}^{-1}$ at 550 nm, $0.5 \times 10^4 \text{ cm}^{-1}$ at 700 nm.²⁷ These results indicate that 550 nm light is penetrated into a depth of only 0.66 μm , and 700 nm light is penetrated into a depth of only 2 μm . Therefore, 2 μm -thick perovskite film is enough to absorb the most of the light. Xing *et. al.*³⁴ also reported that absorption coefficient was estimated to be $5.7 \times 10^4 \text{ cm}^{-1}$ at 600 nm (Figure 1.3). Difference of absorption coefficient may originate from

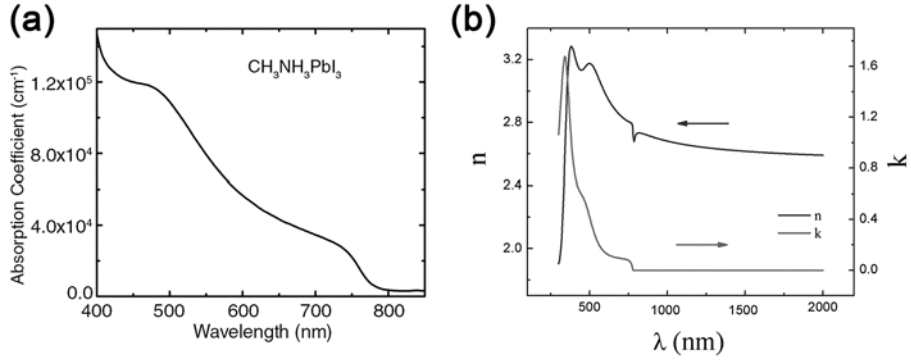


Figure 1.3. (a) UV-Vis spectrum of $\text{CH}_3\text{NH}_3\text{PbI}_3$ film. (ref. 34) (b) Refractive index and extinction coefficient of $\text{CH}_3\text{NH}_3\text{PbI}_3$ film. (ref. 28)

$\text{CH}_3\text{NH}_3\text{PbI}_3$ film morphology and crystallinity.

Ziang *et al.*²⁸ studied refractive index ($n(\lambda)$) and extinction coefficient ($k(\lambda)$) of $\text{CH}_3\text{NH}_3\text{PbI}_3$ film by spectroscopic ellipsometry. According to the Ziang *et al.*, the $k(\lambda)$ represents three major absorption peaks, 776 nm (1.60 eV), 492 nm (2.52 eV) and 350 nm (3.54 eV). Absorption peaks at 776 nm and 492 nm are attributed to direct gap transition of the $\text{CH}_3\text{NH}_3\text{PbI}_3$ from the first valence band maximum to the conduction band minimum and transition from lower valence band minimum to the conduction band minimum, respectively. However, absorption peak at 350 nm is not assigned and further study will be needed.

1.1.2.2 Bandgap and energy level

In previous studies, optical bandgap of $\text{CH}_3\text{NH}_3\text{PbI}_3$ is reported ranging from 1.5 eV to 1.6 eV⁴⁴ and energy levels of valance band maximum (VBM) and conduction band minimum (CBM) are 5.4 eV and 3.9 eV, respectively.^{28, 45–47} Interestingly, bandgap and energy levels of CBM and VBM of organic-inorganic hybrid perovskites can be tuned by changing the organic cation, metal cation and halide (Figure 1.4).⁴⁸ When CH_3NH_3^+ is replaced by $\text{NH}_2\text{-CH=NH}_2^+$, bandgap is reduced from 1.5 eV to 1.4 eV accompanying the shift of CBM from -3.9 eV to -4.0 eV.⁴⁹ However, CH_3NH_3^+ is replaced by $\text{CH}_3\text{CH}_2\text{NH}_3^+$, bandgap is increased to 2.2 eV.⁵⁰ Ogomi *et. al.* studied effect of Pb replacement by Sn in various ratio on electronic properties of $\text{CH}_3\text{NH}_3\text{PbI}_3$. For $\text{CH}_3\text{NH}_3\text{Sn}_{1-x}\text{Pb}_x\text{I}_3$, When x is decreased from 1 to 0, bandgap is decreased gradually from 1.55 to 1.17 eV accompanying the extension of light absorption to 1060 nm.⁴⁶ The alternation of halide that affect the bandgap is widely studied. In $\text{CH}_3\text{NH}_3\text{PbX}_3$, the band gaps are 3.11, 2.22 ad 1.51 eV for X= Cl, Br and I, respectively.^{51,52} Although the bandgap of $\text{CH}_3\text{NH}_3\text{PbX}_3$ cannot be tuned less than bandgap of $\text{CH}_3\text{NH}_3\text{PbI}_3$, however, partial replacement of halide can be a useful method to finely tune the bandgap. In the case of $\text{CH}_3\text{NH}_3\text{Pb}(\text{I}_{1-x}\text{Br}_x)_3$ ($0 \leq x \leq 1$), Noh *et. al.*⁵² revealed that bandgap is gradually tuned from 1.5 eV to 2.2 eV by adjusting the ratio of Br. They suggest the relation between halide composition x and bandgap by following equation.

$$E_g(x) = 1.57 + 0.39x + 0.33x^2 \quad (1.1)$$

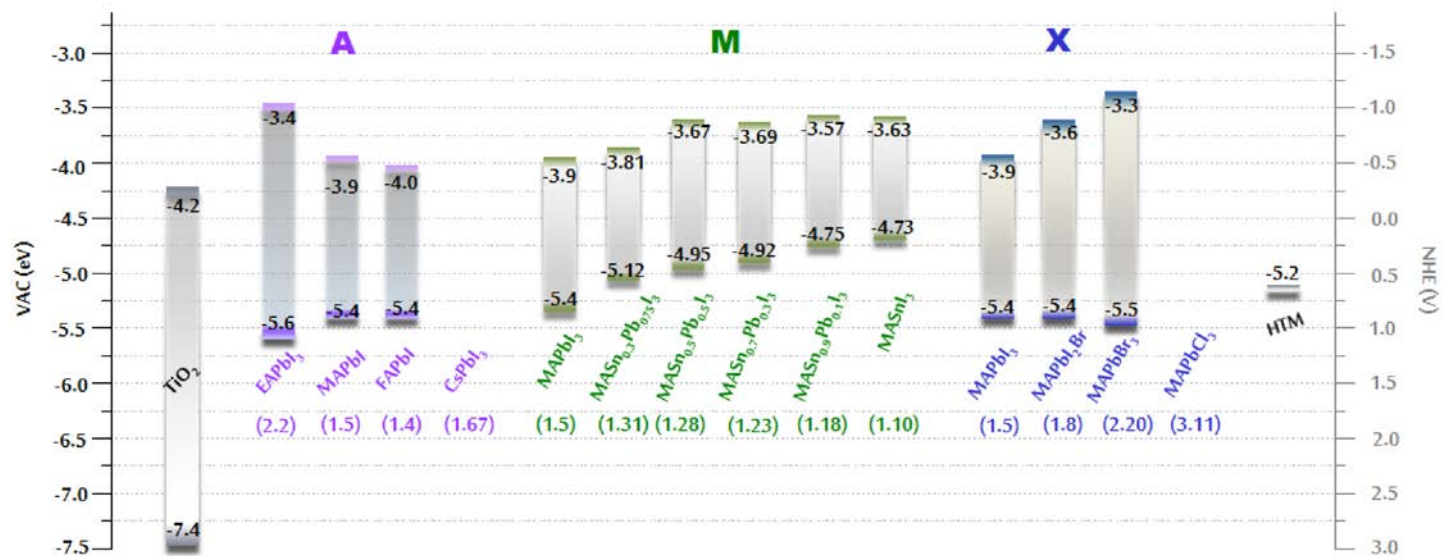


Figure 1.4. Energy levels vs. vacuum and NHE for various perovskite absorbers, TiO₂ and a conventional hole transporting material, 2,2',7,7'-tetrakis-(*N,N*-dimethoxyphenyl-amine)-9,9'-spirobifluorene (spiro-MeOTAD). For the MAPbCl₃, there is no reference regarding the band structures. MA = CH₃NH₃⁺, EA = CH₃CH₂NH₃⁺, FA = NH₂-CH=NH₂⁺. (ref. 48)

Change of crystal structure from the tetragonal structure of $\text{CH}_3\text{NH}_3\text{PbI}_3$ to binding energy to be 37 meV by measuring a magnetoabsorption.⁴¹ Ishihara and Zhang *et. al.* also reported 45 meV²⁹ and 100 meV³⁰, respectively, by temperature-dependent photoluminescence, and Koutselas *et. al.* and Tanaka *et. al.* reported 30 meV³³ and 50 meV,⁵⁶ respectively, by optical absorption. Miyata *et. al.* reported 16 meV by theoretical calculation³¹ and D’Innocenzo *et. al.* reported 55 meV by temperature-dependent optical absorption.⁵⁵ It should be noted that the exciton binding energy in organic photovoltaics is generally accepted to be ~300 meV and it is much larger than exciton binding energy of $\text{CH}_3\text{NH}_3\text{PbI}_3$. In the perovskite layer, exciton is easily dissociated, therefore, energy level offset between lowest unoccupied molecular orbital (LUMO) energy levels of electron donor materials and electron acceptor materials is not to be considered significantly in perovskite solar cells.

1.1.2.3 Exciton binding energy

When light with energy larger than bandgap is illuminated to the light absorber, electrons in valence band are excited to the conduction band and holes and electrons are produced. The photo-induced hole and electron are bound by Coulomb attraction and move like a particle. It is called “exciton”. Excitons are generally classified in two types, Wannier-Mott exciton and Frenkel exciton. Wannier-Mott excitons have low binding energies ranging from 20 meV to 98 meV,^{8,30,55-57} while Frenkel excitons have much higher binding energy (>100 meV) than Wannier-Mott excitons. Wannier-Mott

excitons can be dissociated into free charge carriers by the thermal energy of room temperature however Frenkel excitons require additional energy to be dissociated. It is clear that low exciton binding energy easily produces free charge carriers and is favorable for the high efficiency solar cells.

Exciton binding energy has been estimated in organic-inorganic hybrid perovskites. Hirasawa *et. al.* demonstrated that Wannier-Mott exciton with a large radius about 28 Å is formed in CH₃NH₃PbI₃, and reported the exciton binding energy to be 37 meV by measuring a magnetoabsorption.⁴¹ Ishihara and Zhang *et. al.* also reported 45 meV²⁹ and 100 meV³⁰, respectively, by temperature-dependent photoluminescence, and Koutselas *et. al.* and Tanaka *et. al.* reported 30 meV³³ and 50 meV,⁵⁶ respectively, by optical absorption. Miyata *et. al.* reported 16 meV by theoretical calculation³¹ and D'Innocenzo *et. al.* reported 55 meV by temperature-dependent optical absorption.⁵⁵ It should be noted that the exciton binding energy in organic photovoltaics is generally accepted to be ~300 meV and it is much larger than exciton binding energy of CH₃NH₃PbI₃. In the perovskite layer, exciton is easily dissociated, therefore, energy level offset between lowest unoccupied molecular orbital (LUMO) energy levels of electron donor materials and electron acceptor materials is not to be considered significantly in perovskite solar cells.

1.1.2.4 Dielectric constant

Dielectric constant affects exciton binding energy and charge carrier diffusion length. Large dielectric constant results low exciton binding energy

and long diffusion length. In organic-inorganic hybrid perovskites, large dielectric constant has been reported. In early studies, Hirawara *et. al.* reported that dielectric constant is about 6.5.⁴¹ Samiee *et. al.* also reported dielectric constant to be ~18 by measurement of saturation capacitance at low frequency.⁴² Recently, according to the report of Hu *et. al.*, giant dielectric constants over 500 and ~32 are observed at low frequency region and high frequency region, respectively, under dark conditions (Figure 1.5).⁴³ Juarez-Perez *et. al.* exhibited that dielectric constant is increased with illumination intensity up to an additional factor 1000 under 1 sun (Figure 1.6).³ Such large dielectric constants of organic-inorganic hybrid perovskites exhibit harsh contrast to the dielectric constant (~3) of organic materials which are used for organic photovoltaics.^{58,59} It indicates that organic-inorganic hybrid perovskite is nonexcitonic materials and Coulomb interaction between hole and electron which results charge recombination is effectively screened. Therefore, the large dielectric constant is one of the superior properties of the organic-inorganic hybrid perovskites for high efficiency solar cells.

1.1.2.5 Charge carrier diffusion lengths

Long charge carrier diffusion length is one of the superior properties of organic-inorganic hybrid perovskites. In organic photovoltaic, organic materials have exciton diffusion length of ~10 nm. Due to the short exciton diffusion length, bulk heterojunction is introduced to organic solar cells for enhanced light harvesting. However, optimizing the active layer morphology

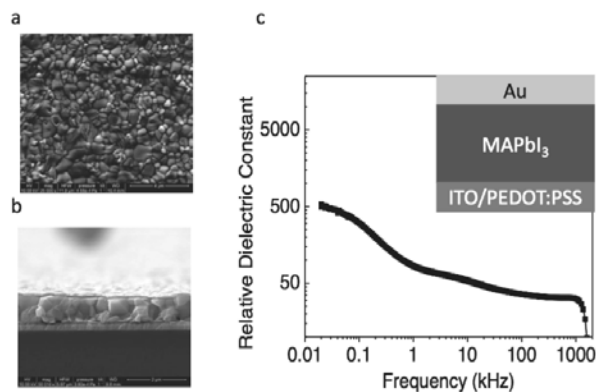


Figure 1.5. Top view (a) and cross-section view (b) of the scan electron microscope images of the $\text{CH}_3\text{NH}_3\text{PbI}_3$ film. (c) Frequency-dependent relative dielectric constant of the $\text{CH}_3\text{NH}_3\text{PbI}_3$ film. The $\text{CH}_3\text{NH}_3\text{PbI}_3$ film based device structure for dielectric constant measurement is shown in the inset. (ref. 43)

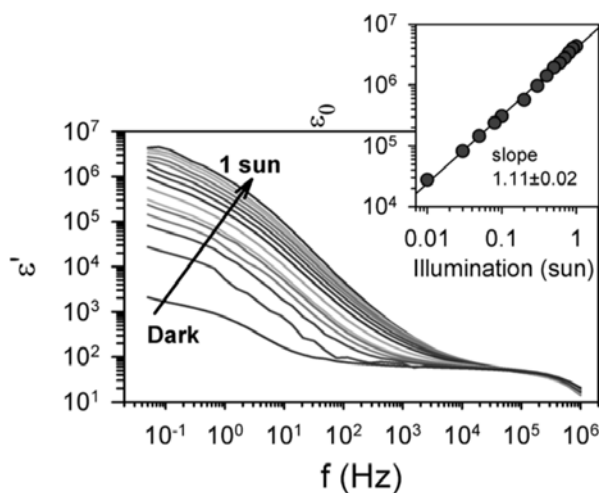


Figure 1.6. Real permittivity (ϵ') as a function of frequency for different incident light intensity from dark to 1 sun. Inset, linear fitting of dielectric constant to illumination intensity at $f = 50$ mHz. (ref. 3)

is difficult and the optimized morphology is not a thermodynamically stable state but a kinetically trapped state. In perovskite solar cells, device with planar heterojunction structure which is very simple and easy to fabricate is possible due to long charge carrier diffusion length of organic-inorganic hybrid perovskite.

Xing *et. al.*³⁴ reported long charge carrier diffusion length of $\text{CH}_3\text{NH}_3\text{PbI}_3$. By using the diffusion coefficients which are estimated from the transient absorption decay dynamics with drift-diffusion model, electron and hole diffusion lengths are estimated to be 130 nm and 110 nm, respectively. However, the reported charge carrier diffusion lengths by Xing *et. al.*³⁴ are hard to be considered as intrinsic properties because charge carrier diffusion length of perovskite is sensitive to perovskite film quality (e.g. crystallinity, domain size, defect density). Recently, Dong *et. al.*³⁷ reported electron-hole diffusion length of $\text{CH}_3\text{NH}_3\text{PbI}_3$ single crystal. Charge diffusion length is estimated over 175 micrometers under 1 sun and exceed 3 millimeters under weak light, respectively. If the charge diffusion length reported by Dong *et. al.*³⁷ is regarded as intrinsic properties, diffusion length of organic-inorganic hybrid perovskite is more than 5 orders of magnitude larger than organic materials for organic solar cells. Such long charge carrier diffusion lengths are one of the most promising properties of organic-inorganic hybrid perovskites for high efficiency solar cells.

1.1.2.6 Charge carrier mobilities

Charge carrier mobility is an important parameter for extraction of photo-induced charges. Low charge carrier mobility results slow charge extraction which causes a charge recombination and deteriorates a solar cell efficiency. In organic photovoltaics, space charge limited current (SCLC) mobilities of active layers are generally ranging from 10^{-5} to 10^{-3} $\text{cm}^2 \text{V}^{-1} \text{s}^{-1}$. Organic-inorganic hybrid perovskites exhibit much higher charge carrier mobilities than SCLC mobilities of active layers for organic photovoltaics.^{11,38-40} Constantinos *et. al.*¹¹ reported electron mobility to be $\sim 66 \text{ cm}^2 \text{V}^{-1} \text{s}^{-1}$ for $\text{CH}_3\text{NH}_3\text{PbI}_3$ by combining resistivity and Hall effect data and Wehrenfennig *et. al.*⁴⁰ reported mobilities of $10 \text{ cm}^2 \text{V}^{-1} \text{s}^{-1}$ for mesosuperstructured perovskite films using time-resolved terahertz spectroscopy. Further, Leijtens *et. al.* reported $\sim 20 \text{ cm}^2 \text{V}^{-1} \text{s}^{-1}$ by using time-resolved terahertz photoconductivity measurement and Dong *et. al.*³⁷ measured carrier mobilities of $\text{CH}_3\text{NH}_3\text{PbI}_3$ single crystal (Figure 1.7). According to the report of Dong *et. al.*,³⁷ hole mobilities are measured to be $165 \pm 25 \text{ cm}^2 \text{V}^{-1} \text{s}^{-1}$ and $105 \pm 35 \text{ cm}^2 \text{V}^{-1} \text{s}^{-1}$ by SCLC and Hall effect, respectively. And electron mobilities are estimated to be $24.8 \pm 4.1 \text{ cm}^2 \text{V}^{-1} \text{s}^{-1}$ and $24.0 \pm 6.8 \text{ cm}^2 \text{V}^{-1} \text{s}^{-1}$ by Hall effect and time-of-flight. Thus, these high mobilities represent that organic-inorganic hybrid perovskites can be a promising material in many applications.

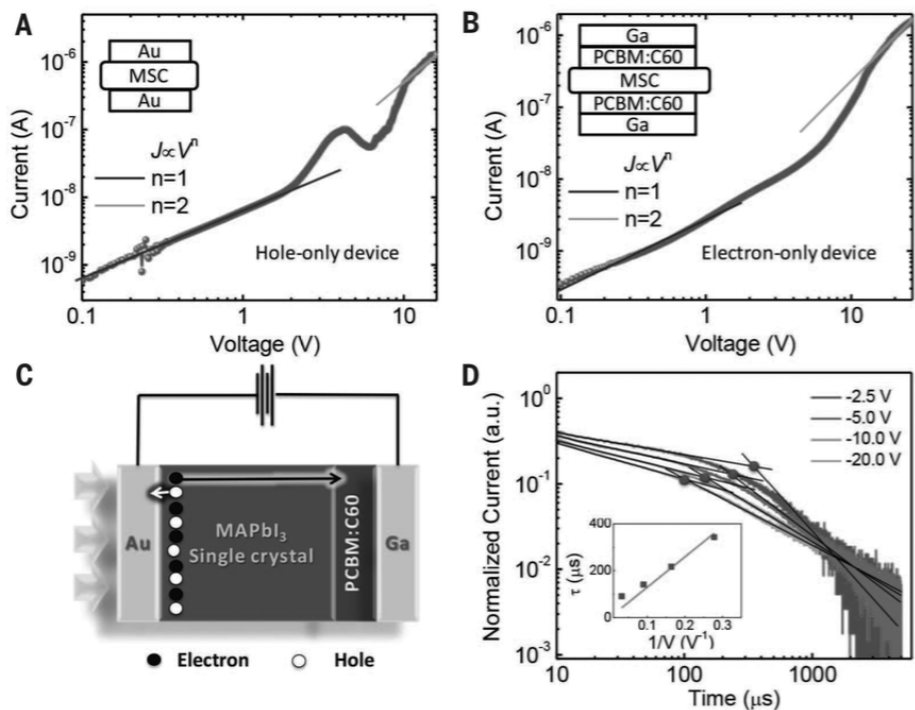


Figure 1.7. Carrier mobility characterization of $\text{CH}_3\text{NH}_3\text{PbI}_3$ single crystal. Current-voltage curve (A) for a hole-only $\text{CH}_3\text{NH}_3\text{PbI}_3$ single crystal device and (B) an electron-only $\text{CH}_3\text{NH}_3\text{PbI}_3$ single crystal device. The insets show the device structure of hole-only and electron-only $\text{CH}_3\text{NH}_3\text{PbI}_3$ single crystal devices, respectively. (C) Schematic illustration of the device for the time-of-flight measurement. (D) The transient current curves of the $\text{CH}_3\text{NH}_3\text{PbI}_3$ single crystal device show the normalized transient photocurrent under various reverse biases. (ref. 37)

1.1.3 Device structures

Device structure of perovskite solar cells are originated from the device structure of dye-sensitized solar cells (DSSCs). Kojima *et. al.*⁶⁰ used mesoscopic heterojunction device with mesoporous TiO₂ layer in first report of the perovskite solar cell (Figure 1.8a). 2,2',7,7'-tetrakis(N,N-di-p-methoxyphenylamino)-9,9'-spirobifluorene (spiro-OMeTAD) which is typically used as hole transport material also stems from solid state dye-sensitized solar cells (ss-DSSC). Unfortunately, mesoporous TiO₂ requires sintering process at >450 °C, materials for low temperature processing have been required.

For an alternative material of mesoporous TiO₂,⁶¹⁻⁶⁷ mesoporous Al₂O₃ is introduced.^{68,69} Annealing process of mesoporous Al₂O₃ is carried out at 150 °C which is quite low temperature compared to sintering temperature of TiO₂. Although the insulating property of Al₂O₃, device with mesoporous Al₂O₃ layer exhibits higher efficiency than device with mesoporous TiO₂. The improved efficiency originates from efficient electron collection through organic-inorganic hybrid perovskite than through the TiO₂ because perovskite facilitates the electron transport compared to the TiO₂ (Figure 1.9).

Due to the long charge carrier diffusion length of organic-inorganic hybrid perovskites as is mentioned at Section 1.1.2.5, device structure without mesoporous layer which is called as planar heterojunction structure are introduced for perovskite solar cells (Figure 1.8b). By using the planar heterojunction devices, high power conversion efficiencies have been

reported,⁷⁰⁻⁷⁸ because perovskites have ambipolar characteristics and show high charge carrier mobilities. Long charge carrier diffusion length is also enough to increase the thickness of perovskite film for efficient light harvesting.

Fabrication of planar heterojunction structure is simple and easy rather than mesoporous structure, it is also applied to OPV-type device (Figure 1.8c).⁷⁹⁻⁹⁰ In OPV-type planar heterojunction devices, holes are collected to the transparent electrode and electrons are collected to the metal electrode. In contrast, holes are collected to the metal electrode and electrons are collected to the transparent electrode in DSSC-type planar heterojunction devices. To distinguish these two types of planar heterojunction structures, DSSC-type device structure is named “normal structure” and OPV-type device structure is named “inverted structure”.

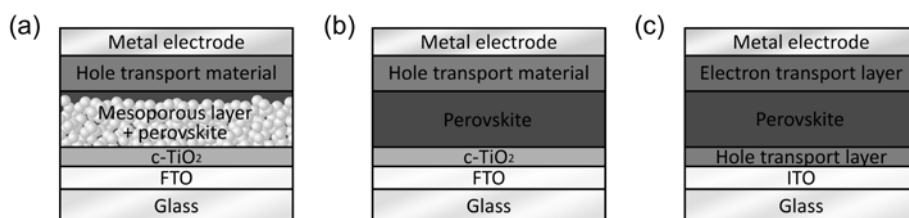


Figure 1.8. Device structures of perovskite solar cells. (a) mesoscopic heterojunction, (b) planar heterojunction with normal structure and (c) planar heterojunction with inverted structure.

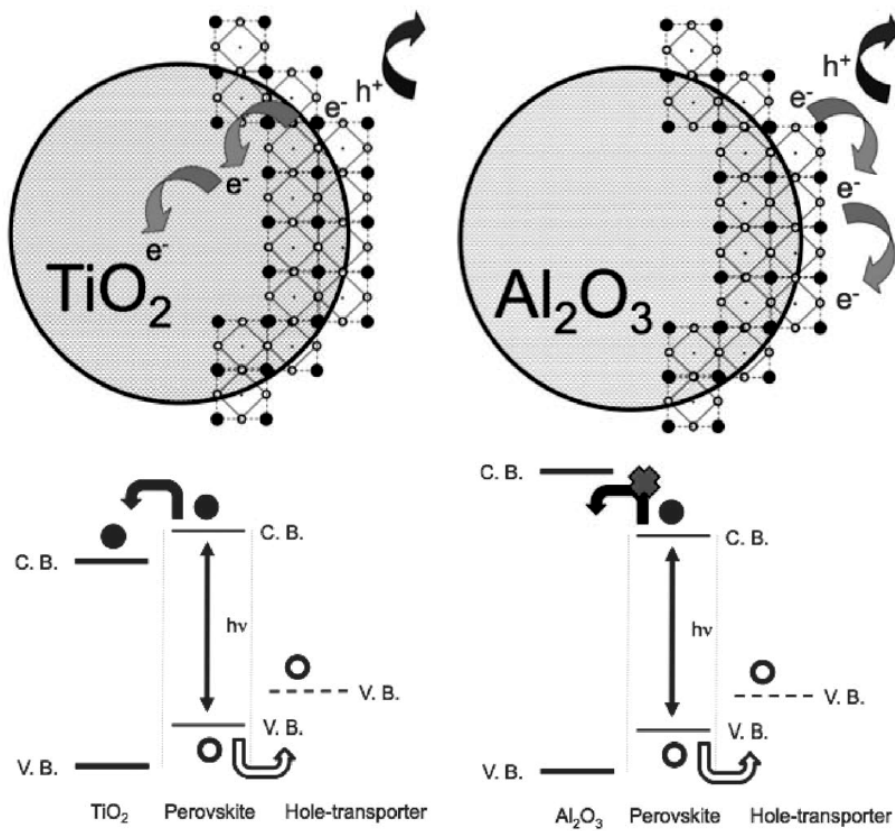


Figure 1.9. Schematic representation of the charge transfer and charge transport in a perovskite-sensitized TiO_2 solar cell and a noninjecting Al_2O_3 -based solar cell. (ref. 68)

1.2 Planar heterojunction perovskite solar cells

1.2.1 Operating principles

Solar cell is a device that converts light energy to electricity. The energy conversion process take place in multiple steps, Step 1—light absorption: When light is incident to photovoltaic device, active material absorbs the light that has higher energy than bandgap of active material. Therefore, for efficient light harvesting, low bandgap materials are needed. $\text{CH}_3\text{NH}_3\text{PbI}_3$ absorbs light up to ~800 nm due to the bandgap energy of 1.5–1.6 eV, indicating that most of the light in visible range can be absorbed by $\text{CH}_3\text{NH}_3\text{PbI}_3$. Step 2—formation of excitons and dissociation into free charge carriers. A photon with larger energy than bandgap of active material excites an electron in valence band to conduction band and produces a exciton. Exciton is dissociated into free electron and free hole due to the built-in electric field. Step 3—Charge transfer. The free charge carriers are transferred to charge transport layer. Step 4—Charge collection. Transferred charges are transported to electrode and generate electric current. When charge extraction rate is overwhelmed by charge generation rate, free charges are accumulated at the interface and deteriorate solar cell performance. Therefore, fast charge transfer from active material and fast charge transport to electrode is essential for the charge transport material.^{70,91–94}

Solar cell performances under illumination are generally characterized by current density–voltage curve (Figure.1.10). Voltage and current density are

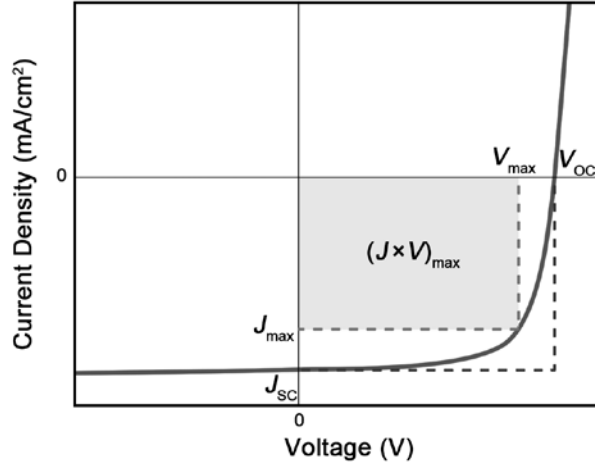


Figure 1.10. current density–voltage curve of solar cells and photovoltaic parameters represented in current density–voltage curve.

represented by X-axis and Y-axis, respectively. Open circuit voltage (V_{OC}) and short circuit current density (J_{SC}) are defined by the points that the curve intersects with X-axis and Y-axis, respectively. Power per unit area is calculated by multiplication of current density and voltage, V_{max} and J_{max} (voltage at maximum power point (V_{max}) and current density at maximum power point (J_{max})). Using these parameters, fill factor (FF) and power conversion efficiency (PCE) are calculated by following formula:

$$FF = \frac{J_{max} \times V_{max}}{J_{SC} \times V_{OC}} \quad (1.2)$$

$$PCE = \frac{V_{OC} \times J_{SC} \times FF}{P_{in}} \quad (1.3)$$

where P_{in} is the incident light power density.

The solar cell parameters are closely related to the charge recombination in bulk perovskite film and at interface between perovskite layer and charge transport layer. Therefore, for high efficiency perovskite solar cell, high quality perovskite film is essential. First, perovskite film with full surface coverage are needed. Good surface coverage of perovskite film reduces the shunting path and also improves the light absorption.⁹⁵⁻⁹⁷ Eperon *et. al.*⁹⁵ reported the improved power conversion efficiency by enhancing the surface coverage. Second, perovskite film with large crystal size are needed. Large perovskite crystal facilitates the transport of photo-generated charge carriers.^{79,98-100} Xiao *et. al.* reported $\text{CH}_3\text{NH}_3\text{PbI}_3$ film composed of micron-sized grains. Large grain reduced number of defect and trap state at grain boundary, therefore it is believed to facilitate charge transport to electrode. Third, low defect density are needed.¹⁰¹⁻¹⁰³ Dong *et. al.* reported that reduced charge mobilities of polycrystalline $\text{CH}_3\text{NH}_3\text{PbI}_3$ film compared to the mobilities of single crystal is due to higher defect density of polycrystalline film than that of $\text{CH}_3\text{NH}_3\text{PbI}_3$ single crystal. Therefore, high quality perovskite film with low defect density facilitates charge transport in the perovskite film. Also, Zhu *et. al.* reported that high defect density may arise $J-V$ hysteresis. Fourth, crystal orientation should be controlled because charge transfer properties are influenced by not only charge transport materials but also $\text{CH}_3\text{NH}_3\text{PbI}_3$ crystal plane. According to the simulation study of Yin *et. al.*,¹⁰⁴ hole and electron transfers at the interface of perovskite are also affected by the crystal plane that forms interface with charge transport layer.

Therefore, the charge transfer properties could be enhance by technique of controlling the crystal orientation and finally the solar cell efficiency can be improved by the enhanced charge transfer properties..

1.2.2 Fabrication methods for organic-inorganic hybrid perovskite film

Fabricating high quality perovskite film is extensively studied for improving the efficiency of perovskite solar cells. Perovskite film properties are easily affected by changing the processing conditions. Most widely studied method is one-step deposition method due to cost-effective, simple and easy process (Figure 1.11). For the one-step deposition method, organic precursor, $\text{CH}_3\text{NH}_3\text{I}$ and inorganic precursor, PbI_2 , are dissolved in an solvent such as N,N-dimethylformamide (DMF), γ -butyrolactone (GBL) or dimethyl

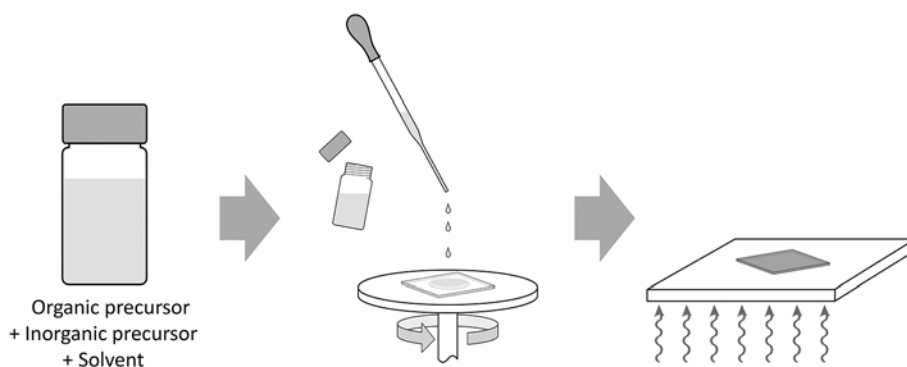


Figure 1.11. Schematic representation of one-step deposition method.

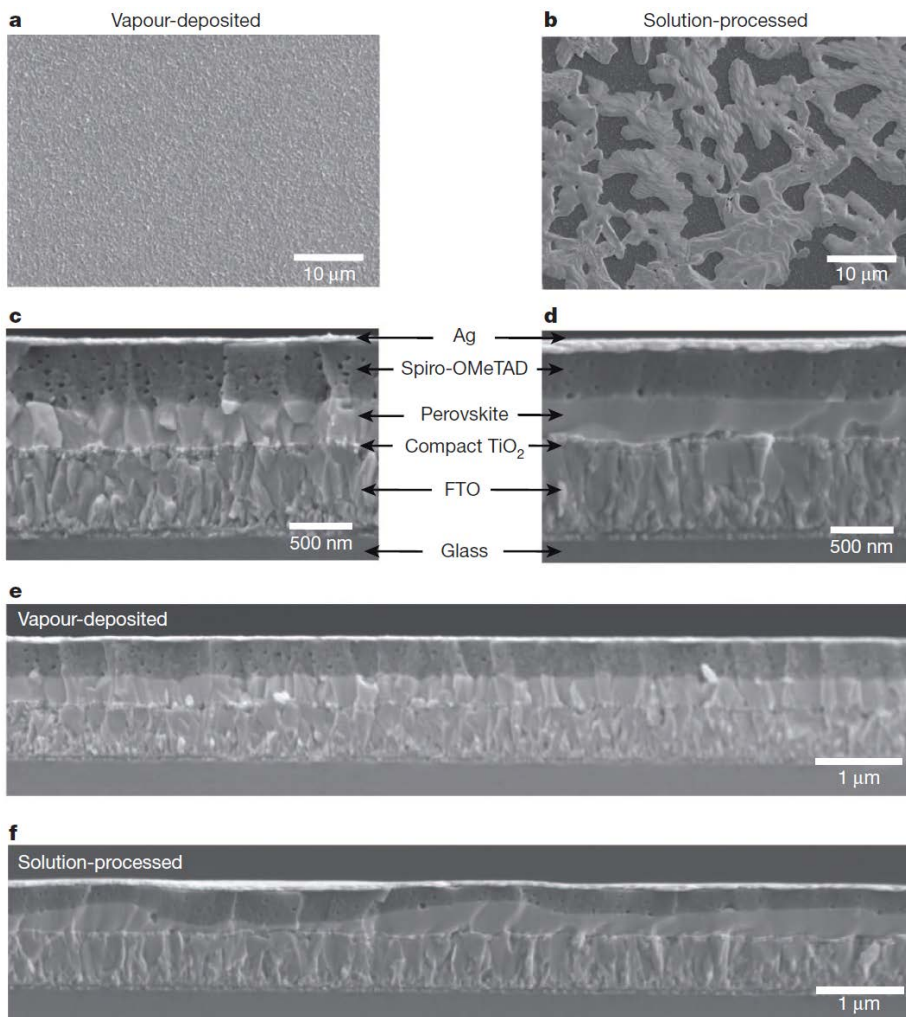


Figure 1.12. SEM images of (a, c, e) vapor-deposited perovskite film and (b, d, f) solution-processed perovskite film. (ref. 71)

sulfoxide (DMSO), and used as a precursor solution. After spin-coating onto the substrate, it is generally heat-treated. In this approach, efficiencies of planar devices are limited due to the poor film formation (Figure 1.12).⁷¹ The films fabricated by one-step deposition exhibit incomplete surface coverage with many pinholes which is induced by extensive crystallization caused by

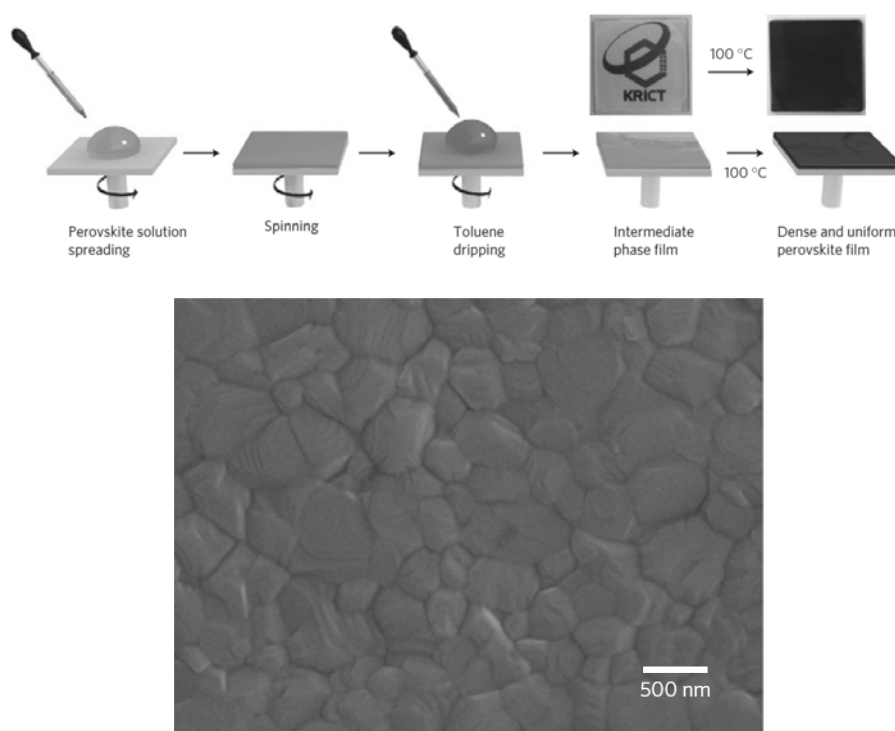


Figure 1.13. Schematic representation of solvent engineering procedure and SEM image of perovskite film fabricated by solvent engineering process. (ref. 98)

solvent evaporation and strong ionic interaction between the metal cations and the halides.^{105,106}

To improve the morphology of organic-inorganic hybrid film, Jeon *et. al.* introduced solvent engineering (Figure 1.13).⁹⁸ $\text{CH}_3\text{NH}_3\text{I}$ and PbI_2 are mixed to 1:1 molar ratio and dissolved in a mixture of DMSO and GBL to 3:7 volume ratio. The precursor solution is spin-coated on substrate and toluene is dropped at certain moment. DMSO was used due to strong coordination property with PbI_2 and toluene was used to extract excess DMSO and GBL. Strong coordination properties between PbI_2 and DMSO impedes the rapid reaction between perovskite precursors. Finally, a highly uniform $\text{CH}_3\text{NH}_3\text{I}$ - PbI_2 -DMSO was formed then changed to $\text{CH}_3\text{NH}_3\text{PbI}_3$ film after heat treatment accompanying the evaporation of DMSO.

Also, Xiao *et. al.* reported fast deposition-crystallization process. 1:1 molar ratio of $\text{CH}_3\text{NH}_3\text{I}$ and PbI_2 were dissolved in DMF and the solution was spin-coated to the substrate. After specific delay time, chlorobenzene (CB) was quickly added to the substrate. Finally, the substrate was heat-treated at 100 °C for 10 min and smooth $\text{CH}_3\text{NH}_3\text{PbI}_3$ film with full surface coverage and micron-sized crystals are fabricated (Figure 1.14). The process of fast deposition-crystallization is similar to the solvent engineering, however, a purpose for choosing solvents are different. When Jeon *et. al.* used DMSO to retard solidification and toluene to extract excess solvent, Xiao *et. al.* used DMF for solvent only to dissolve the precursors and CB to rapidly reduce the solubility of $\text{CH}_3\text{NH}_3\text{PbI}_3$ by extracting DMF and, thereby promote fast nucleation and growth of the crystals in the film. These differences result the

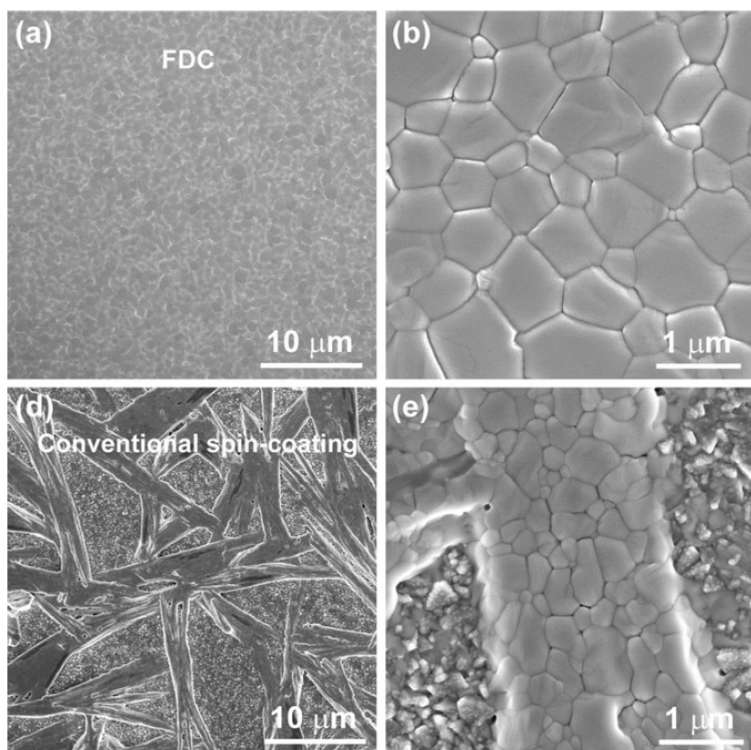
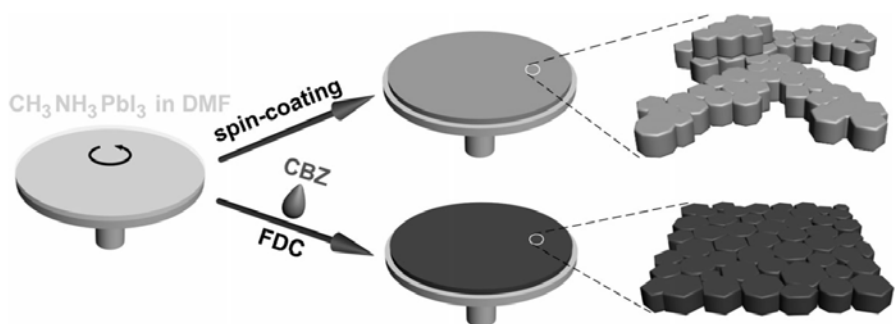


Figure 1.14. Schematic illustration of fast deposition-crystallization (FDC) process and conventional spin-coating process, and SEM images of perovskite films fabricated by FDC process and conventional spin-coating process. (ref. 99)

different appearance of spin-coated film without annealing. The film spin-coated by solvent engineering exhibits yellow color due to the formation of $\text{CH}_3\text{NH}_3\text{I}-\text{PbI}_2-\text{DMSO}$ complex, however, fast deposition-crystallization process results darkening of the film. These results indicate that DMSO coordinates strongly with PbI_2 and prevent the uncontrolled crystallization of $\text{CH}_3\text{NH}_3\text{PbI}_3$. In contrast, DMF is effectively removed by CB dripping and perovskite is instantaneously formed.

Another method to improve the film morphology is solvent annealing. Solvent annealing has been demonstrated in organic solar cells to optimize the morphology of active layer. Xiao *et. al.*¹⁰⁰ applied solvent annealing process to improve $\text{CH}_3\text{NH}_3\text{PbI}_3$ film morphology. When various thicknesses of $\text{CH}_3\text{NH}_3\text{PbI}_3$ films are solvent annealed using DMF at 100 °C, $\text{CH}_3\text{NH}_3\text{PbI}_3$ crystals grow bigger than that in thermally annealed film (Figure 1.15). Interestingly, grain size is similar to the film thickness, *i.e.*, grain size of perovskite is increased according to increase of the film thickness. On the other hand, grain size of thermally annealed perovskite film is independent of the film thickness. Therefore, devices prepared with thermally annealed perovskite film exhibit the decrease of J_{SC} according to the increase of thickness, however, devices prepared with solvent annealed perovskite film exhibit similar J_{SC} with various thicknesses of perovskite film.

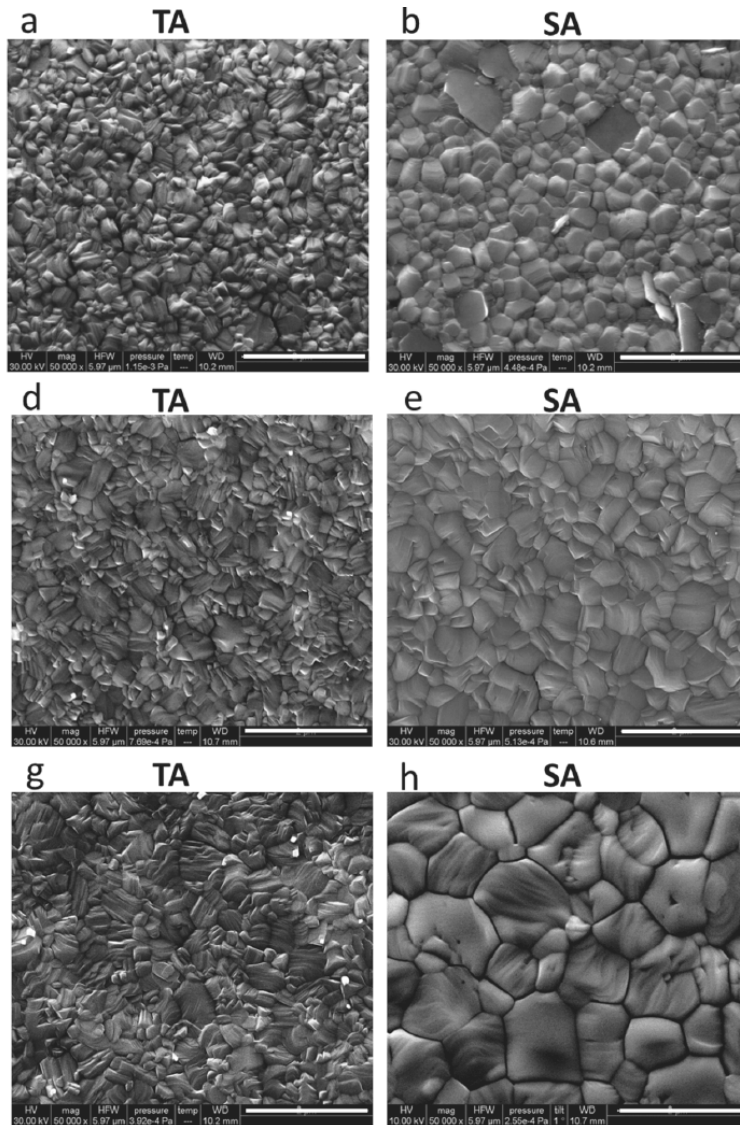


Figure 1.15. SEM images of the thermally annealed perovskite films with thicknesses of (a) 250 nm, (d) 430 nm and (g) 1015 nm, and solvent-annealed perovskite films with thickness of (b) 250 nm, (e) 430 nm and (h) 1015 nm; the scale bars in the SEM micrographs are 2 μm . (ref. 100)

1.3 Objectives of this study

The most important issue of photovoltaics for practical application is to fabricate the cost-effective solar cells. Although crystalline silicon, cadmium telluride and other inorganic absorbers have been developed for high efficiency solar cells, the fabrication cost is still expensive due to vacuum deposition and/or high temperature process. To reduce the fabrication cost, solution processes such as spin-coating, slot-die coating, blade-coating and spray coating have widely been studied. However, the production of these solar cells relies on the use of toxic hydrazine and a high-temperature sintering process. Recently, organic-inorganic hybrid perovskites have intensively been studied as a promising light absorber of solar cells because those have superior properties such as high absorption coefficient,^{27,28} low exciton binding energy,²⁹⁻³³ long charge carrier diffusion length³⁴⁻³⁷ and high charge carrier mobility.^{11,38-40} Furthermore, organic-inorganic hybrid perovskites are suitable for solution and low temperature processing because the precursor materials have enough solubility in several organic solvents (dimethyl formamide, dimethyl sulfoxide, N-methylpyrrolidone, γ -butyrolactone).^{98,100,105,107} Particularly, the power conversion efficiency (PCE) of perovskite solar cells has increased dramatically from the first report of 3.8%⁶⁰ in 2009 to recent 20%.¹⁰⁸

The PCE of perovskite solar cells can be enhanced by minimizing charge recombination in bulk perovskite film and at the interfaces between perovskite and charge transport layers (CTLs). The reduction of charge recombination in

bulk film requires high quality perovskite film with full surface coverage,⁹⁵⁻⁹⁷ large crystal size^{79,98,99} and low defect density,¹⁰¹⁻¹⁰³ while the reduction of charge recombination at the interfaces between perovskite and CTLs needs development of new hole and electron transport materials which can facilitate the charge transport from perovskite layer to electrode.^{70,91-94} According to a recent simulation study,¹⁰⁴ hole and electron transfers at the interfaces in perovskite solar cells are significantly affected by the type of perovskite crystal plane contacting with CTLs. Therefore, the charge recombination at the interface can be reduced when the perovskite crystal plane is properly oriented to the substrate (e.g., CTLs) so as to exhibit good charge transfer at the interface.

First, we report a simple method to fabricate high quality $\text{CH}_3\text{NH}_3\text{PbI}_3$ film to afford high efficiency perovskite solar cells and also elucidate the difference of film formation mechanism depending upon the processing condition. We also propose the optimum processing condition to obtain high quality of perovskite film. The tree-like morphology with many pinholes is developed when the film is fabricated by the conventional one-step deposition, where the solidification due to solvent evaporation is accompanied by crystallization during spin-coating. However, when the spin-coating time is shortened so as to avoid the solidification during spin-coating, $\text{CH}_3\text{NH}_3\text{PbI}_3$ is not crystallized during spin-coating. The liquid film is then crystallized by post heat-treatment at high temperature (110 °C), resulting in flower-like morphology covering the substrate fully without pinholes. Especially, when the perovskite film is fabricated from DMSO solution by spin-coating for

short time followed by heat-treatment, the film exhibits flower-like morphology with large crystal size of tens of micrometers and highly preferred crystal orientation to the substrate. The devices with tree-like morphology exhibit low PCEs due to formation of shunting pathway through pinholes, while those with flower-like morphology show remarkably improved PCEs.

Second, we report fabrication of $\text{CH}_3\text{NH}_3\text{PbI}_3$ films with two different crystal orientations to the substrate along (002)/(110) and (112)/(200) directions, and investigate the effect of crystal orientation on the photovoltaic performance of perovskite solar cells. It has been reported that preferentially oriented perovskite crystals along (110) direction were produced^{73,109–112} when Cl-containing precursor was used to fabricate perovskite film. The crystal orientation is controlled by the use of two different organic precursors ($\text{CH}_3\text{NH}_3\text{Cl}$ and $\text{CH}_3\text{NH}_3\text{I}$). Since the planar heterojunction device has simple interfaces between perovskite and CTLs, the crystal plane of $\text{CH}_3\text{NH}_3\text{PbI}_3$ contacting with CTLs is easily specified, while the $\text{CH}_3\text{NH}_3\text{PbI}_3$ crystal plane contacting with mesoporous TiO_2 in mesoscopic heterojunction device is difficult to be specified. Hence, we fabricate planar heterojunction devices to clearly investigate the effect of crystal orientation on photovoltaic performance of $\text{CH}_3\text{NH}_3\text{PbI}_3$ -based solar cells. Planar heterojunction solar cells can be fabricated as two different device structures, viz. normal structure and inverted structure. When $\text{CH}_3\text{NH}_3\text{PbI}_3$ films with different crystal orientations were introduced into planar heterojunction devices with normal and inverted structures, respectively, we have found that the crystal

orientation to the substrate affects largely the photovoltaic performance of perovskite solar cells due to charge transfer anisotropy of $\text{CH}_3\text{NH}_3\text{PbI}_3$ crystal.

Chapter 2. Experimental Section

2.1 Synthesis

2.1.1 Materials

Methylamine (40% in methanol) was purchased from TCI. Hydroiodic acid (57% w/w aqueous solution stabilized with 1.5% hypophosphorous acid) was purchased from Alfa Aesar. Hydrochloric acid (35–37%) and diethyl ether (99%) were purchased from Samchun Chemical. Ethanol (anhydrous, >99.5%), titanium(IV) chloride (99.9%) and titanium diisopropoxide bis(acetylacetonate) (75 wt% in isopropanol) were purchased from Sigma Aldrich. Benzyl (Extra dry, 98+%) was purchased from Acros Organics. Hydroiodic acid was kept in refrigerator and ethanol, titanium(IV) chloride, titanium diisopropoxide bis(acetylacetonate) and benzyl alcohol were kept in N₂-filled glovebox. All reagents and solvents are used without further purification.

2.1.2 Synthesis

2.1.2.1 Synthesis of organic precursors

Methylammonium iodide: Methylammonium iodide (CH₃NH₃I) was synthesized by reacting equimolar methylamine with hydroiodic acid.

Hydroiodic acid was added dropwise to methylamine solution at 0 °C under stirring. After 2 h, solvent was evaporated in vacuo by rotary evaporator. The product was recrystallized from ethanol and diethyl ether. After filtration, the precipitate was washed with diethyl ether and dried at 60 °C in vacuum oven for 24 h.

Methylammonium chloride: Methylammonium chloride ($\text{CH}_3\text{NH}_3\text{Cl}$) was synthesized by similar process to the synthesis of $\text{CH}_3\text{NH}_3\text{I}$. Methylamine was reacted with equimolar amount of hydrochloric acid. Hydrochloric acid was added dropwise to methylamine solution at 0 °C under stirring. After 2 h, the product was dried by rotary evaporator and recrystallized from ethanol and diethyl ether. After filtration, the precipitate was washed with diethyl ether and dried at 60 °C in vacuum oven for 24 h.

2.1.2.2 Synthesis of titanium dioxide nanoparticles

Synthetic process was performed in the N_2 -filled glovebox. 0.5 ml of titanium(IV) chloride was added slowly to 2 mL of anhydrous ethanol under stirring then the whole content was mixed with 10 mL of anhydrous benzyl alcohol. The solution was heated at 80 °C and translucent suspension was obtained after 6 h. 3 mL of resulting suspension was precipitated in 27 mL of diethyl ether and the precipitate was centrifuged at 5000 rpm to isolate TiO_2 nanoparticles. The isolated TiO_2 was redispersed in ethanol (6 mg/mL) and

14.7 μL of titanium diisopropoxide bis(acetylacetonate) was added to 1 mL of redispersed TiO_2 nanoparticle solution.

2.2 Film fabrication and characterization

2.2.1 Materials

Methylammonium chloride ($\text{CH}_3\text{NH}_3\text{Cl}$) and methylammonium iodide ($\text{CH}_3\text{NH}_3\text{I}$) were dried more than 24 h and then used. Lead iodide (99%) was purchased from Acros Organics and dried in vacuum oven at 240 $^\circ\text{C}$ for 12 h. N,N-Dimethylformamide (anhydrous, 99.8%) and dimethyl sulfoxide (anhydrous, >99.9%) were purchased from Sigma Aldrich and 2-propanol (anhydrous, 99.5+%) was purchased from Alfa Aesar Solvents were used without further purification.

2.2.2 Fabrication method

1.18 mmol of organic precursors ($\text{CH}_3\text{NH}_3\text{I}$ or $\text{CH}_3\text{NH}_3\text{Cl}$) and equimolar amount of PbI_2 were dissolved in 1 ml of DMF or DMSO. The solution was stirred at 60 $^\circ\text{C}$ for 3 h then cooled to room temperature. The cooled solutions were filtered by 0.2 μm PTFE syringe filter before use. Weighing process was carried out in N_2 -filled glovebox. The final precursor solutions were used within 2 days.

Spin-coating process and heat treatment were performed in N_2 -filled glovebox. The final precursor solutions were spin-coated at 3000 rpm and the

substrates were immediately transferred on a hot plate. For fabrication of perovskite film from $\text{CH}_3\text{NH}_3\text{Cl}$ and PbI_2 , $\text{CH}_3\text{NH}_3\text{I}$ solution (5 mg/mL in isopropanol) was additionally spin-coated at 3000 rpm for 30 s and the substrate was annealed at 110 °C for 120 s. $\text{CH}_3\text{NH}_3\text{I}$ was treated twice to remove residual $\text{CH}_3\text{NH}_3\text{PbCl}_3$ in $\text{CH}_3\text{NH}_3\text{PbI}_3$.

2.2.3 Characterization method

OM and In-situ OM images were obtained by Leica MPS 30 microscope and SEM images were obtained. XRD patterns were obtained by X-ray diffractometer (D8 Advance, Bruker) using $\text{Cu-K}\alpha^{1,2}$ radiation ($\lambda = 1.5418 \text{ \AA}$) at a scan rate of 2° min^{-1} and morphology of perovskite films were characterized using field-emission scanning electron microscopy (SU70, Hitachi or JSM-6700F, JEOL). Information of tetragonal $\text{CH}_3\text{NH}_3\text{PbI}_3$ crystal structure was obtained in literature¹¹ and VESTA was used to visualize the crystal structure clearly. Grazing incidence X-ray diffraction (GIXD) measurements were conducted at PLS-II 9A U-SAXS and 6D C&S UNIST-PAL beam line of Pohang Accelerator Laboratory in Korea. The X-rays coming from the in-vacuum undulator (IVU) are monochromated (wavelength, $\lambda = 1.12 \text{ \AA}$ for PLS-II 9A U-SAXS and $\lambda = 1.2398 \text{ \AA}$ for 6D C&S UNIST-PAL) using a Si(111) double-crystal monochromator and focused horizontally and vertically ($300 \text{ (H)} \times 30 \text{ (V)} \mu\text{m}^2$ in FWHM @sample position) using K-B type mirror system. GIXD sample stage is equipped with a 7-axis motorized stage for the fine alignment of sample and the incidence angle of X-ray beam

was set to 0.08° for PLS-II 9A U-SAXS and 0.2° for 6D C&S UNIST-PAL. GIXD pattern were recorded with a 2D CCD detector and X-ray irradiation time was 1.5 s for PLS-II 9A U-SAXS and 120 s for 6D C&S UNIST-PAL. Diffraction angles were calibrated by a pre-calibrated sucrose (Monoclinic, P21, $a = 10.8631 \text{ \AA}$, $b = 8.7044 \text{ \AA}$, $c = 7.7642 \text{ \AA}$, $\beta = 102.938^\circ$)¹¹³ and the sample-to-detector distance was about 226.6 mm for PLS-II 9A U-SAXS and 235.5 mm for 6D C&S UNIST-PAL. JASCO FT-IR-660 plus was used to collect FT-IR spectra. The spectra of DMF and DMSO were measured in liquid phase and the spectra of PbI₂-DMF, CH₃NH₃I-PbI₂-DMF, PbI₂-DMSO and CH₃NH₃I-PbI₂-DMSO were measured in powder samples using KBr pellet. PL lifetimes were measured by using 400 nm, second harmonic generated Ti:Sapphire femtosecond laser (MaiTai, Spectra Physics) as excitation source and time-correlated single photon counting module (MPD-PDM Series DET-40 photon counting detector and Pendulum CNT-91 frequency counter) combined with monochromator as detector. The parameter of PL decay were obtained by fitting the spectra with a biexponential decay function, $I(t) = A_1 \exp(-t/\tau_1) + A_2 \exp(-t/\tau_2)$. Average lifetime, τ_{ave} were calculated by equation, $\tau_{ave} = A_1\tau_1 + A_2\tau_2$.¹¹⁴

2.3 Device fabrication and measurement

2.3.1 Materials

ITO coated glass ($10 \text{ } \Omega \text{ sq}^{-1}$) was purchase from KETI. Poly(3,4-

ethylenedioxy-thiophene):poly(styrenesulfonate) (PEDOT:PSS, Clevios P VP AI 4083) was purchased from Heraeus. [6,6]-Phenyl-C61-butyric acid methyl ester (PC₆₁BM, 99.5%) was purchased from nano-C and 2,2',7,7'-tetrakis(N,N-di-p-methoxyphenylamino)-9,9'-spirobifluorene (spiro-OMeTAD, 99.9%) was purchased from EM index. 4-*tert*-Butylpyridine (96%), Bis(trifluoromethane)sulfonimide lithium salt (99.95%), chloroform (anhydrous, >99%), chlorobenzene (anhydrous, 99.8%) and acetonitrile (anhydrous, 99.8%) are purchased from Sigma aldrich. Aluminum (99.999%) and Gold (99.99%) are purchased from Taewon scientific. Calcium (99.5%) are purchased from Alfa aesar. Acetone (99.7%) and 2-propanol (99.5%) are purchased from Samchun chemical. 10 mg of PC₆₁BM was dissolved in 1 mL of anhydrous chloroform. 72.3 mg of spiro-OMeTAD was dissolved in 1 mL of anhydrous chlorobenzene with an additive of 17.5 μ l of Bis(trifluoromethane)sulfonimide lithium salt solution (520 mg/mL in acetonitrile) and 28.8 μ l 4-*tert*-butylpyridine. 6 mg/mL of TiO₂ dispersion in anhydrous ethanol with an additive of 14.7 μ L of titanium diisopropoxide bis(acetylacetonate) was diluted 2 times for spin-coating on ITO and 4 times for spin-coating on PC₆₁BM.

2.3.2 Solar cell device fabrication

2.3.2.1 Fabrication of device with normal structure

The ITO coated glass was cleaned by stepwise sonication in acetone and isopropanol for 30 min each. After complete drying at 120 °C in convection

oven, the ITO coated glass was treated with UV-ozone for 15 min. TiO₂ solution was spin-coated at 3000 rpm for 40 s onto the ITO and the substrate was then annealed at 150 °C for 30 min in ambient condition. After annealing, the substrate was immediately transferred to a N₂-filled glovebox. CH₃NH₃PbI₃ and spiro-OMeTAD layer were deposited in a N₂-filled glovebox. DMSO precursor solution was spin-coated at 3000 rpm for 15 s and the substrate was immediately transferred on a hot plate at 110 °C for 30 s. For fabrication of perovskite film from CH₃NH₃Cl and PbI₂, CH₃NH₃I solution (5 mg/ml in 2-propanol) was additionally spin-coated at 3000 rpm for 30 s and the substrate was annealed at 110 °C for 120 s. CH₃NH₃I was treated twice to remove residual CH₃NH₃PbCl₃ in 5 CH₃NH₃PbI₃. Spiro-OMeTAD solution (72.3 mg/ml in chlorobenzene) with 17.5 μl of Li-bis(trifluoromethanesulfonyl)imide (520 mg/ml in acetonitrile) and 28.8 μl 4-tert-butylpyridine was spin-coated on the perovskite layer at 3000 rpm for 30 s. Finally, Au electrodes was deposited by thermal evaporation under vacuum (<10⁻⁶ Torr) through a shadow mask to give a device area of 0.1 cm².

2.3.2.2 Fabrication of device with inverted structure

The ITO coated glass was cleaned by stepwise sonication in acetone and isopropanol for 30 min each. After complete drying at 120 °C, the ITO coated glass was treated with UV-ozone for 15 min. PEDOT:PSS was spin-coated at 3000 rpm for 40 s onto the ITO and the substrate was annealed at 150 °C for 30 min in ambient condition. After annealing, the substrate was immediately

transferred to a N₂-filled glovebox, and CH₃NH₃PbI₃ and PCBM layers were successively deposited in a N₂-filled glovebox. DMSO precursor solution was spin-coated at 3000 rpm for 15 s and the substrate was immediately transferred on a hot plate at 110 °C for 30 s. For fabrication of perovskite film from CH₃NH₃Cl and PbI₂, CH₃NH₃I solution (5 mg/mL in 2-propanol) was additionally spin-coated at 3000 rpm for 30 s and the substrate was annealed at 110 °C for 120 s. CH₃NH₃I was treated twice to remove residual CH₃NH₃PbCl₃ in CH₃NH₃PbI₃. PC₆₁BM solution (10 mg/ml in chloroform) was spin-coated onto the perovskite layer at 3000 rpm for 30 s and TiO₂ solution was spin-coated on the PCBM layer at 3000 rpm for 30 s. Finally, Al electrodes was deposited by thermal evaporation under vacuum (<10⁻⁶ Torr) through a shadow mask to give a device area of 0.1 cm².

2.3.3 Solar cell performance measurement and device characterization

J-*V* curves of photovoltaic cells were obtained using a computer-controlled Keithley 4200 source measurement unit under AM 1.5G (100 mW cm⁻²) simulated by an Oriel solar simulator (Oriel 91160A). The light intensity was calibrated using a NREL-certified photodiode prior to each measurement. Ranges of bias sweep were from 1.5 V to -0.5 V for normal cells and from 2 V to -1 V for inverted cells. Data points were placed with an interval of 0.01 V and delay times were 0.1 s for normal cells and 0.01 s for inverted cells. The external quantum efficiency (EQE) was measured using Polaronix K3100 measurement system (Mcsience). EQE was measured with

a range from 300 nm to 900 nm. Data points were placed with an interval of 20 nm and calculated average value of 5 times measurements. The light intensity at each wavelength was calibrated with a standard single-crystal Si cell. Impedance spectroscopic measurements were carried out using an impedance analyzer (Bio-Logic VMP3) with various potential from 0 to 0.8 V with an interval of 0.2 V in dark. AC 10 mV perturbation was applied with a frequency from 1 MHz to 100 Hz. The obtained spectra were fitted with EC-Lab software.

Chapter 3. Results and Discussion

3.1 Two different mechanisms of $\text{CH}_3\text{NH}_3\text{PbI}_3$ film formation and its effect on photovoltaic properties

3.1.1 Synthesis and characterization

Organic-inorganic hybrid perovskites are easily produced by fast reaction of organic precursor and inorganic precursor. Molecules of organic precursor penetrate into inorganic frameworks and change the structure (e.g. from edge sharing of PbI_6 octahedron in PbI_2 to corner sharing of $\text{CH}_3\text{NH}_3\text{PbI}_3$). For fabrication of methylammonium lead triiodide ($\text{CH}_3\text{NH}_3\text{PbI}_3$), methylammonium iodide ($\text{CH}_3\text{NH}_3\text{I}$) as an organic precursor and lead(II) iodide (PbI_2) as a inorganic precursor are widely use and synthesis of $\text{CH}_3\text{NH}_3\text{I}$ was report in many studies.^{68,76,80,115–119} Synthesized $\text{CH}_3\text{NH}_3\text{I}$ through the method that was explained in experimental section was confirmed by ^1H NMR (Figure 3.1.). Protons at methyl and ammonium groups are detected at 2.37 ppm and 7.48 ppm, respectively and two peaks show same integration area due to the same number of protons at methyl and ammonium group.

3.1.2 Photovoltaic properties

It has been reported that the perovskite films processed by one-step

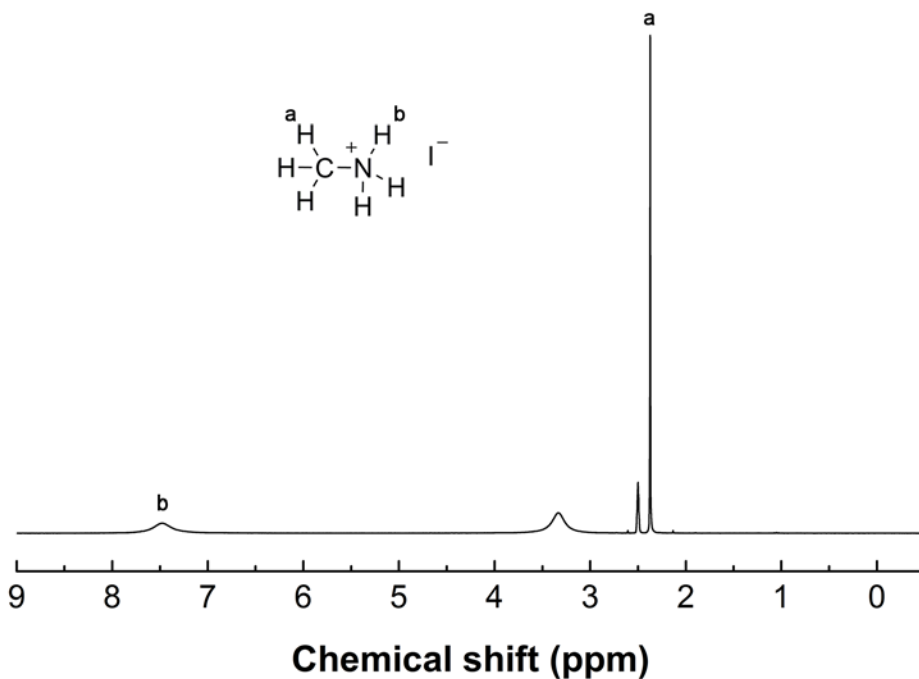


Figure 3.1. ^1H NMR spectrum of methylammonium iodide.

deposition have low surface coverage with many pinholes due to uncontrolled solidification during spin-coating process.⁷¹ To overcome this problem in this work, the spin-coating time is controlled when the perovskite films are fabricated by one-step deposition of precursor solution ($\text{CH}_3\text{NH}_3\text{I}:\text{PbI}_2 = 1:1$ molar ratio) using two different solvents, DMF and DMSO. When the current density–voltage (J – V) curves are measured with an OPV-type device configuration of glass/ITO/PEDOT:PSS/ $\text{CH}_3\text{NH}_3\text{PbI}_3/\text{PC}_{61}\text{BM}/\text{Ca}/\text{Al}$ under

AM1.5G illumination, the open-circuit voltage (V_{OC}), short-circuit current (J_{SC}) and fill factor (FF) are largely improved as the spin-coating time is decreased (Figure.3.2 and Table 3.1). The power conversion efficiency (PCE) of devices fabricated from DMF solution increases from 0.55% to 6.95% as the spin-coating time is decreased from 30 s to 3 s, and the PCE of devices fabricated from DMSO solution also increases from 0.22% to 13.85% as the spin-coating time is decreased from 90 s to 15 s, indicating that the device

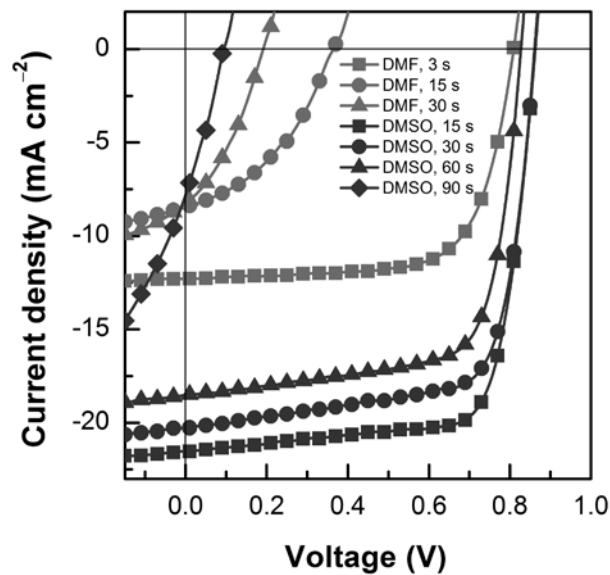


Figure 3.2. J - V curves of $\text{CH}_3\text{NH}_3\text{PbI}_3$ perovskite solar cells. The $\text{CH}_3\text{NH}_3\text{PbI}_3$ films in the devices are prepared by spin-coating the DMF and DMSO solutions with different spin-coating times, then are thermally treated at $110\text{ }^\circ\text{C}$ for 30 s.

Table 3.1. Photovoltaic properties of CH₃NH₃PbI₃ perovskite solar cells depending on solvent and spin-coating time

Solvent	Spin-coating time (s)	V _{oc} (V)	J _{sc} (mA cm ⁻²)	FF	PCE ^[a] (%)	Standard deviation
DMF	3	0.81	12.31	0.70	6.95 (6.68)	0.21
DMF	15	0.36	8.45	0.41	1.23 (0.79)	0.29
DMF	30	0.19	8.28	0.35	0.55 (0.47)	0.09
DMSO	15	0.86	21.55	0.75	13.85 (13.23)	0.37
DMSO	30	0.86	20.31	0.72	12.51 (12.17)	0.38
DMSO	60	0.83	18.50	0.71	10.91 (10.53)	0.29
DMSO	90	0.09	7.82	0.31	0.22 (0.16)	0.03

^[a] Average PCE values based on 10 devices are indicated in parentheses.

performance becomes better as the spin-coating time is decreased. EQE spectra of best-performed devices from DMF and DMSO solutions are shown in Figure 3.3. It should be noted here that all devices are heat-treated at 110 °C for 30 s after spin-coating. Furthermore, the PCEs of the devices fabricated from the best processing condition exhibit small standard deviation less than 0.4%, indicating that highly efficient perovskite solar cells can be obtained

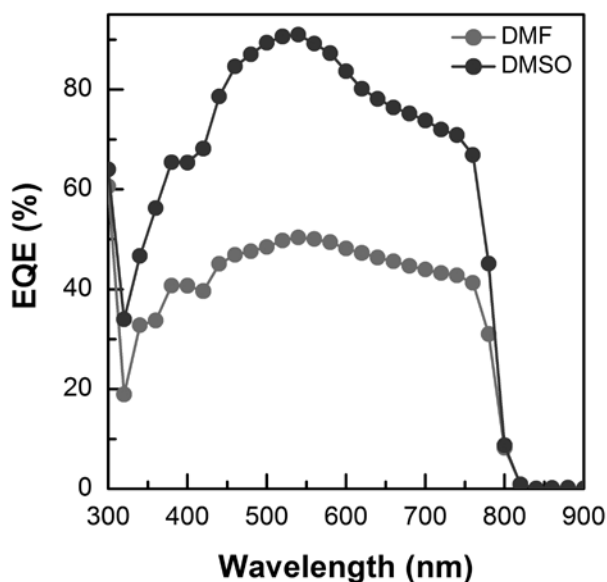


Figure. 3.3. External quantum efficiency spectra of the best cells fabricated from DMF and DMSO solution. The $\text{CH}_3\text{NH}_3\text{PbI}_3$ films are prepared by spin-coating at 3000 rpm for 3 s (DMF) and 15 s (DMSO), respectively and are thermally treated at 110 °C for 30 s.

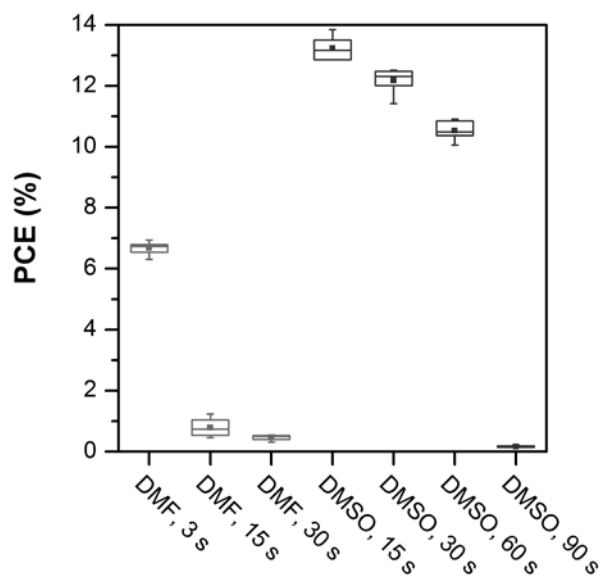


Figure 3.4. Statistical analysis of the power conversion efficiencies of the $\text{CH}_3\text{NH}_3\text{PbI}_3$ perovskite solar cells depending on solvent and spin-coating time.

reproducibly by simply reducing the spin-coating time (Table 3.1 and Figure 3.4). Also, it is interesting to observe that J - V curves of our devices are hysteresis-less (Figure 3.5).

3.1.3 Mechanisms of $\text{CH}_3\text{NH}_3\text{PbI}_3$ film formation

To identify the reason why the devices show the performance difference depending upon the spin-coating time, we monitored the change of film state with the spin-coating time. It should be mentioned here that the effect of

substrate on the morphology of $\text{CH}_3\text{NH}_3\text{PbI}_3$ film is excluded because PEDOT:PSS layer is coated on the substrate before $\text{CH}_3\text{NH}_3\text{PbI}_3$ is deposited in device fabrication process. As shown in Figure 3.6, the liquid film from DMF solution starts to solidify between 5–10 s after spin-coating. The color of liquid film before solidification is yellow (<5 s), which is the same color as the color of DMF bulk solution, and after solidification (≥ 10 s) the color changes from yellow to white and subsequently to brown. The color change

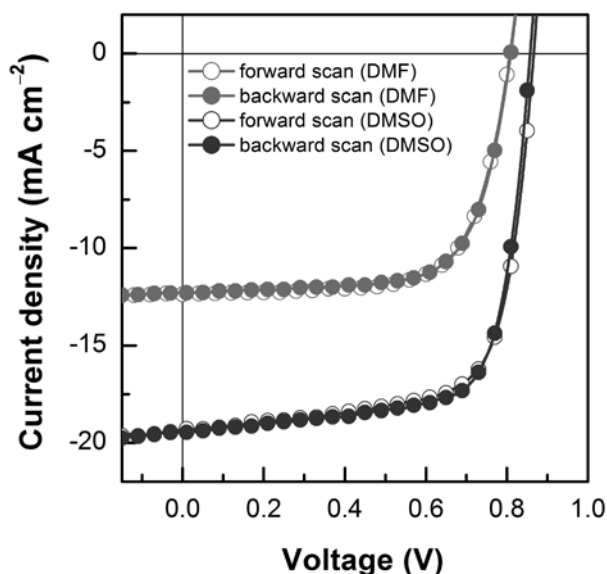


Figure 3.5. J - V hysteresis of perovskite solar cells fabricated from DMF and DMSO solution. The $\text{CH}_3\text{NH}_3\text{PbI}_3$ films are prepared by spin-coating at 3000 rpm for 3 s (DMF) and 15 s (DMSO), respectively and are thermally treated at 110 °C for 30 s.

by solidification is also observed in the film processed by DMSO solution. The color of film spin-coated from DMSO solution maintains yellow until 60 s of spin-coating time after which the color is changed to white due to solidification. It should be noted here that the liquid film from DMSO solution requires longer spin-coating time to solidify than DMF solution due to higher boiling temperature (189 °C) and lower vapor pressure (0.42 mmHg) than those of DMF (153 °C, 2.7 mmHg). Considering that the solidification

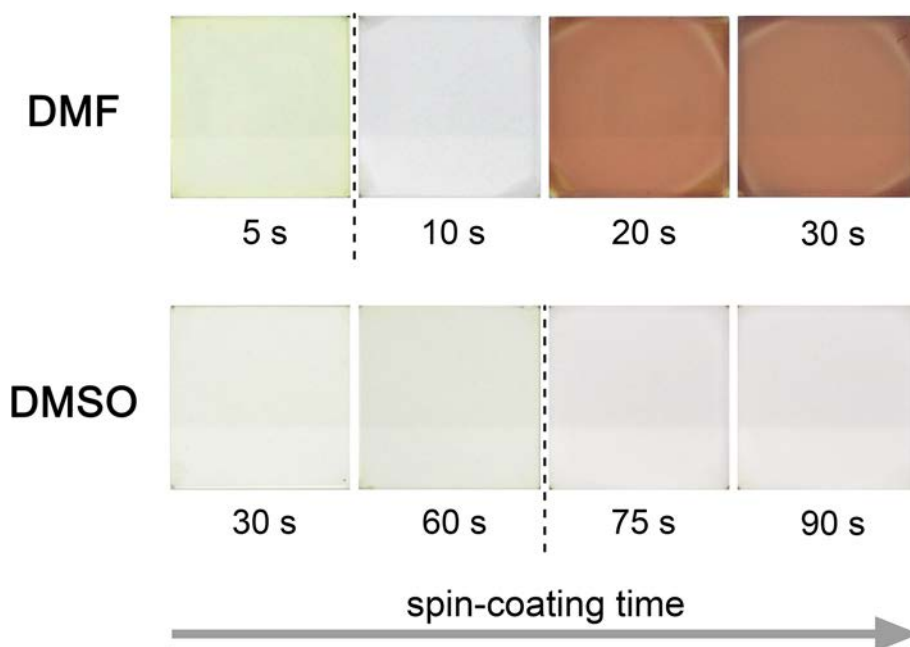


Figure 3.6. The change of film state with different spin-coating time using DMF and DMSO solutions before heat treatment. Dashed lines denote the point at which the liquid film starts to solidify.

during spin-coating is closely related to the device performance, it is concluded that the device performance becomes better when the spin-coating time is short so as to prevent solidification of liquid film during spin-coating.

When the films spin-coated for various spin-coating times are thermally treated at 110 °C for 30 s to complete the formation of $\text{CH}_3\text{NH}_3\text{PbI}_3$ solid film, the films show different morphologies depending upon the spin-coating time, as shown in optical microscopy (OM) images of Figure 3.7 and Figure 3.8. Independent of processing solvent, heat-treatment of liquid films develops the flower-like morphology with circular domain shape (Figure 3.7a and Figure 3.8a–c), while the heat-treatment of films after solidification during spin-coating develops film morphology containing many pinholes (Figure 3.7b–d and Figure 3.8d).

The microscopic morphologies of perovskite films as observed by scanning electron microscopy (SEM) also show that the films spin-coated for short time, which is not enough to solidify the liquid film, exhibit the flower-like morphology after heat-treatment (Figure 3.9a and 3.9b) while the films spin-coated for longer times exhibit tree-like morphology containing many pinholes (Figure 3.9c and 3.9d). Magnification of SEM images reveals that the crystal domains in all films are not composed of a single crystal but many micro-crystals (insets of Figure 3.9). Another important feature is that the size of individual $\text{CH}_3\text{NH}_3\text{PbI}_3$ crystallites grown from DMSO solution is much larger than that grown from DMF solution. Especially, the film with flower-like morphology as developed from DMSO solution consists of large crystallites with the scale of tens of micrometers and good surface coverage.

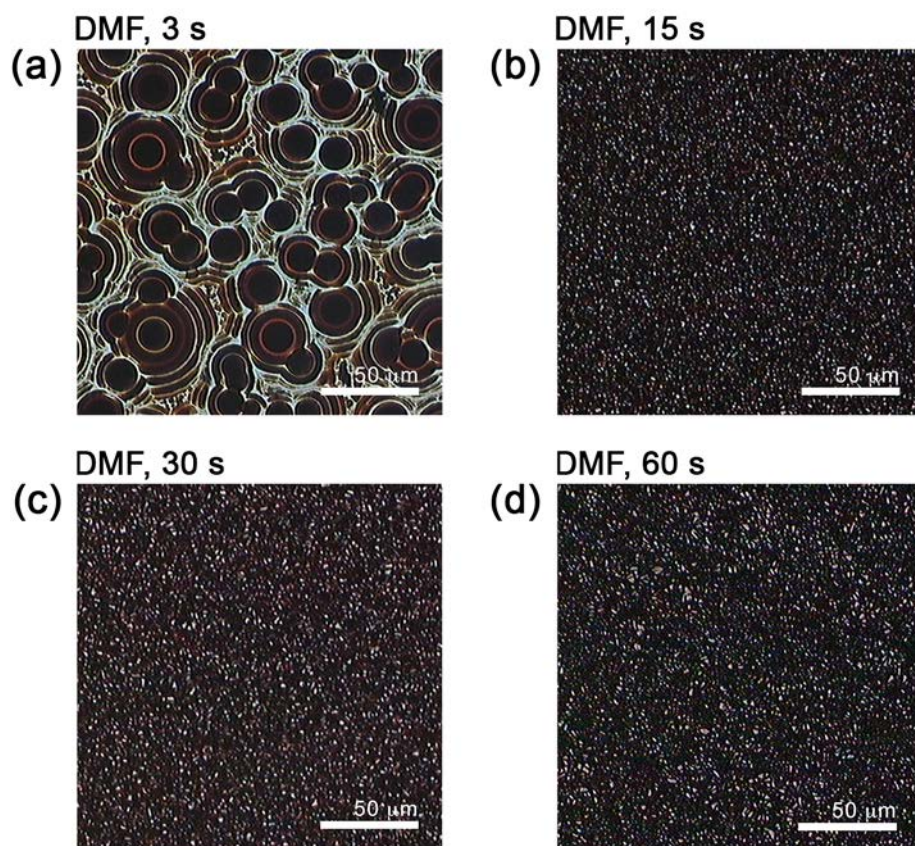


Figure 3.7. OM images of $\text{CH}_3\text{NH}_3\text{PbI}_3$ films formed from DMF solution with various spin-coating time. All films are spin-coated at 3000 rpm and are thermally treated at 110 °C for 30 s immediately after spin-coating.

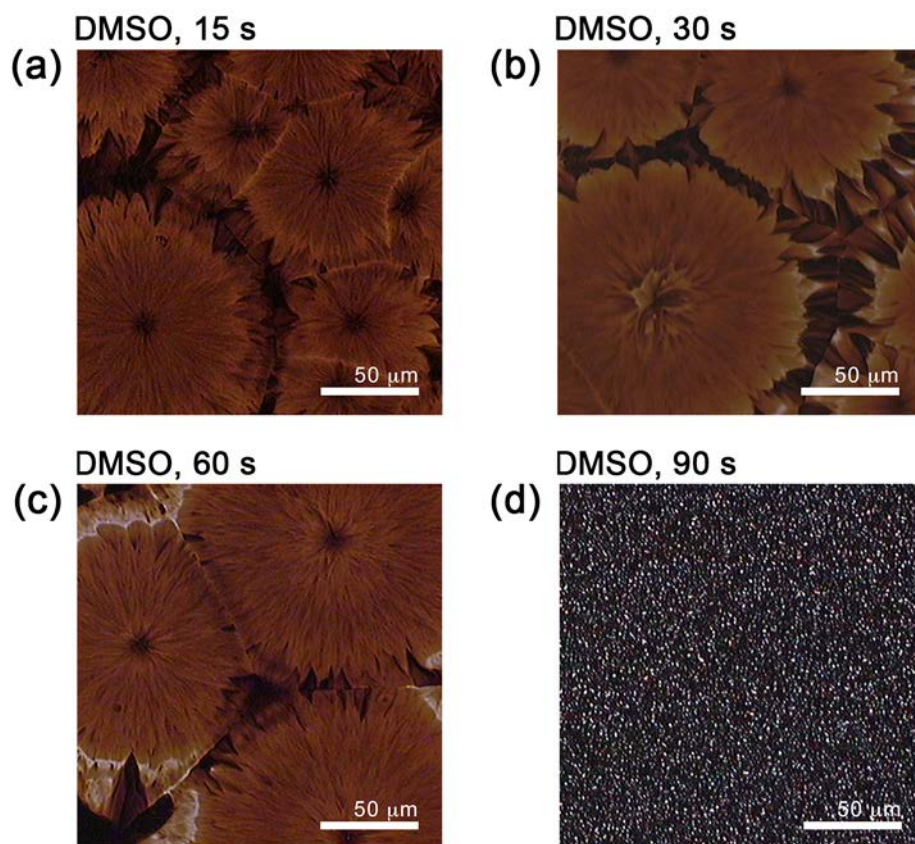


Figure 3.8. OM images of $\text{CH}_3\text{NH}_3\text{PbI}_3$ films formed from DMSO solution with various spin-coating time. All films are spin-coated at 3000 rpm and are thermally treated at $110\ ^\circ\text{C}$ for 30 s immediately after spin-coating.

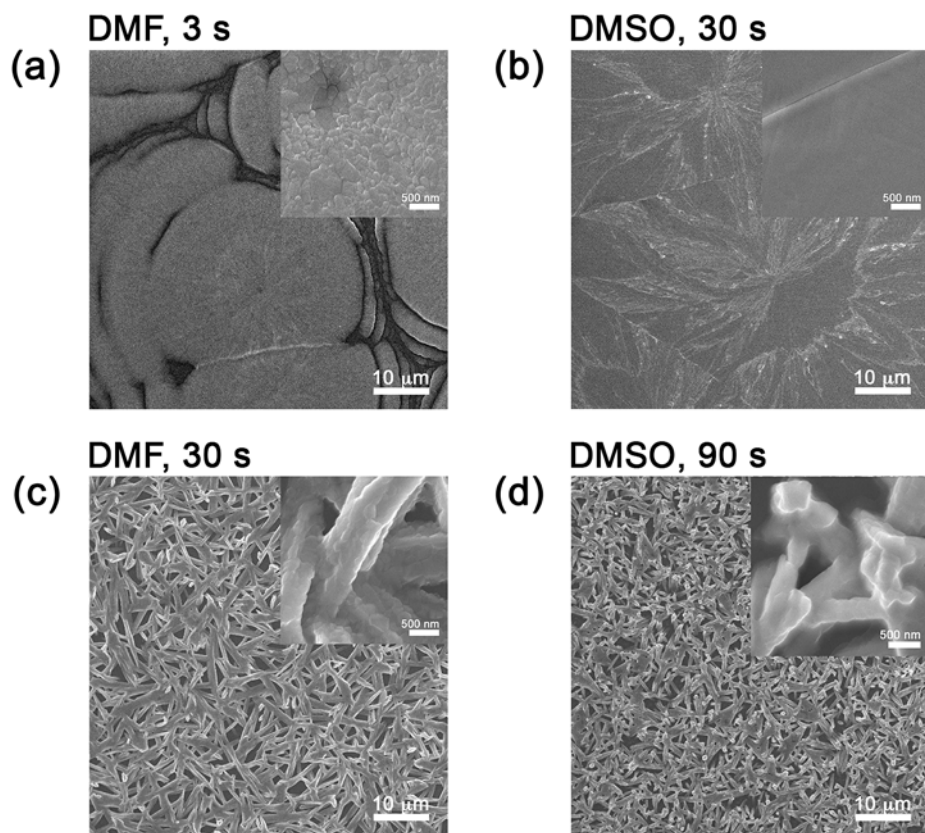


Figure 3.9. SEM images of $\text{CH}_3\text{NH}_3\text{PbI}_3$ films with (a, b) flower-like and (c, d) tree-like morphology fabricated from (a, c) DMF and (b, d) DMSO solution. All films are thermally treated at 110 °C for 30 s immediately after spin-coating.

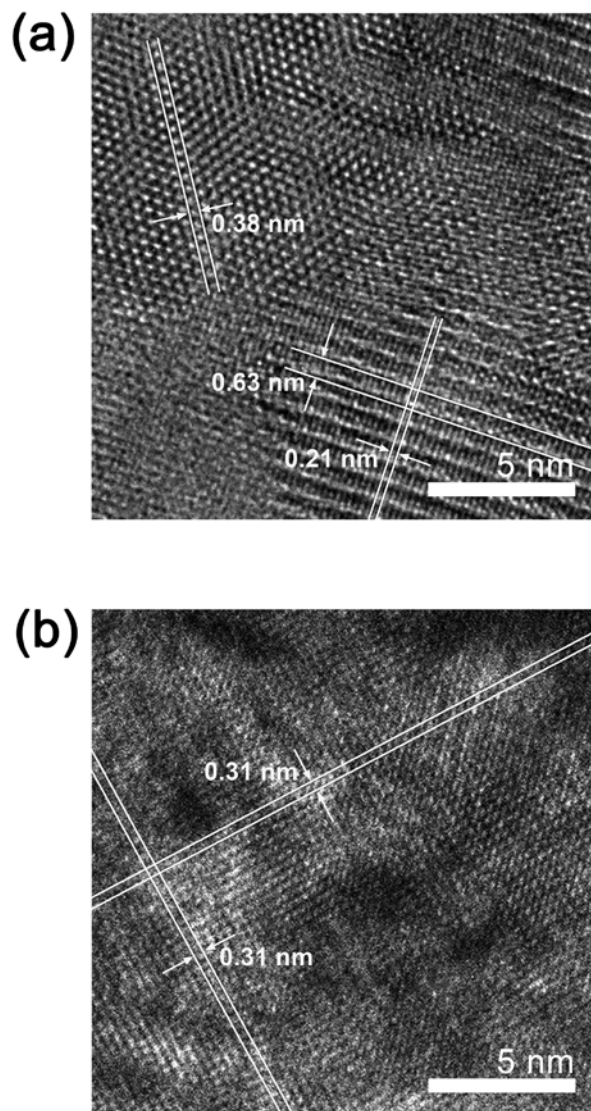


Figure 3.10. HRTEM images of $\text{CH}_3\text{NH}_3\text{PbI}_3$ films with flower-like morphology. The films are spin-coated at 3000 rpm and are thermally treated at 110 °C for 30 s immediately after spin-coating.

When the crystal morphologies of films are investigated by high-resolution transmission electron microscopy (HRTEM), as shown in Figure. 3.10, the HRTEM image of film with flower-like morphology, as developed from DMSO solution, reveals a large crystal plane with the lattice fringe indexed only as (004) plane, whereas the image of film with flower-like morphology fabricated from DMF solution shows multiple crystal planes such as (201) and (410). The multiple crystal planes indicate that the film fabricated from DMF solution is composed of smaller $\text{CH}_3\text{NH}_3\text{PbI}_3$ crystallites with different crystal orientation (Figure 3.10a), while the HRTEM image of film from DMSO solution exhibits only one crystal plane (Figure 3.10b). This is a direct evidence that the crystallites in the film fabricated from DMSO solution are much larger in crystal size than the crystallites in the film fabricated from DMF solution, although the two films show flower-like morphology.

The above observation leads us to conclude that long spin-coating time enough to solidify the liquid film develops tree-like morphology with many pinholes which may provide shunting pathway and thus reduce the solar cell efficiency, while short spin-coating time not enough to solidify during spin-coating develops flower-like morphology with good film coverage which affords high photovoltaic performance. Specifically, when the film with flower-like morphology, as spin-coated for short time (15 s) from DMSO solution, is used as active layer, the device exhibits much higher PCE (13.85%) than the device (PCE = 0.22%) fabricated by spin-coating of DMSO solution for long time (90 s). The higher efficiency of the device fabricated from short-time spin-coating of DMSO solution may arise from larger crystal

size and preferred crystal orientation in the film (which will be discussed in the next section), which facilitates the charge transport and reduces defect density. To reveal the reason for high efficiency of the device with flower-like morphology, we measured bulk recombination times of devices using an impedance analyzer.¹⁰³ Devices with flower-like morphology show longer bulk recombination time (which may afford higher efficiency) than devices with tree-like morphology (Figure 3.11) probably due to larger crystal size of flower-like morphology, indicating that the charge recombination in the bulk film is closely related to the film morphology.

To reveal the origin for the difference between tree-like and flower-like morphologies, the development of morphology in liquid films, prepared by controlling the spin-coating time (3 s for DMF solution and 30 s for DMSO solution) to prevent solidification, is monitored by in-situ OM, as shown in Figure 3.12 and Figure 3.13. When the liquid film from DMF solution is dried at room temperature, the colorless crystals start to grow at 60 s of standing and grow slowly for the next 20 s. When the dried film was heat-treated at 110 °C, the color of crystals is changed from colorless to dark brown, retaining the tree-like morphology. The same phenomenon is also observed in the film spin-coated from DMSO solution at room temperature, indicating that the tree-like morphology is developed by growth of colorless crystals (Figure 3.12). However, when liquid films spin-coated from both DMF and DMSO solutions are heat-treated at 110 °C immediately after short spin-coating times, the color of nuclei is dark brown and the crystals rapidly grow in circular shape (Figure 3.13).

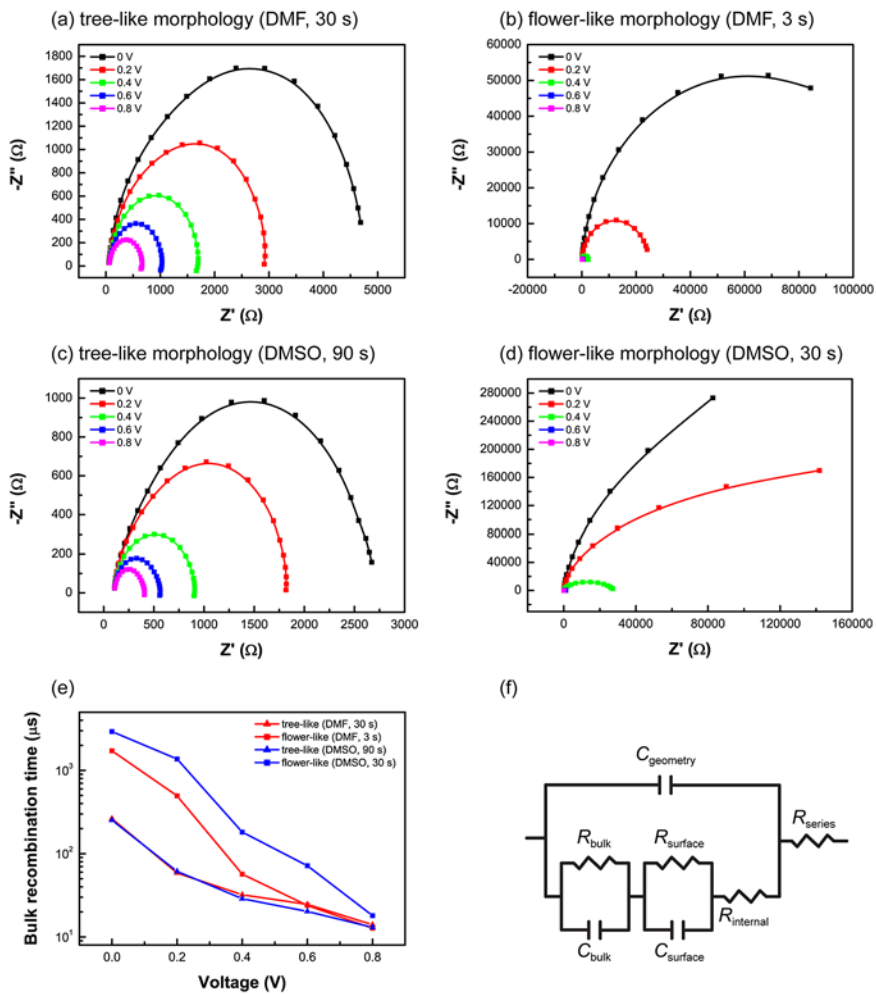


Figure 3.11. Nyquist plots of $\text{CH}_3\text{NH}_3\text{PbI}_3$ solar cells with (a–d) different morphology and processing solvent under different applied voltage. (e) Bulk recombination times are calculated by fitting the Nyquist plot using (f) the equivalent circuit.

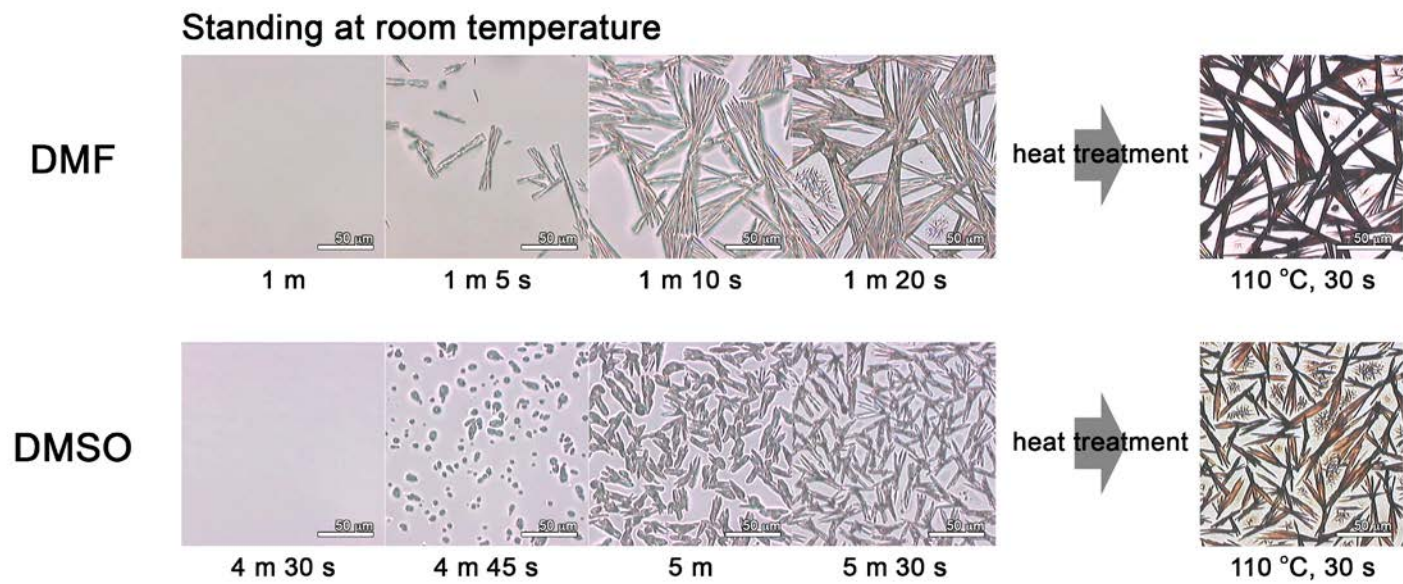


Figure 3.12. In-situ OM images of crystal growth in liquid films under room temperature. The liquid films prepared from DMF and DMSO solutions are spin-coated for 3 s and 30 s, respectively.

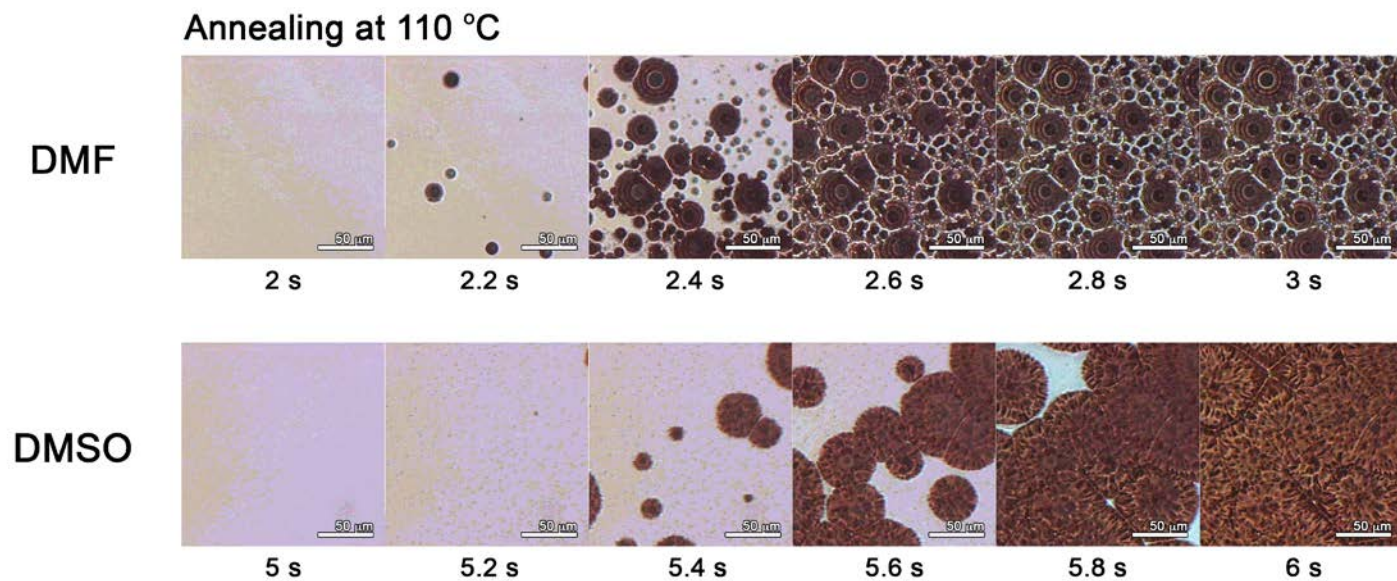


Figure 3.13. In-situ OM images of crystal growth in liquid films at 110 °C. The liquid films prepared from DMF and DMSO solutions are spin-coated for 3 s and 30 s, respectively.

When the crystal structure of colorless crystals in the film dried at room temperature was identified by X-ray diffraction (XRD), as shown in Figure 3.14, the XRD pattern of dried film from DMSO solution exhibits several primary peaks between $5\text{--}10^\circ$, which are the same as the diffraction peaks of $\text{CH}_3\text{NH}_3\text{I-PbI}_2\text{-DMSO}$ complex,⁹⁸ indicating that the colorless crystals are formed from $\text{CH}_3\text{NH}_3\text{I-PbI}_2\text{-DMSO}$ complex. However, the crystal structure of $\text{CH}_3\text{NH}_3\text{I-PbI}_2\text{-DMF}$ complex has not been reported, although it was reported that DMF molecule coordinates to Pb in PbI_2 to form $\text{PbI}_2\text{-DMF}$ complex¹²⁰ and the XRD pattern of $\text{PbI}_2\text{-DMF}$ complex crystal was also reported.⁹⁷ Since the XRD pattern of film dried from DMF is different from the reported XRD pattern of $\text{PbI}_2\text{-DMF}$ complex crystal, the colorless crystals formed from DMF solution should not be the crystals of $\text{PbI}_2\text{-DMF}$ complex. Fourier transform infrared spectra (Figure 3.15) provide another evidence of complex formation of $\text{CH}_3\text{NH}_3\text{I-PbI}_2\text{-solvent}$: Vibration peaks of C=O of DMF and S=O of DMSO in spectra of $\text{PbI}_2\text{-solvent}$ complexes are shifted to shorter wavenumber as compared with the corresponding peaks of pure DMF and DMSO due to interaction between PbI_2 and solvent molecule, and the vibration peaks in spectra of $\text{CH}_3\text{NH}_3\text{I-PbI}_2\text{-solvent}$ complexes are further shifted because both $\text{CH}_3\text{NH}_3\text{I}$ and PbI_2 interact with solvent molecule.³³ Hence it is reasonable to assume that the colorless crystals are the crystals of $\text{CH}_3\text{NH}_3\text{I-PbI}_2\text{-DMF}$ complex. When the crystals of $\text{CH}_3\text{NH}_3\text{I-PbI}_2\text{-solvent}$ complexes are heated at 110°C , the (110) peak of $\text{CH}_3\text{NH}_3\text{PbI}_3$ at 14.2° grows while the diffraction peaks of complex crystals between $5\text{--}10^\circ$ disappear accompanying by the color change from colorless to dark brown in in-situ

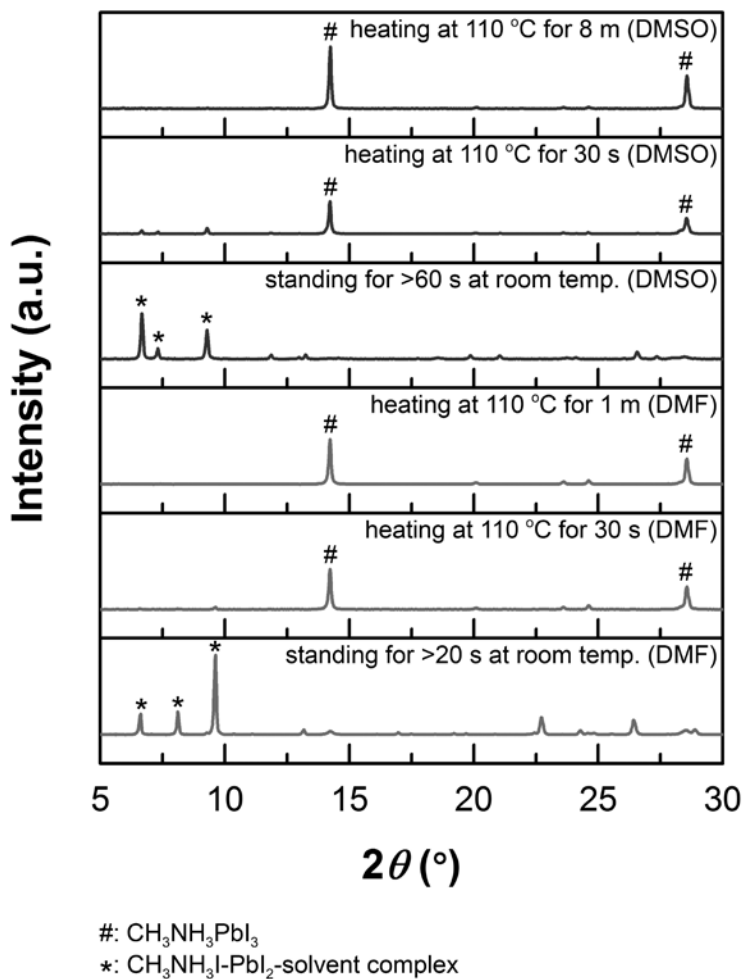


Figure 3.14. XRD patterns of films fabricated from DMF and DMSO solution. Liquid films are solidified by standing the films at room temperature for >20 s (DMF) or >60 s (DMSO). The solidified films are thermally treated at 110 °C until the peaks of $\text{CH}_3\text{NH}_3\text{I-PbI}_2$ -solvent complex disappear.

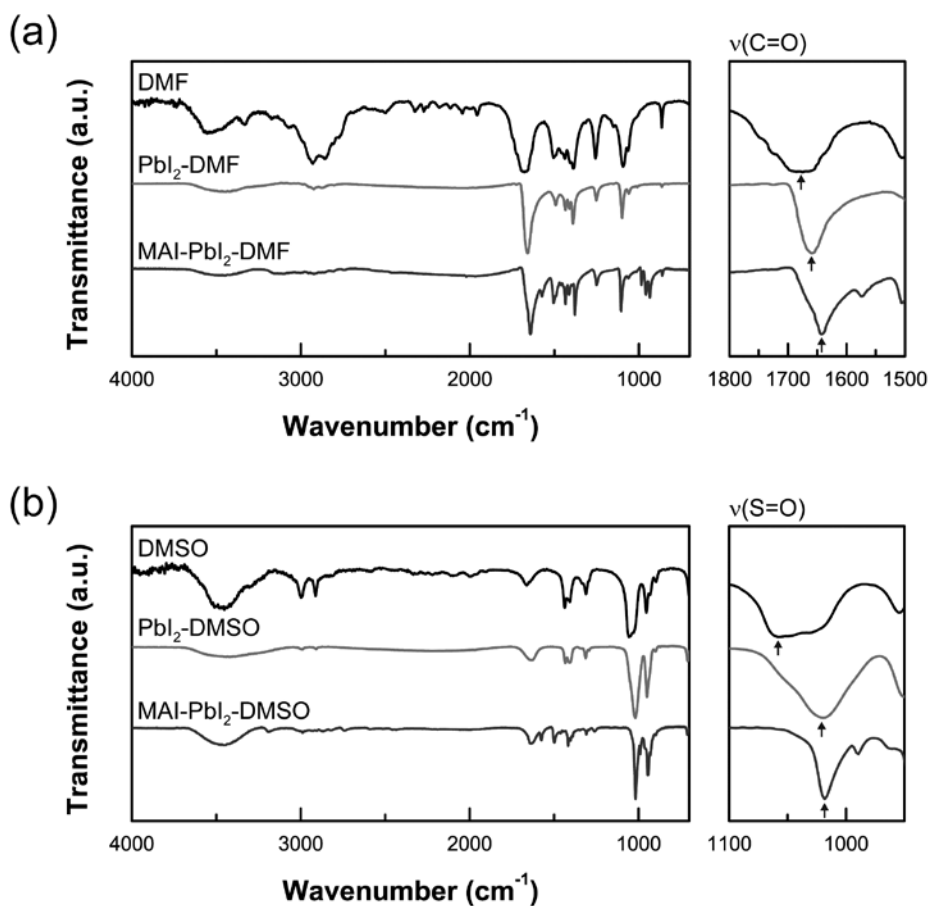


Figure 3.15. FT-IR spectra of (a) DMF (solution), PbI₂-DMF (powder), CH₃NH₃I-PbI₂-DMF (powder) and (b) DMSO (solution), PbI₂-DMSO (powder), CH₃NH₃I-PbI₂-DMSO (powder).

OM images (Figure 3.12). Furthermore, formation of the complex crystals can also be identified in XRD patterns of the films as solidified during spin-coating (compare Figure 3.14 with Figure 3.16), indicating that the crystals of $\text{CH}_3\text{NH}_3\text{I-PbI}_2$ -solvent complexes are formed by solidification during spin-coating. The solidified film during the spin-coating also exhibits the colorless crystal and the color of film is changed to dark brown $\text{CH}_3\text{NH}_3\text{PbI}_3$ after heat treatment (Figure 3.17). This change of color in OM image is well-matched with XRD results. Therefore, it can be concluded that the crystals of $\text{CH}_3\text{NH}_3\text{I-PbI}_2$ -solvent complexes are formed when the solidification occurs during spin-coating or when the liquid films after short spin-coating time are placed at room temperature for long time and that the crystals of the complexes grow in one-dimensional direction, leading to tree-like morphology of $\text{CH}_3\text{NH}_3\text{PbI}_3$ crystals.

The color change of $\text{CH}_3\text{NH}_3\text{I-PbI}_2$ -solvent complex crystal during heat treatment at 110 °C is due to evaporation of solvent molecules which participated in the complex formation. However, when the liquid films after short spin-coating time are heat-treated at 110 °C, $\text{CH}_3\text{NH}_3\text{PbI}_3$ crystals (flower-like morphology) are directly formed without formation of complex crystals, because solvent molecules are evaporated before the complex crystals are formed. When the liquid film is annealed at different temperatures, tree-like morphology is developed at 60 °C annealing, and flower-like morphology is developed at 100 °C (Figure 3.18). Mixed morphology of tree-like and flower-like morphologies is developed at 80 °C probably due to the competition between formation of $\text{CH}_3\text{NH}_3\text{I-PbI}_2$ -solvent complex crystal

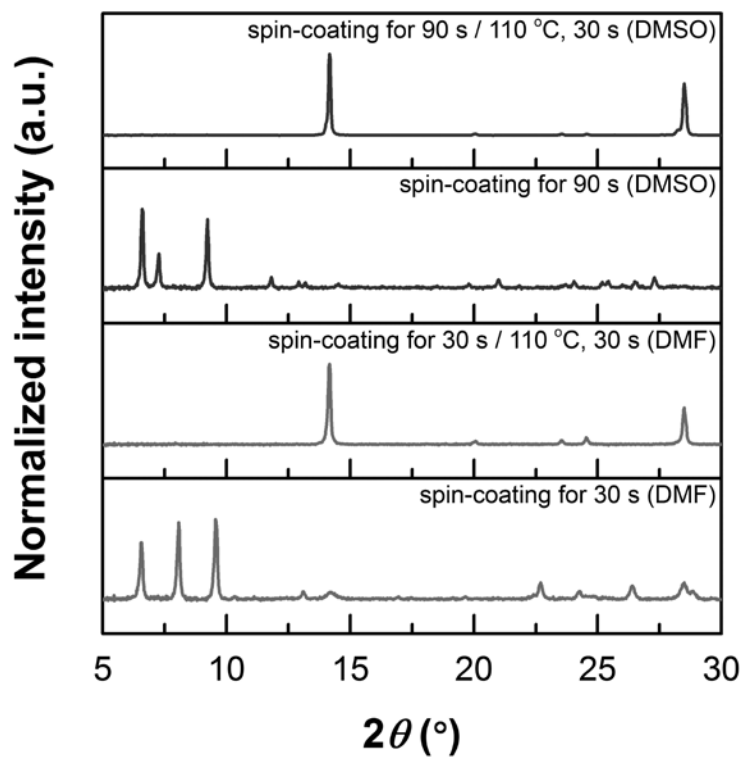


Figure 3.16. XRD patterns of films fabricated from DMF and DMSO solution. The solidified films are prepared by spin-coating at 3000 rpm for 30 s (DMF) or 90 s (DMSO). When the solid films after spin-coating are thermally treated at 110 °C for 30 s, all peaks corresponding to $\text{CH}_3\text{NH}_3\text{I}-\text{PbI}_2$ -solvent complex crystal completely disappear.

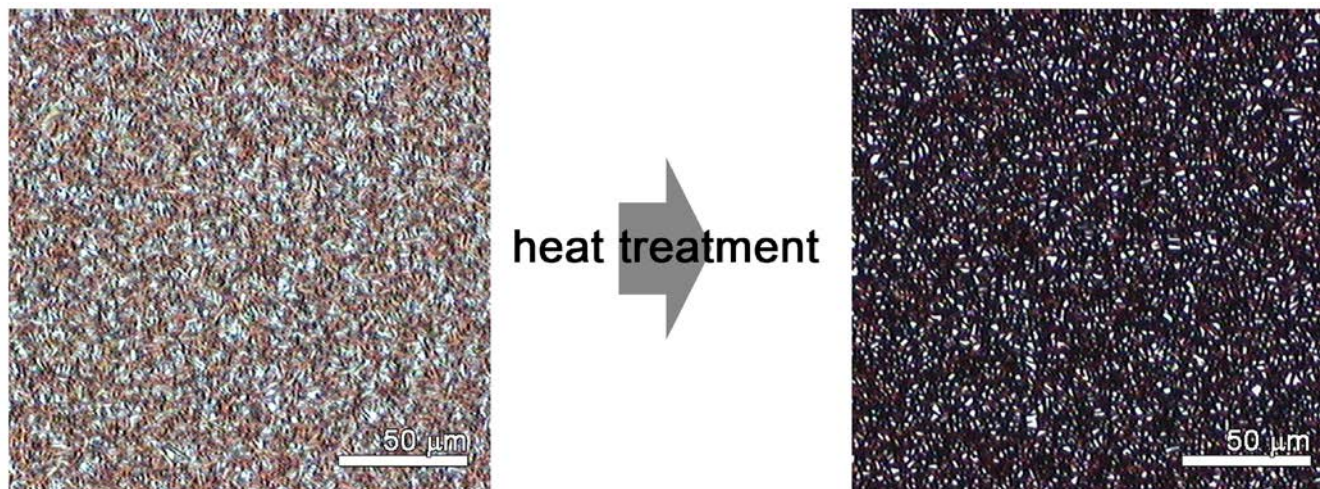


Figure 3.17. OM images of solidified film during the spin-coating and the film after heat treatment. The solidified films are fabricated from DMF solution and prepared by spin-coating at 3000 rpm for 30 s. The solidified film after spin-coating are thermally treated at 110 °C for 30 s.

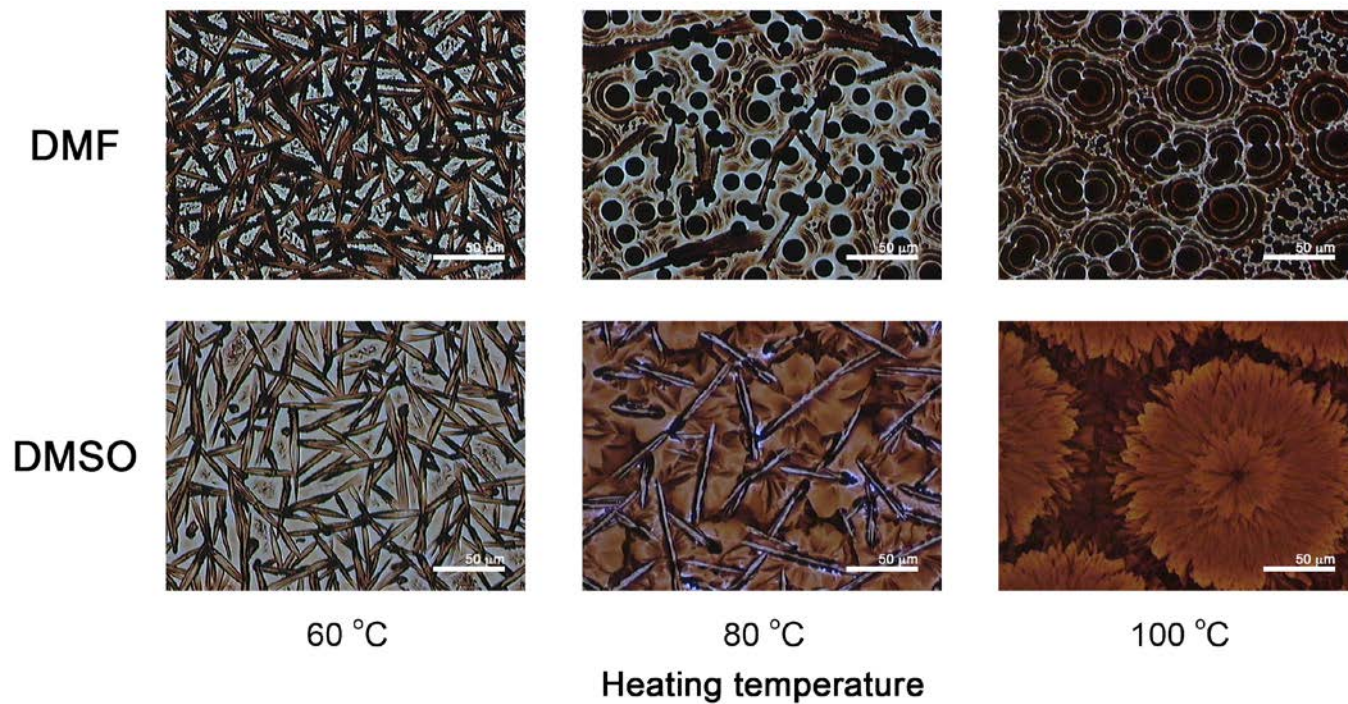


Figure 3.18. OM images of $\text{CH}_3\text{NH}_3\text{PbI}_3$ films prepared from DMF and DMSO solution. The films are prepared by heating the liquid films, which are prepared by spin-coating at 3000 rpm for 3 s (DMF) or for 30 s (DMSO), at 60, 80 and 100 °C.

and solvent evaporation without formation of complex crystal.

3.1.4 $\text{CH}_3\text{NH}_3\text{PbI}_3$ crystal orientation

The above observation tells us that the crystal formation of $\text{CH}_3\text{NH}_3\text{I}-\text{PbI}_2$ -solvent complex is closely related to the film morphology and the

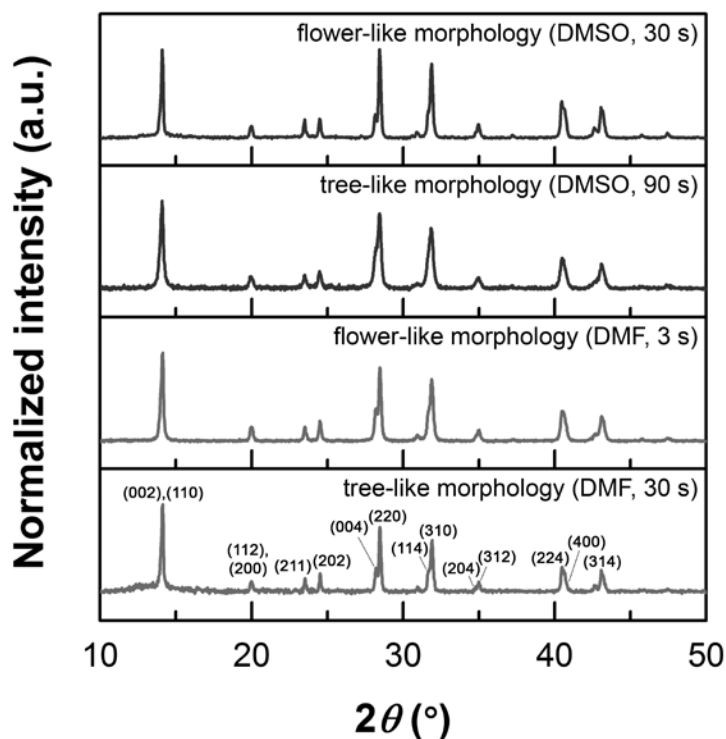


Figure 3.19. Powder XRD patterns of $\text{CH}_3\text{NH}_3\text{PbI}_3$ films with flower-like and tree-like morphology fabricated from DMF and DMSO solution. All films are thermally treated at 110 °C for 30 s after spin-coating. Films with flower-like and tree-like morphologies are ground for powder samples.

orientation of $\text{CH}_3\text{NH}_3\text{PbI}_3$ crystallites. Considering the fact that the same crystal structure, corresponding to the tetragonal structure of $\text{CH}_3\text{NH}_3\text{PbI}_3$ perovskite, is observed in the powder XRD patterns of all films (Figure 3.19), the difference between thin-film XRD patterns (Figure 3.20) indicates that $\text{CH}_3\text{NH}_3\text{PbI}_3$ crystallites have different orientation depending on the film morphology. The XRD patterns of films with tree-like morphology show

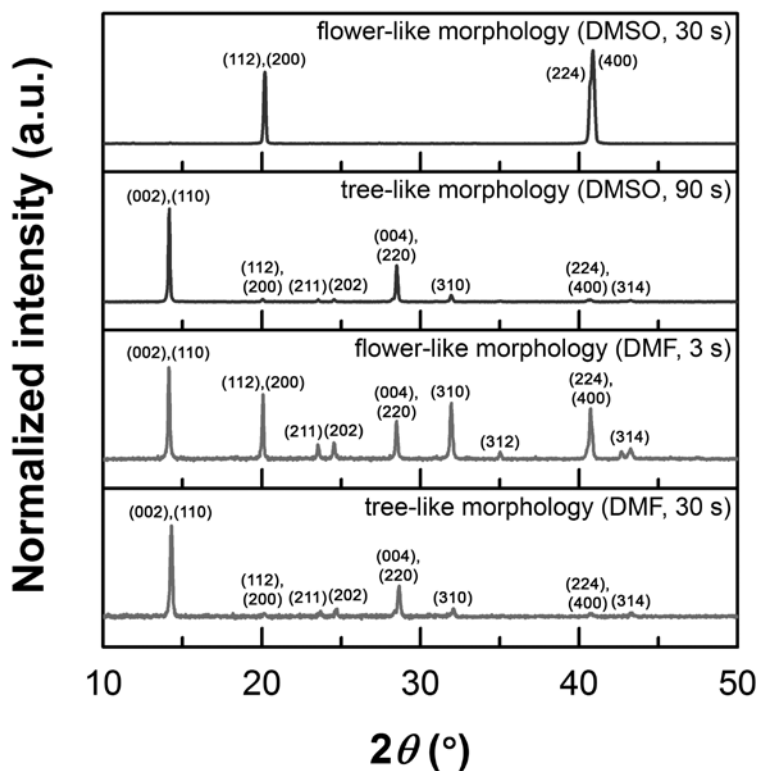


Figure 3.20. XRD patterns of $\text{CH}_3\text{NH}_3\text{PbI}_3$ films with flower-like and tree-like morphology as prepared from DMF and DMSO solution. All films are thermally treated at $110\text{ }^\circ\text{C}$ for 30 s immediately after spin-coating.

strong (002) and (110) peaks dominantly while the patterns of films with flower-like morphology exhibit strong (112) and (200) peaks. The crystal orientation in $\text{CH}_3\text{NH}_3\text{PbI}_3$ films can clearly be identified by 2D grazing incidence X-ray diffraction (GIXD) and its azimuthal angle (χ) scans (Figure 3.21). Peaks of GIXD pattern are assigned in Figure 3.22. The $\text{CH}_3\text{NH}_3\text{PbI}_3$ crystallites in the films with tree-like morphologies, as prepared from DMF and DMSO solutions, do not show preferential orientation (Figure 3.21a and 3.21b) while the crystallites in the films with flower-like morphology are preferentially oriented along (112) or (200) directions to the substrate (Figure 3.21c and 3.21d). Especially, the film from DMSO solution exhibits spot-like reflections with strong intensity, indicating that the $\text{CH}_3\text{NH}_3\text{PbI}_3$ crystallites are highly oriented. Since the edges of PbI_6 octahedron in $\text{CH}_3\text{NH}_3\text{PbI}_3$ crystal contact with the substrate (see Figure 3.23), indicating that $\text{CH}_3\text{NH}_3\text{PbI}_3$ crystallites are oriented along (112) or (200) directions, the crystals with flower-like morphology are oriented in such a way that edges of PbI_6 octahedron contact with the substrate. This result leads us to conclude that the orientation of $\text{CH}_3\text{NH}_3\text{PbI}_3$ crystals is strongly dependent on the film morphology, which can be easily controlled by varying the spin-coating condition. Considering that preferential orientation of perovskite crystals affords high PCEs, the crystal orientation must be one of important factors determining the solar cell performance, although the effect of crystal orientation on photovoltaic properties of $\text{CH}_3\text{NH}_3\text{PbI}_3$ perovskite has not been

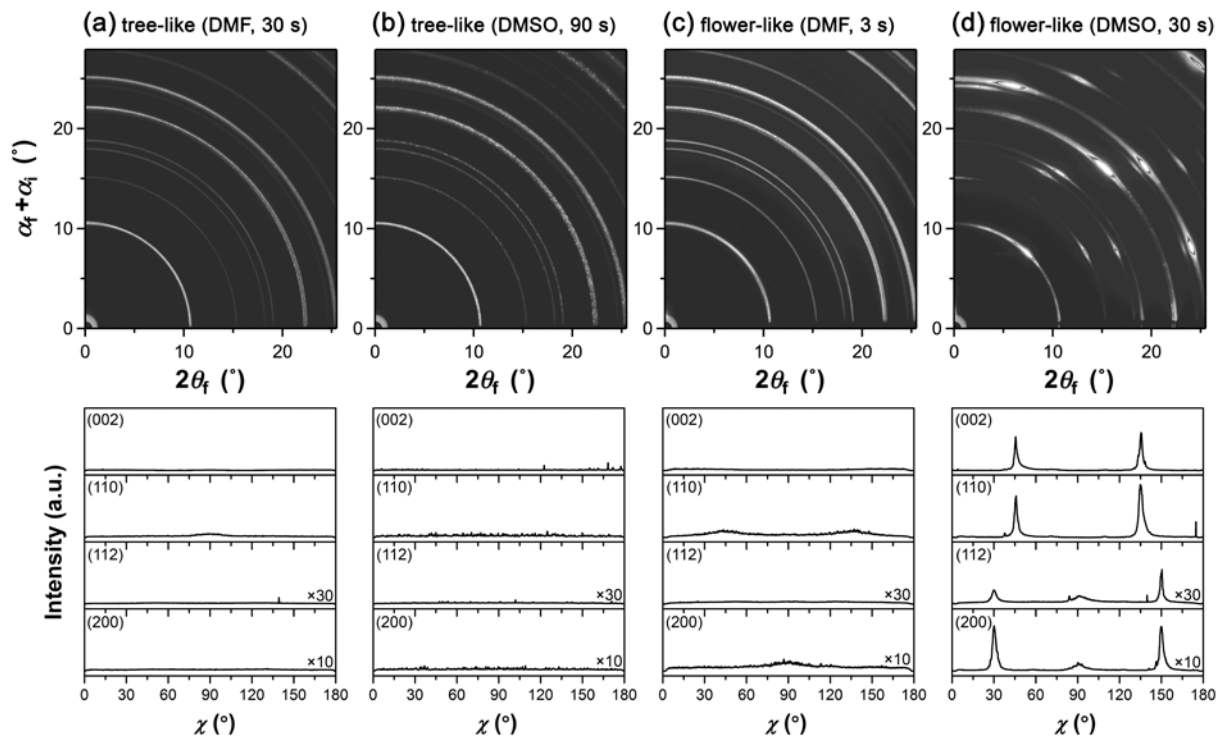


Figure 3.21. 2D GIXD patterns of $\text{CH}_3\text{NH}_3\text{PbI}_3$ films with (a, b) tree-like and (c, d) flower-like morphologies fabricated from (a, c) DMF and (b, d) DMSO solution. All films are thermally treated at 110 °C for 30 s after spin-coating.

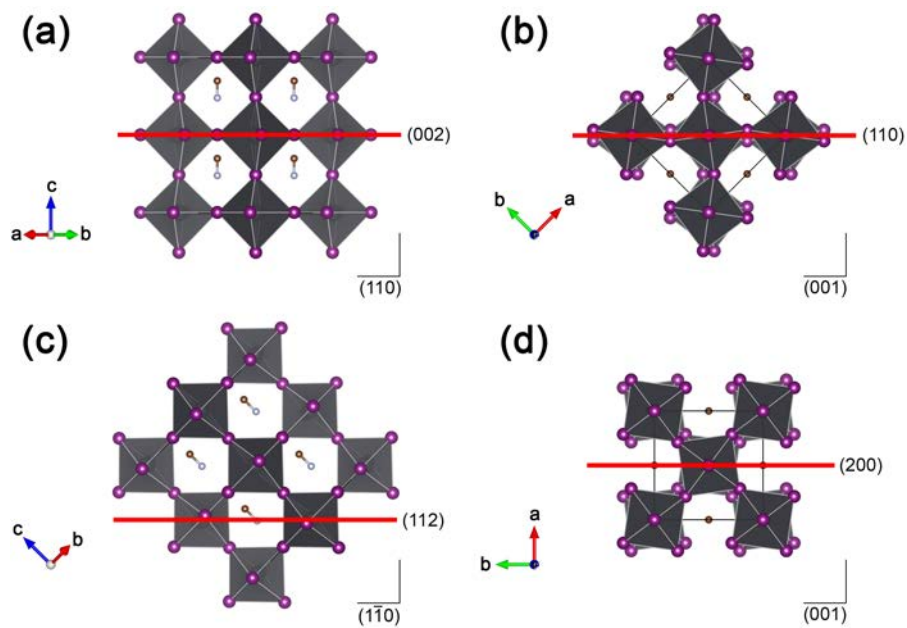


Figure 3.23. Unit cell of tetragonal $\text{CH}_3\text{NH}_3\text{PbI}_3$ crystal. The C, N, I and Pb atoms are represented as brown, light blue, purple and black spheres, respectively, and black octahedra represent PbI_6 units. Solid lines indicate (a) (002), (b) (110), (c) (112) and (d) (200) planes.

fully understood and therefore further studies should be needed to reveal the orientation effect.

3.1.5 Summary

Photovoltaic properties are measured according to spin-coating time and long spin-coating time deteriorates solar cell performance significantly. Comparing color change of films during spin-coating to significant drop of power conversion efficiency, solidification during spin-coating is expected to affect film morphology. Two different morphologies, tree-like and flower-like morphologies, are observed depending on the spin-coating time in OM and SEM images. Solidification during the spin-coating results tree-like morphology and liquid film which is the state before solidification results flower-like morphology. In-situ OM and XRD studies reveal that the solidification during spin-coating is accompanied by formation of $\text{CH}_3\text{NH}_3\text{I}-\text{PbI}_2$ -solvent complex crystals, which induces the crystal growth in one-dimensional direction. The crystal growth in one-dimensional direction yields tree-like morphology with many pinholes in $\text{CH}_3\text{NH}_3\text{PbI}_3$ perovskite film, resulting in very low PCEs of solar cell devices. However, when the solidification during spin-coating is suppressed by shortening the spin-coating time and thereafter $\text{CH}_3\text{NH}_3\text{PbI}_3$ is crystallized directly from the liquid film after spin-coating by post heat-treatment, flower-like morphology is developed in the film with high surface coverage and large crystal size. Also, when the liquid film is annealed at different temperatures, tree-like and

flower-like morphologies are developed at 60 °C and 100 °C, respectively, and mixed morphology of tree-like and flower-like morphologies is developed at 80 °C. Therefore, to achieve a direct crystallization without formation of $\text{CH}_3\text{NH}_3\text{I-PbI}_2$ -solvent complex crystal, sufficient annealing temperature are essential because of the competition between formation of $\text{CH}_3\text{NH}_3\text{I-PbI}_2$ -solvent complex crystal and solvent evaporation without formation of complex crystal. When the $\text{CH}_3\text{NH}_3\text{PbI}_3$ film is fabricated by the direct crystallization, it exhibits crystal orientation along (112) and (200). Specifically, the film from DMSO solution showing flower-like morphology with large-sized crystallites on the length scale of tens of micrometers is composed of crystallites which are highly orientated along (112) and (200), resulting in a high PCE of 13.85%, in contrast, the film with tree-like morphology has small-sized crystallites with random crystal orientation, exhibiting very low PCEs.

3.2 CH₃NH₃PbI₃ crystal orientation and photovoltaic performance of planar heterojunction perovskite solar cells

3.2.1 Synthesis and characterization

Although, in section 3.1, we fabricated the (112) and (200)-oriented CH₃NH₃PbI₃ film controlling the spin-coating time using DMSO solution, highly oriented film with other orientation are required to identify the orientation effect on photovoltaic performance. One of the well-known method is replace the organic precursor from CH₃NH₃I to CH₃NH₃Cl because presence of Cl precursors assists the growth of (110)-oriented CH₃NH₃PbI₃ film.^{65,135,136} Therefore, we synthesized CH₃NH₃Cl through the method that was explained in experimental section and confirmed by ¹H NMR (Figure 3.24.). Protons of methyl and ammonium group are detected at 2.32 ppm and 7.98 ppm, respectively.

3.2.2 CH₃NH₃PbI₃ crystal orientation

Anisotropy of physical properties of inorganic perovskites has intensively been studied.^{121–128} Although CH₃NH₃PbI₃, one of perovskites, has recently received great interest as a promising active layer material in photovoltaics, anisotropic properties of CH₃NH₃PbI₃ have rarely been reported except a few of theoretical studies,^{117,129,130} probably because of lack of techniques to fabricate CH₃NH₃PbI₃ films with well-controlled crystal

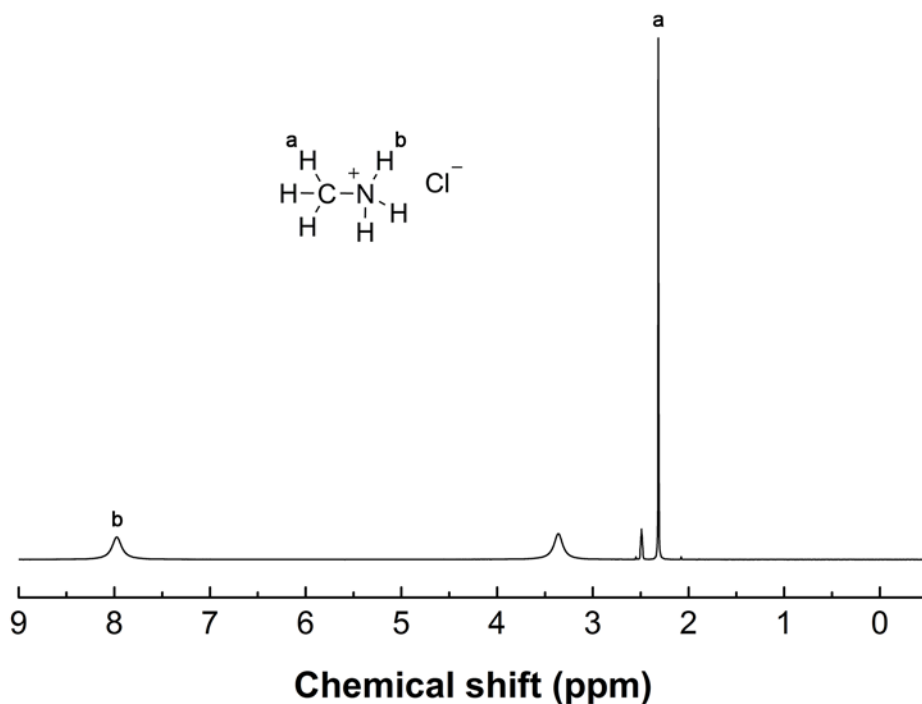


Figure 3.24. ^1H NMR spectrum of methylammonium chloride.

orientation except for orientation of (110) plane. In section 3.1, we have developed a new method to fabricate high quality $\text{CH}_3\text{NH}_3\text{PbI}_3$ film by controlling the type of solvent, spin-coating time and annealing time/temperature. Especially, when $\text{CH}_3\text{NH}_3\text{PbI}_3$ films are fabricated using DMSO as a processing solvent, the crystals in the film exhibit preferred orientation along (112)/(200) direction. Since it has been reported that the presence of Cl precursors ($\text{CH}_3\text{NH}_3\text{Cl}$ or PbCl_2) assists the growth of (110)-oriented $\text{CH}_3\text{NH}_3\text{PbI}_3$ crystals,^{65,135,136} we fabricated perovskite films with

different crystal orientations using two different DMSO solutions containing two organic precursors ($\text{CH}_3\text{NH}_3\text{I}$ and $\text{CH}_3\text{NH}_3\text{Cl}$).

X-ray diffraction (XRD) pattern of $\text{CH}_3\text{NH}_3\text{PbI}_3$ film fabricated from $\text{CH}_3\text{NH}_3\text{I}$ and PbI_2 (hereafter denoted as I_3 film) shows only strong (112) and (200) peaks, while the XRD pattern of $\text{CH}_3\text{NH}_3\text{PbI}_3$ film fabricated from $\text{CH}_3\text{NH}_3\text{Cl}$ and PbI_2 (hereafter denoted as I_2Cl film) shows strong (002) and (110) peaks with additionally weak peak at 15.6° corresponding to (100) reflection of $\text{CH}_3\text{NH}_3\text{PbCl}_3$ crystal, indicating that two films have different crystal orientations (Figure 3.25a). Since it has been known that $\text{CH}_3\text{NH}_3\text{PbI}_3$ (I_2Cl film) contains a small amount of $\text{CH}_3\text{NH}_3\text{PbCl}_3$ crystal after the film is prepared from Cl precursors, we treated several times $\text{CH}_3\text{NH}_3\text{I}$ on the I_2Cl film to remove the residual $\text{CH}_3\text{NH}_3\text{PbCl}_3$ crystal. As the I_2Cl film is treated two times by $\text{CH}_3\text{NH}_3\text{I}$, the peak intensity of $\text{CH}_3\text{NH}_3\text{PbCl}_3$ crystal is largely decreased while the peak intensities of $\text{CH}_3\text{NH}_3\text{PbI}_3$ crystals remain nearly unchanged (Figure 3.25b).

The orientation of $\text{CH}_3\text{NH}_3\text{PbI}_3$ perovskite crystals within the I_3 and I_2Cl films are characterized by 2D grazing-incidence X-ray diffraction (2D GIXD). Since 2D GIXD patterns of I_3 and I_2Cl films show spot-like reflections with strong intensity, as shown in Figure 3.26a and 3.26b, the $\text{CH}_3\text{NH}_3\text{PbI}_3$ crystals are highly oriented (Peaks in 2D diffraction patterns are assigned in Figure 3.27). The azimuthal angle (χ) scan is a powerful method to assess the crystal orientation. Considering that the peak at $\chi=90^\circ$ indicates preferential orientation of the corresponding crystal plane parallel to the substrate, we realize that the $\text{CH}_3\text{NH}_3\text{PbI}_3$ crystals in I_3 film are oriented such (112) and

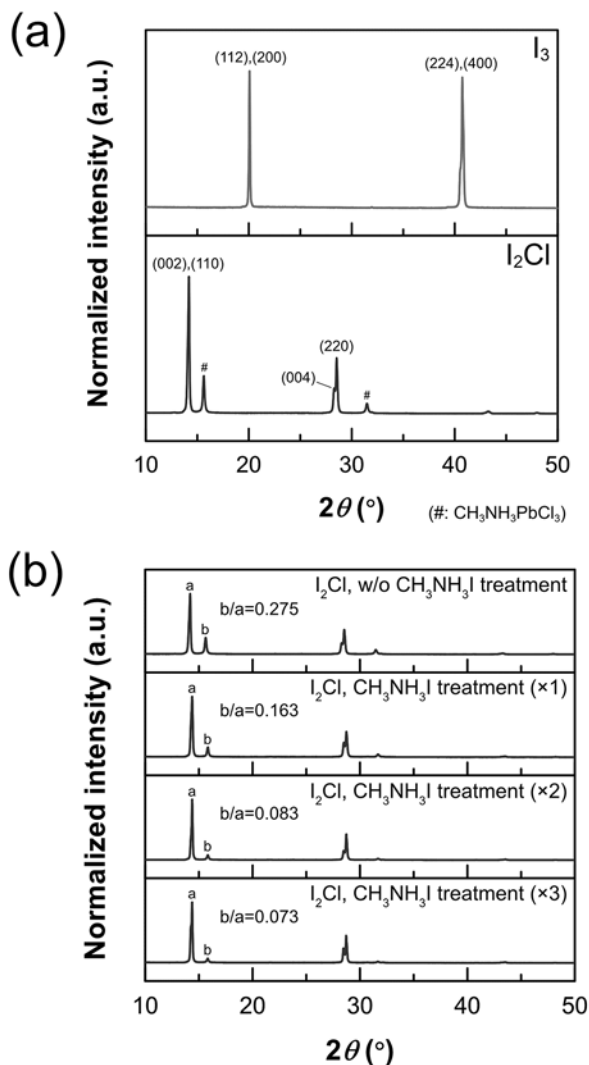


Figure 3.25. XRD patterns of films fabricated from (a) two different organic precursors ($\text{CH}_3\text{NH}_3\text{I}$ and $\text{CH}_3\text{NH}_3\text{Cl}$) and (b) the change of XRD patterns of I_2Cl films according to $\text{CH}_3\text{NH}_3\text{I}$ treatment. $\text{CH}_3\text{NH}_3\text{I}$ is treated on I_2Cl film several times to minimize the residual amount of $\text{CH}_3\text{NH}_3\text{PbCl}_3$ in $\text{CH}_3\text{NH}_3\text{PbI}_3$ crystal.

(200) planes that are parallel to the substrate while those in I_2Cl film are oriented along (002) and (110) directions, because the χ scans of (112) and (200) reflections of I_3 film show peaks at 90° while the χ scans of (002) and (110) reflections of I_2Cl film reveal the peaks at 90° . Ball-and-stick representations of $CH_3NH_3PbI_3$ crystals oriented along (002), (110), (112) and

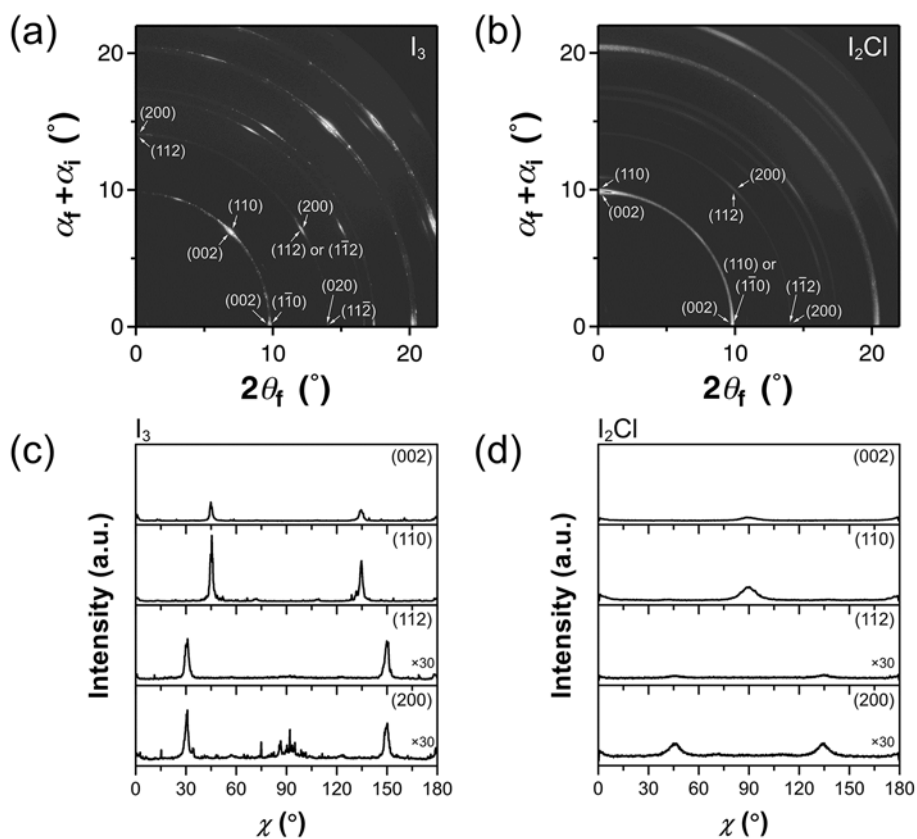


Figure 3.26. GIXD patterns of (a) I_3 and (b) I_2Cl film and (c, d) azimuthal angle (χ) scans.

(200) directions with respect to the substrate are shown in Figure 3.28. According to the previous report,¹³⁰ the (110) and (002) planes of

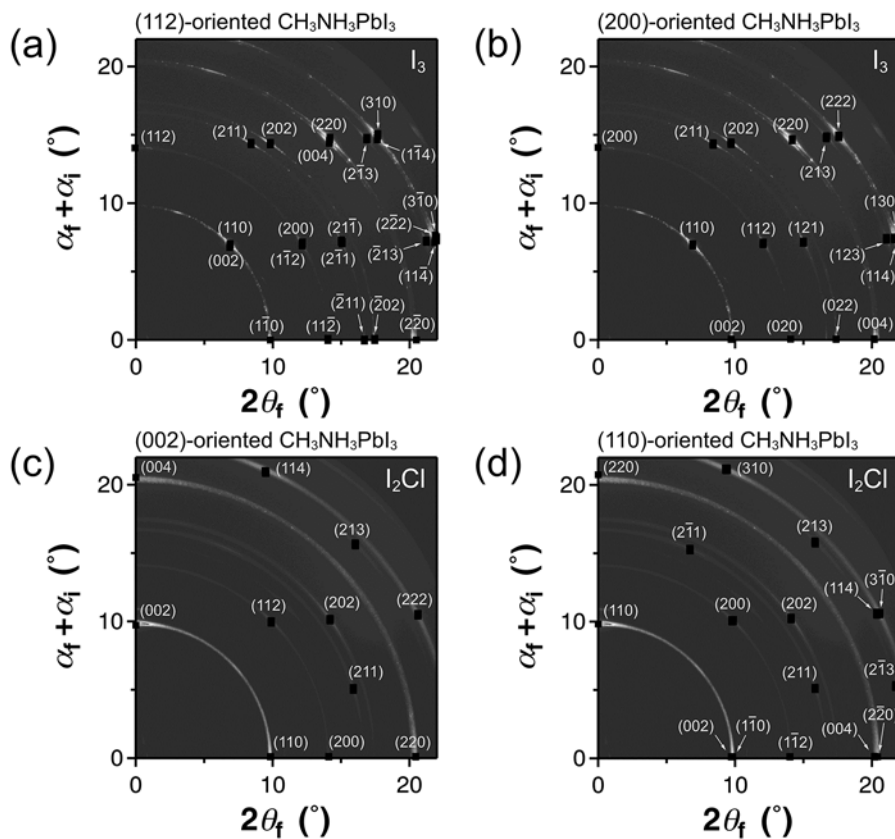


Figure 3.27. Assignment of diffraction peaks. 2D diffraction pattern of I_3 film is assigned by calculated pattern of $\text{CH}_3\text{NH}_3\text{PbI}_3$ crystals oriented such (a) (112) and (b) (200) planes that are parallel to the substrate. 2D diffraction pattern of $I_2\text{Cl}$ film is assigned by calculated pattern of $\text{CH}_3\text{NH}_3\text{PbI}_3$ crystals oriented such (a) (002) and (b) (112) planes that are parallel to the substrate.

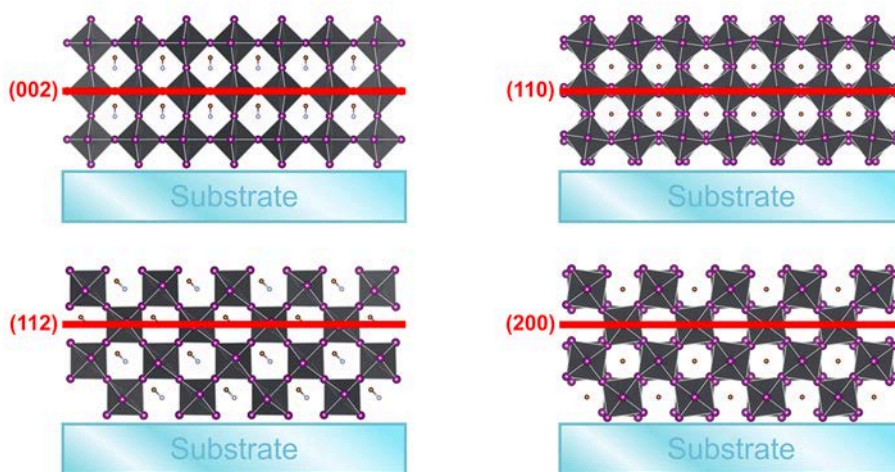


Figure 3.28. Ball-and-stick representation of $\text{CH}_3\text{NH}_3\text{PbI}_3$ crystal in which (002), (110), (112) and (200) planes are parallel to the substrate. The C, N, I and Pb atoms are represented by brown, blue, purple and black spheres, respectively, and dark grey octahedron represent PbI_6 unit.

$\text{CH}_3\text{NH}_3\text{PbI}_3$ crystal are nonpolar surfaces which are constructed with alternative stacking of neutral $[\text{CH}_3\text{NH}_3\text{I}]^0$ and $[\text{PbI}_2]^0$ planes, while the (200) and (112) planes are polar surfaces which consist of stacking of $[\text{CH}_3\text{NH}_3\text{PbI}]^{2+}$ and $[\text{I}_2]^{2-}$ planes.

3.2.3 Film morphology

Morphologies of I_3 and I_2Cl films as observed by scanning electron microscopy (SEM) reveal that the morphologies of I_3 and I_2Cl films are

similar and additional $\text{CH}_3\text{NH}_3\text{I}$ treatment does not affect significantly the film morphology (Figure 3.29), indicating that the film morphology may not be related to photovoltaic performance.

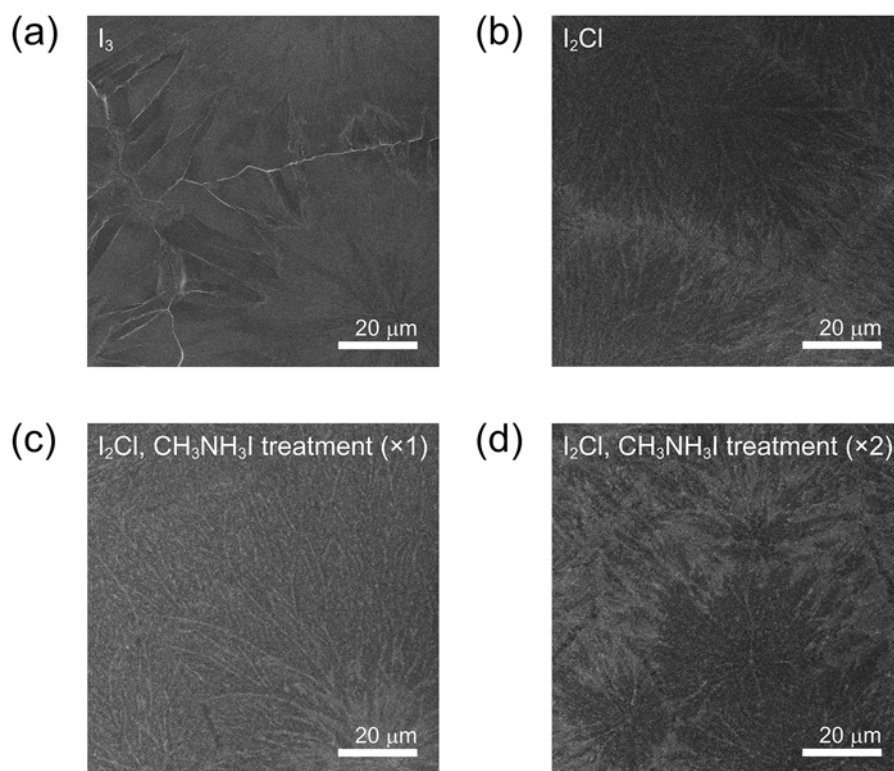


Figure 3.29. SEM images of films fabricated from different organic precursors: (a) I_3 film, (b) I_2Cl , and I_2Cl films after $\text{CH}_3\text{NH}_3\text{I}$ is treated (c) one and (d) two times.

3.2.4 Photovoltaic properties

To identify the effect of preferred orientation of $\text{CH}_3\text{NH}_3\text{PbI}_3$ crystals on photovoltaic performance, two types of planar heterojunction solar cells (inverted and normal cells) are fabricated with I_3 and I_2Cl films. Normal cell has the device configuration of $\text{ITO}/\text{TiO}_2/\text{CH}_3\text{NH}_3\text{PbI}_3/\text{spiro-OMeTAD}/\text{Au}$ and inverted cell has the device configuration of $\text{ITO}/\text{PEDOT:PSS}/\text{CH}_3\text{NH}_3\text{PbI}_3/\text{PCBM}/\text{TiO}_2/\text{Al}$. J - V curves of solar cells are shown in Figure 3.30 and photovoltaic parameters are listed in Table 3.2. External quantum efficiency spectra are shown in Figure 3.31. The efficiency of inverted cell made of I_3 film is higher than that of the inverted cell prepared with I_2Cl film mainly due to higher short circuit current (J_{SC}) and higher fill factor (FF) of I_3 -based cell, whereas the efficiency of normal cell prepared with I_2Cl film is higher than that of the inverted cell made of I_3 film. Considering that the crystals in I_3 and I_2Cl films exhibit different orientation to the substrate, we assume that the orientation of $\text{CH}_3\text{NH}_3\text{PbI}_3$ crystal in film affects largely the charge transfer between $\text{CH}_3\text{NH}_3\text{PbI}_3$ and CTL.

3.2.5 Charge transfer characteristics

The charge transfer between $\text{CH}_3\text{NH}_3\text{PbI}_3$ film and CTL is evaluated by measuring the photoluminescence (PL) lifetime: Shorter PL lifetime indicates faster charge transfer between $\text{CH}_3\text{NH}_3\text{PbI}_3$ film and CTL. PL decays, as shown in Figure 3.32, were fitted with bi-exponential decay curves to yield

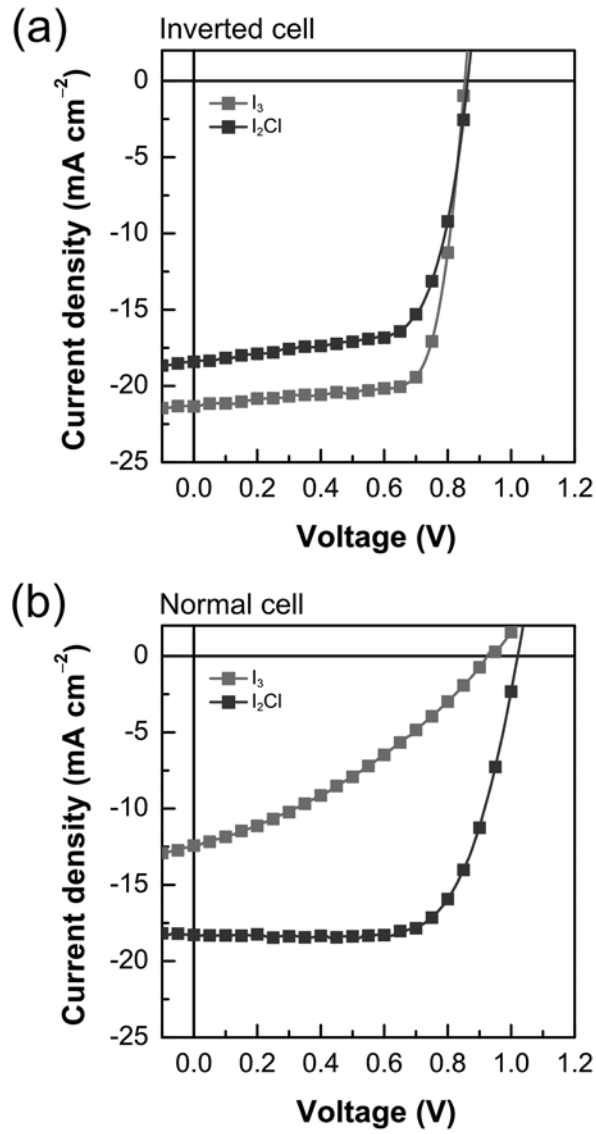


Figure 3.30. J - V curves of (a) inverted cells and (b) normal cells.

Table 3.2. Photovoltaic properties of CH₃NH₃PbI₃ solar cells made of different organic precursor and different device structure.

Device structure	Organic precursor	V_{OC} (V)	J_{SC} (mA cm ⁻²)	FF (%)	Best PCE (ave. PCE) (%)	Standard deviation
Inverted ^[a]	CH ₃ NH ₃ I	0.86	21.34	74.1	13.60 (12.85)	0.53
	CH ₃ NH ₃ Cl	0.86	18.54	70.6	11.26 (10.72)	0.45
Normal ^[b]	CH ₃ NH ₃ I	0.92	12.43	34.7	3.97 (3.18)	0.98
	CH ₃ NH ₃ Cl	1.02	18.28	69.1	12.88 (11.36)	0.47

^[a] ITO/PEDOT:PSS/CH₃NH₃PbI₃/PC₆₁BM/TiO₂/Al

^[b] ITO/TiO₂/CH₃NH₃PbI₃/spiro-OMeTAD/Au

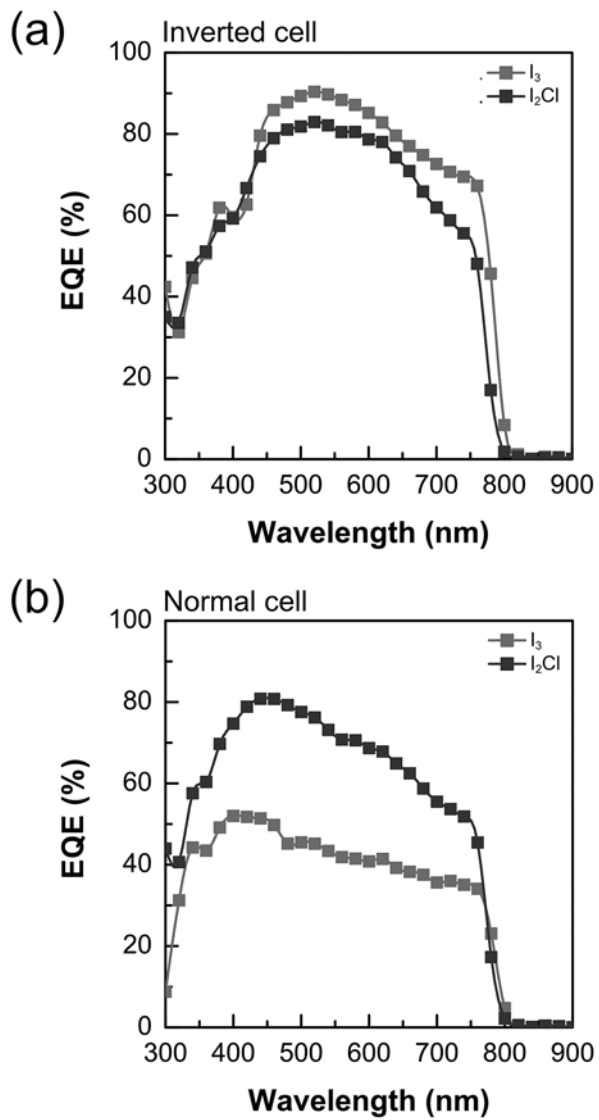


Figure 3.31. EQE spectra of (a) inverted cells and (b) normal cells.

the lifetimes of carriers,^{131,132} and the fitting parameters are listed in Table 3.3. From the relation $1/(\tau_{\text{ave,HJ}}) = 1/(\tau_{\text{ave,Perov}}) + 1/(\tau_{\text{CT}})$, we can estimate the charge carrier transfer time (τ_{CT}) by measuring average lifetimes of pristine $\text{CH}_3\text{NH}_3\text{PbI}_3$ film ($\tau_{\text{ave,Perov}}$) and $\text{CH}_3\text{NH}_3\text{PbI}_3$ film contacting with quencher ($\tau_{\text{ave,HJ}}$).³⁴ When $\text{CH}_3\text{NH}_3\text{PbI}_3$ contacts with charge transport layers (PEDOT:PSS, spiro-OMeTAD, PCBM and TiO_2), the PL lifetimes become shorter than the PL lifetime of pristine $\text{CH}_3\text{NH}_3\text{PbI}_3$, indicating that charges are effectively transferred from $\text{CH}_3\text{NH}_3\text{PbI}_3$ to CTL. For the purpose to examine the effect of crystal orientation of perovskite on the charge transfer, we compare the charge transfer time of I_3 to quencher with that of I_2Cl to quencher. Note here that the crystals in I_3 are oriented such that (112) and (200) planes are parallel to the substrate while the crystals in I_2Cl are oriented along (002) and (110) directions. Comparison of average lifetimes reveals that hole and electron are more easily transferred from I_3 to PEDOT:PSS and PCBM than from I_2Cl to PEDOT:PSS and PCBM, respectively, indicating that (112) and (200) planes contacting with the substrate are more favorable for charger transfer than (102) and (110) planes. On the other hand, the charge carriers are more easily transferred from I_2Cl to spiro-OMeTAD and TiO_2 than from I_3 to spiro-OMeTAD and TiO_2 , respectively, indicating that (002) and (110) planes contacting the substrate are more favorable for the charge transfer. Since perovskite layer contacts with PEDOT:PSS and PCBM in inverted cell, we may expect that I_3 -based inverted solar cell exhibits higher efficiency than I_2Cl -based inverted cell. On the other hand, the perovskite layer contacts with spiro-OMeTAD and

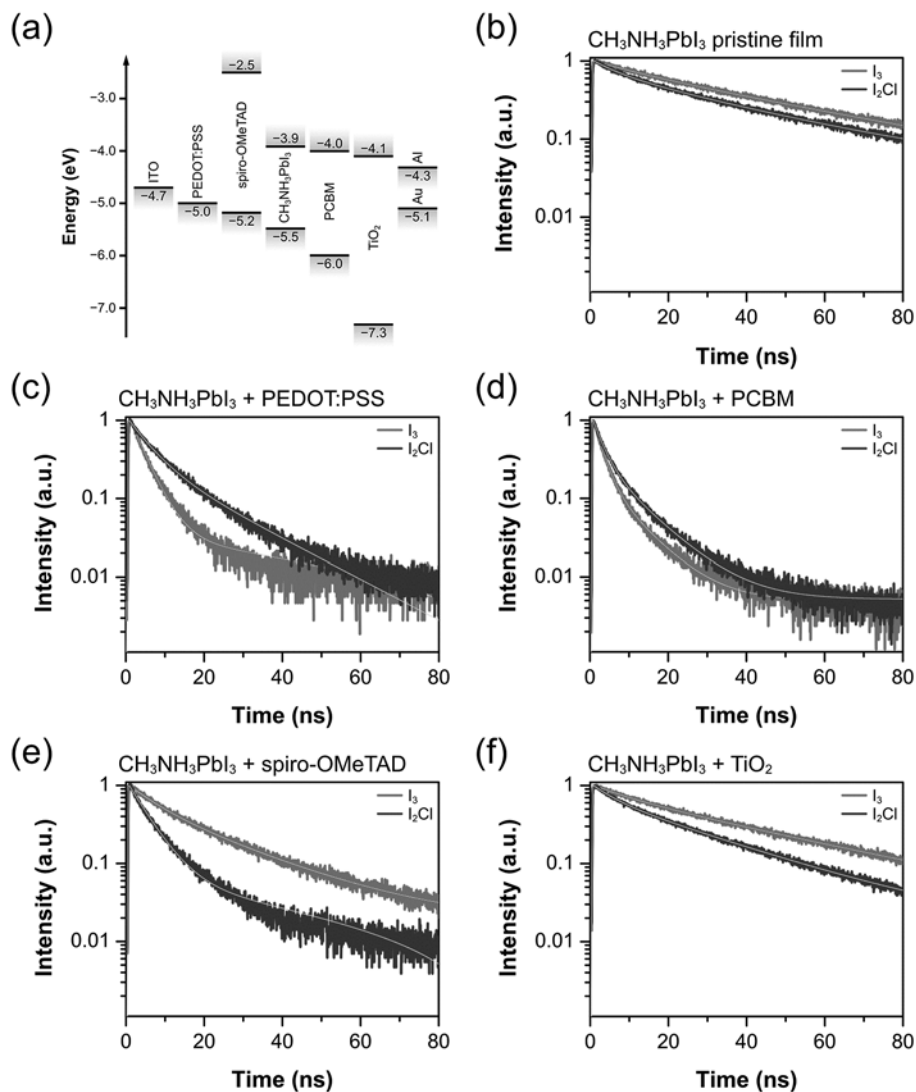


Figure 3.32. (a) energy levels of materials used for solar cells; transient photoluminescence spectra: (b) pristine CH₃NH₃PbI₃ film, (c) CH₃NH₃PbI₃/PEDOT:PSS, (d) CH₃NH₃PbI₃/PCBM, (e) CH₃NH₃PbI₃/spiro-OMeTAD and (f) CH₃NH₃PbI₃/TiO₂. All samples for PL are prepared on quartz glass.

Table 3.3. Fitting parameters of PL decays of CH₃NH₃PbI₃ and CH₃NH₃PbI₃/CTL.

CTL	Film	Crystal plane ^[a]	A ₁	τ ₁ (ns)	A ₂	τ ₂ (ns)	τ _{ave,HJ} (ns) ^[b]	τ _{CT} (ns) ^[c]	Charge transfer efficiency (%)
None	I ₃	(112)/(200)	0.78	46.0	0.22	12.6	38.7 ^[d]	-	-
	I ₂ Cl	(002)/(110)	0.70	34.2	0.30	6.7	25.9 ^[d]	-	-
PEDOT:PSS	I ₃	(112)/(200)	0.96	3.7	0.04	82.8	7.1	8.6	82
	I ₂ Cl	(002)/(110)	0.69	5.1	0.32	16.7	8.8	13.3	66
PCBM	I ₃	(112)/(200)	0.82	2.1	0.18	8.0	3.2	3.5	92
	I ₂ Cl	(002)/(110)	0.70	2.5	0.30	9.0	4.4	5.3	83
Spiro-OMeTAD	I ₃	(112)/(200)	0.57	21.4	0.43	6.9	15.1	24.9	61
	I ₂ Cl	(002)/(110)	0.92	5.0	0.08	65.6	9.8	15.8	62
TiO ₂	I ₃	(112)/(200)	0.75	40.1	0.25	10.3	32.5	203.8	16
	I ₂ Cl	(002)/(110)	0.68	25.9	0.32	5.6	19.4	78.2	25

^[a] Crystal planes that are parallel to the substrate

^[b] $\tau_{ave} = A_1\tau_1 + A_2\tau_2$ (τ_{ave} : average charge carrier lifetime)

^[c] $1/\tau_{ave,HJ} = 1/\tau_{ave,Perv} + 1/\tau_{CT}$, where $\tau_{ave,Perv}$ and $\tau_{ave,HJ}$ are the average lifetimes of pristine and CH₃NH₃PbI₃ film contacting with CTL, respectively, and τ_{CT} is the charge carrier transfer time.

^[d] Average lifetimes of pristine CH₃NH₃PbI₃ film ($\tau_{ave,Perv}$)

TiO₂ in normal solar cell, and therefore I₂Cl-based normal cell is expected to exhibit higher efficiency than I₃-based normal solar cell. In short, the orientation of CH₃NH₃PbI₃ crystals on the substrate is directly related to the photovoltaic performance of perovskite solar cells through the anisotropy of charge transfer in perovskite crystal.

3.2.6 Photocurrent density–voltage hysteresis

Another feature to note here is that the charge transfer from CH₃NH₃PbI₃ to spiro-OMeTAD or TiO₂ is slow as to compared the charge transfer to PEDOT:PSS and PCBM. Especially, the charge transfer time to TiO₂ ($\tau_{CT}=203.8$ ns) is much longer than other cases and thus the charge transfer efficiency (16%) is the lowest. Since it has been known that photo-induced charges accumulate at the interface and thus cause $J-V$ hysteresis when hole and electron extractions from perovskite layer are delayed and imbalanced,^{114,133} it is not strange to observe strong hysteresis in $J-V$ curves of normal cells due to slow and imbalanced charge transfer to spiro-OMeTAD and TiO₂ whereas the inverted cells do not show hysteresis because of fast and balanced charge transfers from perovskite layer to PEDOT:PSS and PCBM (Figure 3.33). Sanchez *et. al.*¹³⁴ have proposed the hysteric index (HI) as defined by the following equation to quantify the hysteresis effect in the $J-V$ curve:

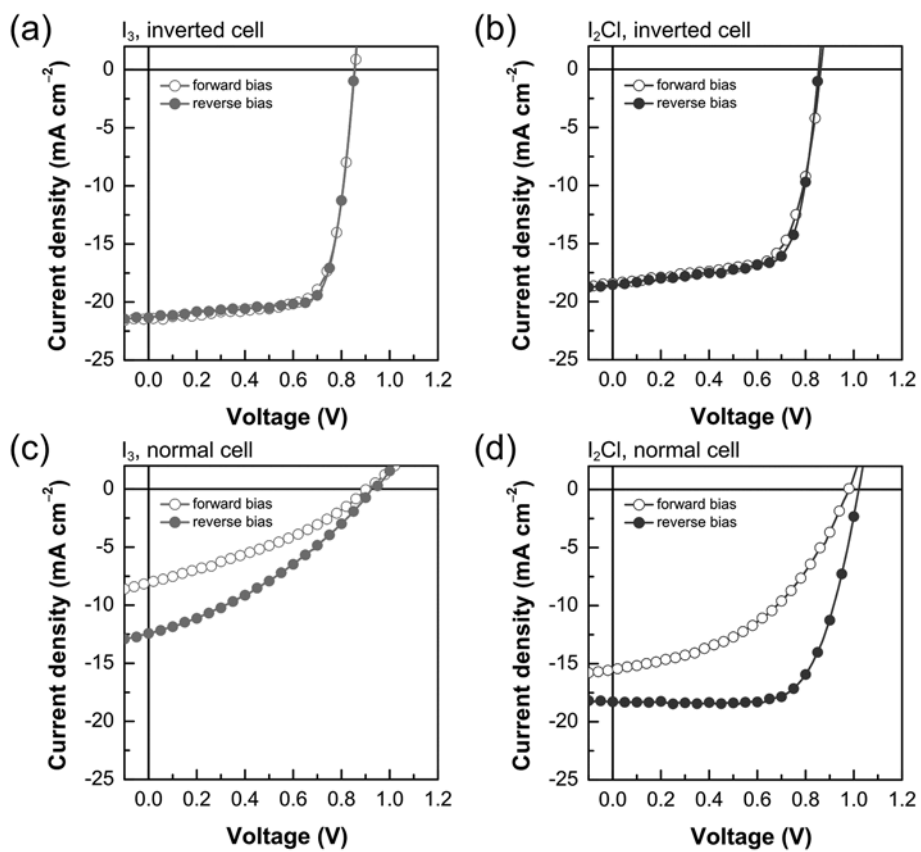


Figure 3.33. J - V hysteresis of (a, b) inverted and (c, d) normal cells. The devices are fabricated from (a, c) I_3 and (b, d) I_2Cl films.

Table 3.4. Photovoltaic properties of CH₃NH₃PbI₃ solar cells depending on device structure, organic precursor and scan direction.

Device structure	Organic precursor	Scan direction	V _{OC} (V)	J _{SC} (mA cm ⁻²)	FF (%)	PCE (%)
Inverted	CH ₃ NH ₃ I	Forward	0.86	21.43	71.9	13.25
		Reverse	0.86	21.34	74.1	13.60
	CH ₃ NH ₃ Cl	Forward	0.86	18.41	68.0	10.77
		Reverse	0.86	18.54	70.6	11.26
Normal	CH ₃ NH ₃ I	Forward	0.90	8.08	33.9	2.47
		Reverse	0.92	12.43	34.7	3.97
	CH ₃ NH ₃ Cl	Forward	0.98	15.48	45.4	6.89
		Reverse	1.02	18.28	69.1	12.88

$$\text{HI} = \frac{J_{\text{SC,rev}}(V_{\text{OC}}/2) - J_{\text{SC,fwd}}(V_{\text{OC}}/2)}{J_{\text{SC,rev}}(V_{\text{OC}}/2)} \quad (3.1)$$

where $J_{\text{SC,rev}}(V_{\text{OC}}/2)$ and $J_{\text{SC,fwd}}(V_{\text{OC}}/2)$ are the photocurrent at $V_{\text{OC}}/2$ bias for reverse scan and forward scan, respectively. A value of HI = 0 represents a device without hysteresis, while the value of 1 represents a device showing hysteresis as high as the photocurrent at $V_{\text{OC}}/2$. The HI values obtained from J - V curves of inverted cells are very small while the values obtained from J - V curves of normal cells are large. Since the HI value is inversely proportional to the charge transfer time and the ratio of hole (electron) to electron (hole) transfer time, our result supports previous reports that J - V hysteresis originates from slow and imbalanced charge transfer with that.^{114,133}

In short, we successfully fabricated perovskite films with different crystal orientations. Since we have found that the orientation of $\text{CH}_3\text{NH}_3\text{PbI}_3$ crystals is directly related to photovoltaic performance of perovskite solar cells, the crystal orientation of perovskite layer must be carefully controlled depending upon the nature of substrate for achieving high efficiency of perovskite solar cells with planar heterojunction structure.

3.2.7 Summary

By using two different organic precursors ($\text{CH}_3\text{NH}_3\text{I}$ and $\text{CH}_3\text{NH}_3\text{Cl}$), $\text{CH}_3\text{NH}_3\text{PbI}_3$ films with two different crystal orientations with respect to the substrate were successfully fabricated: Crystals in I_3 film are oriented such (112) and (200) planes are parallel to the substrate while those in I_2Cl film are

oriented along (002) and (110) directions with respect to the substrate. The efficiency of inverted cell made of I_3 film is higher than that of the cell fabricated from I_2Cl film, while the efficiency of normal cell made of I_2Cl film is higher than that of the device prepared from I_3 film. The efficiency difference arises mainly from orientation difference of $\text{CH}_3\text{NH}_3\text{PbI}_3$ crystals through anisotropy of charge transfer in $\text{CH}_3\text{NH}_3\text{PbI}_3$ crystal. Strong hysteresis are observed in $J-V$ curves of normal cells and interpreted in terms of slow and imbalanced charge transfers from perovskite to CTLs. In short, we have found that the crystal orientation of $\text{CH}_3\text{NH}_3\text{PbI}_3$ is directly related to the photovoltaic performance due to anisotropy of charge transfer in perovskite crystal, suggesting that control of crystal orientation is one of important methods to improve the photovoltaic performance of perovskite solar cells with planar heterojunction structure.

Chapter 4. Conclusions

In this study, we have proposed the optimum processing condition to afford favorable film morphology and crystal orientation for achieving high power conversion efficiency of perovskite solar cells.

First, we have investigated the effect of solidification during spin-coating in one-step deposition on the morphology of $\text{CH}_3\text{NH}_3\text{PbI}_3$ film and its photovoltaic performance. In-situ OM and XRD studies reveal that the solidification during spin-coating is accompanied by formation of $\text{CH}_3\text{NH}_3\text{I}-\text{PbI}_2$ -solvent complex crystals, which induces the crystal growth in one-dimensional direction. The crystal growth in one-dimensional direction yields tree-like morphology with many pinholes in $\text{CH}_3\text{NH}_3\text{PbI}_3$ perovskite film, resulting in very low PCEs of solar cell devices. However, when the solidification during spin-coating is suppressed by shortening the spin-coating time and thereafter $\text{CH}_3\text{NH}_3\text{PbI}_3$ is crystallized directly from the liquid film after spin-coating by post heat-treatment, flower-like morphology is developed in the film with high surface coverage and large crystal size. Specifically, the film from DMSO solution showing flower-like morphology has large-sized crystallites on the length scale of tens of micrometers and the crystallites in the film are highly orientated along (112) and (200) directions, resulting in a high PCE of 13.85%. This observation demonstrates that the solidification accompanied by complex formation during spin-coating should be avoided for high performance perovskite solar cells. Hence, the direct crystallization from liquid film without formation of the complex crystal is a

promising method for achieving high performance perovskite solar cells.

Second, we successfully fabricated $\text{CH}_3\text{NH}_3\text{PbI}_3$ films with two different crystal orientations with respect to the substrate by using two different organic precursors ($\text{CH}_3\text{NH}_3\text{I}$ and $\text{CH}_3\text{NH}_3\text{Cl}$): Crystals in I_3 film are oriented such (112) and (200) planes are parallel to the substrate while those in I_2Cl film are oriented along (002) and (110) directions with respect to the substrate. We have then demonstrated that the crystal orientation of perovskite is closely related to the photovoltaic performance of planar heterojunction solar cells, where the orientation effect on photovoltaic performance becomes different depending upon the type of substrate: The efficiency of inverted cell made of I_3 film is higher than that of the cell fabricated from I_2Cl film, while the efficiency of normal cell made of I_2Cl film is higher than that of the device prepared from I_3 film. The efficiency difference arises mainly from orientation difference of $\text{CH}_3\text{NH}_3\text{PbI}_3$ crystals through anisotropy of charge transfer in $\text{CH}_3\text{NH}_3\text{PbI}_3$ crystal. Due to the slow and imbalanced charge transfer, Strong hysteresis as observed in J - V curves of normal cells are interpreted in terms of slow and imbalanced charge transfers from perovskite to CTLs. In short, we have found that the crystal orientation of $\text{CH}_3\text{NH}_3\text{PbI}_3$ is directly related to the photovoltaic performance due to anisotropy of charge transfer in perovskite crystal, suggesting that control of crystal orientation is one of important methods to improve the photovoltaic performance of perovskite solar cells with planar heterojunction structure.

We have revealed the mechanisms of $\text{CH}_3\text{NH}_3\text{PbI}_3$ film formation and the effect of crystal orientation on photovoltaic properties, and proposed the

optimum processing condition to afford favorable film morphology and crystal orientation for achieving high power conversion efficiency of perovskite solar cells. Further improvement of power conversion efficiency can be achieved by studying of new device architecture because we may be able to have deeper insight on operating mechanisms of new device architecture based on our know-how of morphology control and crystal orientation control.

Bibliography

- (1) Weber, D. *Z. Naturforsch.* **1978**, *33b*, 1443.
- (2) Weber, D. *Z. Naturforsch.* **1978**, *33b*, 862.
- (3) Juarez-Perez, E. J.; Sanchez, R. S.; Badia, L.; Garcia-Belmonte, G.; Kang, Y. S.; Mora-Sero, I.; Bisquert, J. *J. Phys. Chem. Lett.* **2014**, *5*, 2390.
- (4) Batra, A. K.; Bhattacharjee, S.; Chilvery, A. K.; Aggarwal, M. D.; Edwards, M. E.; Bhalla, A. *J. Photon. Energy* **2011**, *1*, 014001.
- (5) Bokov, A. A.; Ye, Z. G. *J. Mater. Sci.* **2006**, *41*, 31.
- (6) Loi, M. A.; Hummelen, J. C. *Nat. Mater.* **2013**, *12*, 1087.
- (7) Mitzi, D. B. (1999) Synthesis, Structure, and Properties of Organic-Inorganic Perovskites and Related Materials, in Progress in Inorganic Chemistry, Volume 48 (ed K. D. Karlin), John Wiley & Sons, Inc., Hoboken, NJ, USA. doi: 10.1002/9780470166499.ch1
- (8) Frost, J. M.; Butler, K. T.; Brivio, F.; Hendon, C. H.; van Schilfgaarde, M.; Walsh, A. *Nano. Lett.* **2014**, *14*, 2584.
- (9) Takahashi, Y.; Obara, R.; Lin, Z.-Z.; Takahashi, Y.; Naito, T.; Inabe, T.; Ishibashi, S.; Terakura, K. *Dalton Trans.* **2011**, *40*,

5563.

- (10) Bhalla, A.; Guo, R.; Roy, R. *Mater. Res. Innov.* **2000**, *4*, 3.
- (11) Stoumpos, C. C.; Malliakas C. D.; Kanatzidis, M. G. *Inorg. Chem.* **2013**, *52*, 9019.
- (12) Mitzi, D. B.; Feild, C. A.; Harrison, W. T. A.; Guloy, A. M. *Nature* **1994**, *369*, 467.
- (13) Kim, H.-S.; Im, S. H.; Park, N.-G. *J. Phys. Chem. C* **2014**, *118*, 5615.
- (14) Cheng, Z.; Lin, J. *CrystEngComm* **2010**, *12*, 2646.
- (15) Mitzi, D. B. *J. Chem. Soc. Dalton Trans.* **2001**, 1.
- (16) Mitzi, D. B.; Chondroudis, K.; Kagan, C. R. *IBM J. Res. Dev.*, **2001**, *45*, 29.
- (17) Yamada, K.; Kuranaga, Y.; Ueda, K.; Goto, S.; Okuda, T.; Furukawa, Y. *Bull. Chem. Soc. Jpn.* **1998**, *71*, 127.
- (18) Mitzi, D. B.; Feild, C. A.; Schlesinger, Z.; Laibowitz, R. B. *J. Solid State Chem.* **1995**, *114*, 159.
- (19) Poglitsch, A.; Weber, D. *J. Chem. Phys.* **1987**, *87*, 6373.
- (20) Knop, O.; Wasylshen, R. E.; White, M. A.; Cameron, T. S.; Van Oort, M. J. M. *Can. J. Chem.* **1990**, *68*, 412.
- (21) Yamada, K. *Z. Naturforsch.* **1990**, *46a*, 307.
- (22) Mitzi, D. B. *J. Mater. Chem.* **2004**, *14*, 2355.

- (23) Mitzi, D. B.; Wang, S.; Field, C. A.; Chess, C. A.; Guloy, A. M. *Science* **1995**, *267*, 1473.
- (24) Kagan, C. R.; Mitzi, D. B.; Dimitrakopoulos, C. D. *Science* **1999**, *286*, 945.
- (25) Chondroudis, K.; Mitzi, D. B.; *Chem. Mater.* **1999**, *11*, 3028.
- (26) Era, M.; Tsutsui, T.; Saito, S. *Appl. Phys. Lett.* **1995**, *67*, 2436.
- (27) Park, N.-G. *Mater. Today* 2015, **18**, 65.
- (28) Ziang, X.; Shifeng, L.; Laixiang, Q.; Shuping, P.; Wei, W.; Yu, Y.; Li, Y.; Zhijian, C.; Shufeng, W.; Honglin, D.; Minghui Y.; Qin, G. G. *Opt. Mater. Express* 2015, **5**, 29.
- (29) Ishihara, T. *J. Lumin.* 1994, **60–61**, 269.
- (30) Zhang, W.; Saliba, M.; Stranks, S. D.; Sun, Y.; Shi, X.; Wiesner, U.; Snaith, H. J. *Nano Lett.* 2013, **13**, 4505.
- (31) Lin, Q.; Armin, A.; Nagiri, R. C. R.; Burn, P. L.; Meredith, P. *Nat. Photonics*, 2015, **9**, 106.
- (32) Miyata, A.; Mitioglu, A.; Plochocka, P.; Portugall, O.; Wang, J. T.-W.; Stranks, S. D.; Snaith, H. J.; Nicholas, R. J. *Nat. Phys.* 2015, **11**, 582.
- (33) Koutselasy, I. B.; Ducassez, L.; Papavassiliou, G. C. *J. Phys.: Condens. Matter.* 1996, **8**, 1217.
- (34) Xing, G.; Mathews, N.; Sun, S.; Lim, S. S.; Lam, Y. M.;

- Grätzel, M.; Mhaisalkar, S.; Sum, T. C. *Science* 2013, **342**, 344.
- (35) Stranks, S. D.; Eperon, G. E.; Grancini, G.; Menelaou, C.; Alcocer, M. J. P.; Leijtens, T.; Herz, L. M.; Petrozza, A.; Snaith, H. J. *Science* 2013, **342**, 341.
- (36) Edri, E.; Kirmayer, S.; Henning, A.; Mukhopadhyay, S.; Gartsman, K.; Rosenwaks, Y.; Hodes, G.; Cahen, D. *Nano Lett.* 2014, **14**, 1000.
- (37) Dong, Q.; Fang, Y.; Shao, Y.; Mulligan, P.; Qiu, J.; Cao, L.; Huang, J. *Science* 2015, **347**, 967.
- (38) Ponceca, Jr., C. S.; Savenije, T. J.; Abdellah, M.; Zheng, K.; Yartsev, A.; Pascher, T.; Harlang, T.; Chabera, P.; Pullerits, T.; Stepanov, A.; Wolf, J.-P.; Sundström, V. *J. Am. Chem. Soc.* 2014, **136**, 5189.
- (39) Leijtens, T.; Stranks, S. D.; Eperon, G. E.; Lindblad, R.; Johansson, E. M. J.; McPherson, I. J.; Rensmo, H.; Ball, J. M.; Lee, M. M.; Snaith, H. J. *ACS Nano* 2014, **8**, 7147.
- (40) Wehrenfennig, C.; Eperon, G. E.; Johnston, M. B.; Snaith, H. J.; Herz, L. M. *Adv. Mater.* 2014, **26**, 1584.
- (41) Hirasawa, M.; Ishihara, T.; Goto, T.; Uchida, K.; Miura, N. *Phys. B*, **1994**, *201*, 427.
- (42) Samiee, M.; Konduri, S.; Ganapathy, B.; Kottokkaran, R.; Abbas, H. A.; Kitahara, A.; Joshi, P.; Zhang, L.; Noack, M.;

- Dalal, V. *Appl. Phys. Lett.* **2014**, *105*, 153502.
- (43) Hu, M.; Bi, C.; Yuan, Y.; Xiao, Z.; Dong, Q.; Shao, Y.; Huang, J. *small*, **2015**, *11*, 2164–2169.
- (44) Bretschneider, S. A.; Weickert, J.; Dorman, J. A.; Schmidt-Mende, L. *APL Mater.* **2014**, *2*, 040701.
- (45) Kim, H.-S.; Lee, C.-R.; Im, J.-H.; Lee, K.-B.; Moehl, T.; Marchioro, A.; Moon, S.-J.; Humphry-Baker, R.; Yum, J.-H.; Moser, J. E.; Graetzel, M.; Park, N.-G. *Sci. Rep.* **2012**, *2*, 591.
- (46) Ogomi, Y.; Morita, A.; Tsukamoto, S.; Saitho, T.; Fujikawa, N.; Shen, Q.; Toyoda, T.; Yoshino, K.; Pandey, S. S.; Ma, T.; Hayase, S. *J. Phys. Chem. Lett.* **2014**, *5*, 1004.
- (47) 125 Park, B.-w; Philippe, B.; Gustafsson, T.; Sveinbjörnsson, K.; Hagfeldt, A.; Johansson, E. M. J.; Boschloo, G. *Chem. Mater.* **2014**, *26*, 4466.
- (48) Wang, B.; Xiao, X.; Chen, T. *Nanoscale*, **2014**, *6*, 12287.
- (49) Pang, S.; Hu, H.; Zhang, J.; Lv, S.; Yu, Y.; Wei, F.; Qin, T.; Xu, H.; Liu, Z.; Cui, G. *Chem. Mater.* **2014**, *26*, 1485.
- (50) Im, J.-H.; Chung, J.; Kim, S.-J.; Park, N.-G. *Nanoscale Res. Lett.* **2012**, *7*, 353.
- (51) Kitazawa, N.; Watanabe, Y.; Nakamura, Y. *J. Mater. Sci.* **2002**, *37*, 3585.
- (52) Noh, J. H.; Im, S. H.; Heo, J. H.; Mandal, T. N.; Seok, S. I.

- Nano Lett.*, **2013**, *13*, 1764.
- (53) Hao, F.; Stoumpos, C. C.; Cao, D. H.; Chang, R. P. H.; Kanatzidis, M. G. *Nat. Photonics* **2014**, *8*, 489.
- (54) Zhang, M.; Yu, H.; Lyu, M.; Wang, Q.; Yun, J.-H.; Wang, L. *Chem. Commun.* **2014**, *50*, 11727.
- (55) D'Innocenzo, V.; Grancini, G.; Alcocer, M. J.; Kandada, A. R.; Stranks, S. D.; Lee, M. M.; Lanzani, G.; Snaith, H. J.; Petrozza, A. *Nat. Commun.* **2014**, *5*, 3586.
- (56) Tanaka, K.; Takahashi, T.; Ban, T.; Kondo, T.; Uchida, K.; Miura, N. *Solid State Commun.* **2003**, *127*, 619.
- (57) Sun, S.; Salim, T.; Mathews, N.; Duchamp, M.; Boothroyd, C.; Xing, G.; Sum, T. C.; Lam, Y. M. *Energy Environ. Sci.* **2014**, *7*, 399.
- (58) Zhou, E.; Cong, J.; Hashimoto, K.; Tajima, K. *Adv. Mater.* **2013**, *25*, 6991.
- (59) Kirchartz, T.; Gong, W.; Hawks, S. A.; Agostinelli, T.; MacKenzie, R. C. I.; Yang, Y.; Nelson, J. *J. Phys. Chem. C* **2012**, *116*, 7672.
- (60) Kojima, A.; Teshima, K.; Shirai, Y.; Miyasaka, T. *J. Am. Chem. Soc.* **2009**, *131*, 6050.
- (61) Zhou, Z.; Wang, Z.; Zhou, Y.; Pang, S.; Wang, D.; Xu, H.; Liu, Z.; Padture, N. P.; Cui, G. *Angew. Chem. Int. Ed.* **2015**, *54*,

9705.

- (62) Ahn, N.; Son, D.-Y.; Jang, I.-H.; Kang, S. M.; Choi, M.; Park, N.-G. *J. Am. Chem. Soc.* **2015**, *137*, 8696.
- (63) Wei, H.; Shi, J.; Xu, X.; Xiao, J.; Luo, J.; Dong, J.; Lv, S.; Zhu, L.; Wu, H.; Li, D.; Luo, Y.; Meng, Q.; Chen Q. *Phys. Chem. Chem. Phys.* **2015**, *17*, 4937.
- (64) Xia, X.; Li, H.; Wu, W.; Li, Y.; Fei, D.; Gao, C.; Liu, X. *ACS Appl. Mater. Interfaces* **2015**, *7*, 16907.
- (65) Bu, L.; Liu, Z.; Zhang, M.; Li, W.; Zhu, A.; Cai, F.; Zhao, Z.; Zhou Y. *ACS Appl. Mater. Interfaces* **2015**, *7*, 17776.
- (66) Gratia, P.; Magomedov, A.; Malinauskas, T.; Daskeviciene, M.; Abate, A.; Ahmad, S.; Grätzel, M.; Getautis, V.; Nazeeruddin, M. K. *Angew. Chem. Int. Ed.* **2015**, *54*, 11409.
- (67) Li, G.; Ching, K. L.; Ho, J. Y. L.; Wong, M.; Kwok, H.-S. *Adv. Energy Mater.* **2015**, *5*, 1401775.
- (68) Lee, M. M.; Teuscher, J.; Miyasaka, T.; Murakami, T. N.; Snaith, H. J. *Science* **2012**, *338*, 643.
- (69) Ball, J. M.; Lee, M. M.; Hey, A.; Snaith H. J. *Energy Environ. Sci.* **2013**, *6*, 1739.
- (70) Zhou, H.; Chen, Q.; Li, G.; Luo, S.; Song, T.-b.; Duan, H.-S.; Hong, Z.; You, J.; Liu, Y.; Yang Y. *Science* **2014**, *345*, 542.
- (71) Liu, M.; Johnston M. B.; Snaith, H. J. *Nature* **2013**, *501*, 395.

- (72) Zheng, Y. C.; Yang, S.; Chen, X.; Chen, Y.; Hou, Y.; Yang, H. G. *Chem. Mater.* **2015**, *27*, 5116.
- (73) Huang, L.; Hu, Z.; Yue, G.; Liu, J.; Cui, X.; Zhang, J.; Zhu, Y. *Phys. Chem. Chem. Phys.* **2015**, *17*, 22015.
- (74) Chen, Q.; Zhou, H.; Fang, Y.; Stieg, A. Z.; Song, T.-B.; Wang, H.-H.; Xu, X.; Liu, Y.; Lu, S.; You, J.; Sun, P.; McKay, J.; Goorsky, M. S.; Yang, Y. *Nat. Commun.* **2015**, *6*, 7269.
- (75) Liu, D.; Kelly, T. L. *Nat. Commun.* **2014**, *8*, 133.
- (76) Chen, Q.; Zhou, H.; Hong, Z.; Luo, S.; Duan, H.-S.; Wang, H.-H.; Liu, Y.; Li, G.; Yang, Y. *J. Am. Chem. Soc.* **2014**, *136*, 622.
- (77) Heo, J. H.; Song, D. H.; Han, H. J.; Kim, S. Y.; Kim, J. H.; Kim, D.; Shin, H. W.; Ahn, T. K.; Wolf, C.; Lee, T.-W.; Im, S. H. *Adv. Mater.* **2015**, *27*, 3424.
- (78) Cheng, Y.; Yang, Q.-D.; Xiao, J.; Xue, Q.; Li, H.-W.; Guan, Z.; Yip, H.-L.; Tsang, S.-W. *ACS Appl. Mater. Interfaces* **2015**, *7*, 19986.
- (79) Nie, W.; Tsai, H.; Asadpour, R.; Blancon, J.-C.; Neukirch, A. J.; Gupta, G.; Crochet, J. J.; Chhowalla, M.; Tretiak, S.; Alam, M. A.; Wang, H.-L.; Mohite, A. D. *Science*, **2015**, *347*, 522
- (80) Tsai, H.; Nie, W.; Cheruku, P.; Mack, N. H.; Xu, P.; Gupta, G.; Mohite, A. D.; Wang, H.-L. *Chem. Mater.* **2015**, *27*, 5570.
- (81) Xia, F.; Wu, Q.; Zhou, P.; Li, Y.; Chen, X.; Liu, Q.; Zhu, J.; Dai,

- S.; Lu, Y.; Yang, S. *ACS Appl. Mater. Interfaces* **2015**, *7*, 13659.
- (82) Malinkiewicz, O.; Yella, A.; Lee, Y. H.; Espallargas, G. M.; Graetzel, M.; Nazeeruddin, M. K.; Bolink, H. J. *Nat. Photonics* **2014**, *8*, 128.
- (83) Wang, Q.; Shao, Y.; Dong, Q.; Xiao, Z.; Yuan Y.; Huang, J. *Energy Environ. Sci.* **2014**, *7*, 2359.
- (84) Chiang, C.-H.; Tseng, Z.-L.; Wua, C.-G. *J. Mater. Chem. A* **2014**, *2*, 15897.
- (85) Jung, J. W.; Williams, S. T.; Jen, A. K.-Y. *RSC Adv.* **2014**, *4*, 62971.
- (86) Jung, J. W.; Chueh, C.-C.; Jen, A. K.-Y. *Adv. Energy Mater.* **2015**, *5*, 1500486.
- (87) Liu, X.; Lei, M.; Zhou, Y.; Song, B.; Li, Y. *Appl. Phys. Lett.* **2015**, *107*, 063901.
- (88) Yao, K.; Wang, X.; Li, F.; Zhou, L. *Chem. Commun.* **2015**, *51*, 15430.
- (89) Dong, Q.; Yuan, Y.; Shao, Y.; Fang, Y.; Wang, Q.; Huang, J. *Energy Environ. Sci.* **2015**, *8*, 2464.
- (90) Chen, Y.; Peng, J.; Su, D.; Chen, X.; Liang, Z. *ACS Appl. Mater. Interfaces*, **2015**, *7*, 4471.
- (91) Yang, M.; Guo, R.; Kadel, K.; Liu, Y.; O'Shea, K.; Bone, R.;

- Wang, X.; Hea, J.; Li, W. *J. Mater. Chem. A* **2014**, *2*, 19616.
- (92) Wang, J. T.-W.; Ball, J. M.; Barea, E. M.; Abate, A.; Alexander-Webber, J. A.; Huang, J.; Saliba, M.; Mora-Sero, I.; Bisquert, J.; Snaith, H. J.; Nicholas, R. J. *Nano Lett.* **2014**, *14*, 724.
- (93) Liu, Y.; Chen, Q.; Duan, H.-S.; Zhou, H.; Yang, Y. (M.); Chen, H.; Luo, S.; Song, T.-B.; Dou, L.; Honga, Z.; Yang, Y. *J. Mater. Chem. A* **2015**, *3*, 11940.
- (94) Zhu, Z.; Bai, Y.; Lee, H. K. H.; Mu, C.; Zhang, T.; Zhang, L.; Wang, J.; Yan, H.; So, S. K.; Yang, S. *Adv. Funct. Mater.* **2014**, *24*, 7357.
- (95) Eperon, G. E.; Burlakov, V. M.; Docampo, P.; Goriely, A.; Snaith, H. J. *Adv. Funct. Mater.* **2014**, *24*, 151.
- (96) Kim, H.-B.; Choi, H.; Jeong, J.; Kim, S.; Walker, B.; Song, S.; Kim, J. Y. *Nanoscale* **2014**, *6*, 6679.
- (97) Shen, D.; Yu, X.; Cai, X.; Peng, M.; Ma, Y.; Su, X.; Xiao, L.; Zou, D. *J. Mater. Chem. A* **2014**, *2*, 20454.
- (98) Jeon, N. J.; Noh, J. H.; Kim, Y. C.; Yang, W. S.; Ryu, S.; Seok, S. I. *Nat. Mater.* **2014**, *13*, 897.
- (99) Xiao, M.; Huang, F.; Huang, W.; Dkhissi, Y.; Zhu, Y.; Etheridge, J.; Gray-Weale, A.; Bach, U.; Cheng, Y.-B.; Spiccia, L. *Angew. Chem., Int. Ed.* **2014**, *53*, 9898.
- (100) Xiao, Z.; Dong, Q.; Bi, C.; Shao, Y.; Yuan, Y.; Huang, J. *Adv.*

- Mater.* **2014**, *26*, 6503.
- (101) Yang, Y.; Yang, M.; Li, Z.; Crisp, R.; Zhu, K.; Beard, M. C. *J. Phys. Chem. Lett.* **2015**, *6*, 4688.
- (102) Xing, G.; Mathews, N.; Lim, S. S.; Yantara, N.; Liu, X.; Sabba, D.; Grätzel, M.; Mhaisalkar, S.; Sum, T. C. *Nat. Mater.* **2014**, *13*, 476.
- (103) Shao, Y.; Xiao, Z.; Bi, C.; Yuan, Y.; Huang, J. *Nat. Commun.* **2014**, *5*, 5784.
- (104) Yin, J.; Cortecchia, D.; Krishna, A.; Chen, S.; Mathews, N.; Grimsdale, A. C.; Soci, C. *J. Phys. Chem. Lett.* **2015**, *6*, 1396.
- (105) Jeng, J.-Y.; Chiang, Y.-F.; Lee, M.-H.; Peng, S.-R.; Guo, T.-F.; Chen, P.; Wen, T.-C. *Adv. Mater.* **2013**, *25*, 3727.
- (106) Chiang, Y.-F.; Jeng, J.-Y.; Lee, M.-H.; Peng, S.-R.; Chen, P.; Guo, T.-F.; Wen, T.-C.; Hsu, Y.-J.; Hsu, C.-M. *Phys. Chem. Chem. Phys.* **2014**, *16*, 6033.
- (107) Etgar, L.; Gao, P.; Qin, P.; Graetzel, M.; Nazeeruddin, M. K. *J. Mater. Chem. A* **2014**, *2*, 11586.
- (108) Yang, W. S.; Noh, J. H.; Jeon, N. J.; Kim, Y. C.; Ryu, S.; Seo, J.; Seok, S. I. *Science* 2015, **348**, 1234.
- (109) Pellegrino, G.; Colella, S.; Deretzis, I.; Condorelli, G. G.; Smecca, E.; Gigli, G.; La Magna, A.; Alberti, A. *J. Phys. Chem. C* **2015**, *119*, 19808.

- (110) Yantara, N.; Yanan, F.; Shi, C.; Dewi, H. A.; Boix, P. P.; Mhaisalkar, S. G.; Mathews, N. *Chem. Mater.* **2015**, *27*, 2309.
- (111) Chen, Y.; Zhao, Y.; Liang, Z. *Chem. Mater.* **2015**, *27*, 1448.
- (112) Zuo, C.; Ding, L. *Nanoscale* **2014**, *6*, 9935.
- (113) Hynes, R. C.; Le Page, Y. *J. Appl. Cryst.* **1991**, *24*, 352.
- (114) Heo, J. H.; Han, H. J.; Kim, D.; Ahn, T. K.; Im, S. H. *Energy Environ. Sci.* **2015**, *8*, 1602.
- (115) Bi, D.; Yang, L.; Boschloo, G.; Hagfeldt, A.; Johansson, E. M. J. *J. Phys. Chem. Lett.* **2013**, *4*, 1532.
- (116) Li, J.-F.; Zhang, Z.-L.; Gao, H.-P.; Zhang, Y.; Mao, Y.-L. *J. Mater. Chem. A* **2015**, *3*, 19476.
- (117) Luo, P.; Liu, Z.; Xia, W.; Yuan, C.; Cheng, J.; Lu, Y. *ACS Appl. Mater. Interfaces* **2015**, *7*, 2708.
- (118) Chen, B.; Zheng, X.; Yang, M.; Zhou, Y.; Kundu, S.; Shi, J.; Zhu, K.; Priya, S. *Nano Energy* **2015**, *13*, 582.
- (119) Zhang, W.; Saliba, M.; Moore, D. T.; Pathak, S. K.; Hörantner, M. T.; Stergiopoulos, T.; Stranks, S. D.; Eperon, G. E.; Alexander-Webber, J. A.; Abate, A.; Sadhanala, A.; Yao, S.; Chen, Y.; Friend, R. H.; Estroff, L. A.; Wiesner, U.; Snaith, H. *J. Nat. Commun.* **2015**, *6*, 6142.
- (120) Wakamiya, A.; Endo, M.; Sasamori, T.; Tokitoh, N.; Ogomi, Y.; Hayase, S.; Murata, Y. *Chem. Lett.*, 2014, **43**, 711.

- (121) Swartz , S.; Schulze, W. A.; Biggers, J. V. *Ferroelectrics* **1981**, 38, 765.
- (122) Takahashi, M.; Noguchi, Y.; Miyayama, M. *Jpn. J. Appl. Phys.* **2002**, 41, 7053.
- (123) Noguchi, Y.; Soga, M.; Takahashi, M.; Miyayama, M. *Jpn. J. Appl. phys.* **2005**, 44, 6998.
- (124) Roy, A.; Prasad, R.; Auluck, S.; Garg, A. *J. Phys.: Condens. Matter* **2010**, 22, 165902.
- (125) Sesion Jr., P. D.; Henriques, J. M.; Barboza, C. A.; Albuquerque, E. L.; Freire, V. N.; Caetano, E. W. S. *J. Phys.: Condens. Matter* **2010**, 22, 435801.
- (126) Damjanovic, D.; Budimir, M.; Davis, M.; Setter, N. *J. Mater. Sci.* **2006**, 41, 65.
- (127) Shen, Y.; Clarke, D. R.; Fuierer, P. A. *Appl. Phys. Lett.* **2008**, 93, 102907.
- (128) Sparks, T. D.; Fuierer, P. A.; Clarke, D. R. *J. Am. Ceram. Soc.* **2010**, 93, 1136.
- (129) Volonakis, G.; Giustino, F. *J. Phys. Chem. Lett.* **2015**, 6, 2496.
- (130) Haruyama, J.; Sodeyama, K.; Han, L.; Tateyama, Y. *J. Phys. Chem. Lett.* **2014**, 5, 2903
- (131) You, J.; Hong, Z.; Yang, Y. (M.); Chen, Q.; Cai, M.; Song, T.-B.; Chen, C.-C.; Lu, S.; Liu, Y.; Zhou, H.; Yang, Y. *ACS Nano*

2014, 8, 1674.

(132) Xu, Y.; Zhu, L.; Shi, J.; Lv, S.; Xu, X.; Xiao, J.; Dong, J.; Wu, H.; Luo, Y.; Li, D.; Meng, Q. *ACS Appl. Mater. Interfaces* **2015**, 7, 2242.

(133) Kim, H.-S.; Mora-Sero, I.; Gonzalez-Pedro, V.; Fabregat-Santiago, F.; Juarez-Perez, E. J.; Park, N.-G.; Bisquert, J. *Nat. Commun.* 2013, **4**, 2242.

(134) Sanchez, R. S.; Gonzalez-Pedro, V.; Lee, J.-W.; Park, N.-G.; Kang, Y. S.; Mora-Sero, I.; Bisquert, J. *J. Phys. Chem. Lett.* **2014**, 5, 2357.

초 록

원스텝 방법은 간단하고 쉽게 페로브스카이트 필름을 제작할 수 있다는 장점을 가지고 있어 원스텝 방법으로 페로브스카이트 필름을 제작하는 많은 연구가 이루어지고 있다. 그러나 원스텝 방법으로 필름을 제작할 경우 페로브스카이트의 빠른 결정화로 인해 균일하게 표면을 덮는 필름을 제작하기 어렵고 그 결과 원스텝 방법으로 제작한 필름을 이용하여 태양전지를 제작할 경우 높은 효율을 기대하기 어렵다는 문제점이 있다. 이 연구에서는 고효율의 페로브스카이트 태양전지를 제작하기 위해 페로브스카이트 필름의 필름 모폴로지와 결정 방향성을 최적화하는 공정 조건을 알아보았다. 첫째로 스핀코팅 시간과 열처리 시 온도를 변화시킴으로써 두 종류의 모폴로지(tree-like 모폴로지와 flower-like 모폴로지)를 나타내는 $\text{CH}_3\text{NH}_3\text{PbI}_3$ 필름을 얻을 수 있었다. Flower-like 모폴로지의 필름은 짧은 스핀코팅 시간으로 고체화되기 전의 필름을 열처리하여 얻을 수 있었고 반면, tree-like 모폴로지의 필름은 스핀코팅 시 고체화가 일어난 필름을 열처리하여 얻을 수 있었다. In-situ 광학 현미경과 X-선 산란을 통해 스핀코팅 시간에 따라 서로 다른 두 모폴로지(tree-like 모폴로지와 flower-like 모폴로지)를 보이는 원인을 확인한 결과, tree-like 모폴로지의 경우, $\text{CH}_3\text{NH}_3\text{I}-\text{PbI}_2$ -용매 복합체가 먼저 형성되고 열처리 시 $\text{CH}_3\text{NH}_3\text{PbI}_3$ 로 변화되는 것을 확인할 수 있었던 반면, flower-like 모폴로지의 경우, 액체 상태의 필름에서 $\text{CH}_3\text{NH}_3\text{I}-\text{PbI}_2$ -용매 복합체의 형성 없이 직접적으로

$\text{CH}_3\text{NH}_3\text{PbI}_3$ 필름이 형성되는 것을 확인할 수 있었다. DMSO로 제작한 flower-like 모폴로지를 보이는 필름은 (112)와 (200) 방향성을 나타내는 큰 결정들로 이루어져 있었고 13.85%의 높은 효율을 나타내었다. 반면, tree-like 모폴로지를 나타내는 필름은 작은 결정들로 이루어져 있었고 특정한 결정 방향성을 나타내지 않았으며 매우 낮은 효율을 나타내었다. 둘째로 두 종류의 유기 전구체($\text{CH}_3\text{NH}_3\text{I}$ 와 $\text{CH}_3\text{NH}_3\text{Cl}$)를 사용함으로써 서로 다른 결정 방향성을 나타내는 $\text{CH}_3\text{NH}_3\text{PbI}_3$ 필름을 제작하였고 결정 방향성이 페로브스카이트 태양 전지의 광전 특성에 미치는 영향을 확인하였다. Inverted 소자의 경우, 유기 전구체로 $\text{CH}_3\text{NH}_3\text{I}$ 를 사용한 I_3 필름(13.60%)이 $\text{CH}_3\text{NH}_3\text{Cl}$ 을 사용한 I_2Cl 필름(11.26%)에 비해 더 높은 단락 전류 밀도와 fill factor를 나타내어 결과적으로 더 높은 효율을 보인 반면, normal 소자의 경우, I_2Cl 필름(12.88%)이 I_3 필름(3.97%)에 비해 더 높은 효율을 나타내었다. I_3 필름과 I_2Cl 필름이 서로 다른 결정 방향성을 나타낸다는 점을 고려해 볼 때 페로브스카이트 결정의 방향성이 광전 특성에 직접적인 영향을 미친다는 것을 알 수 있었다. 결정 방향성에 따라 효율의 차이가 나타나는 원인을 확인하기 위해 transient photoluminescence를 측정하여 전하의 lifetime을 확인하였다. 짧은 lifetime은 페로브스카이트와 전하수송층 간의 빠른 전하 전이를 나타내기 때문에 짧은 lifetime을 나타내는 소자의 경우 높은 단락 전류 밀도와 효율을 나타내었다. 또한, normal 소자에서 강한 hysteresis가 나타나는 원인은 페로브스카이트에서 전하수송층으로 전하 전이가 느리게 일어났고 또한 전자와 정공의 전이가 서로 큰 차이를

보이기 때문임을 확인할 수 있었다.

주요어: 페로브스카이트 태양전지, 메틸암모늄 요오드화 납, 필름
모폴로지, 평면 이중접합, 공정 조건, 결정 방향성

학 번: 2009-23044

List of papers

1. Lee, J. W.; Bae, S.; Jo, W. H. *J. Mater. Chem. A* **2014**, *2*, 14146.
2. Bae, S.; Lee, J. U.; Park, H.-S.; Jung, E. H.; Jung, J. W.; Jo, W. H. *Sol. Energy Mater. Sol. Cells* **2014**, *130*, 599.
3. Jung, E. H.; Bae, S.; Yoo, T. W.; Jo, W. H. *Polym. Chem.* **2014**, *5*, 6545.
4. Jo, J. W.; Bae, S.; Liu, F.; Russell, T. P.; Jo, W. H. *Adv. Funct. Mater.* **2015**, *25*, 120.
5. Kim, S. S.; Bae, S.; Jo, W. H. *Chem. Commun.* **2015**, *51*, 17413.
6. Bae, S.; Han, S. J.; Shin, T. J.; Jo, W. H. *J. Mater. Chem. A* **2015**, *3*, 23964.